

The Applicability of the Tap-Delay Line Channel Model to Ultra Wideband

Liu Yang

Thesis submitted to the Faculty of the
Virginia Polytechnic Institute and State University
in partial fulfillment of the requirements for the degree of

Master of Science
in
Electrical Engineering

Committee:

R. Michael Buehrer (chair)
Brian D. Woerner
Annamalai Annamalai

Sep 15, 2004
Blacksburg, VA

Keywords: ultra-wideband, UWB, channel model, CLEAN, pulse distortion

Copyright 2004, Liu Yang

The Applicability of the Tap-Delay Line Channel Model to Ultra Wideband

Liu Yang
Thesis Abstract

Ultra-wideband (UWB) communication systems are highly promising because of their capabilities for high data rate information transmission with low power consumption and low interference and their immunity to multipath fading. More importantly, they have the potential to relieve the “spectrum drought” caused by the explosion of wireless systems in the past decade by operating in the same bands as existing narrowband systems. With the extremely large bandwidth of UWB signals, we need to revisit UWB channel modeling. Specifically we need to verify whether or not the traditional tap-line delay channel model is still applicable to UWB.

One essential task involved in channel modeling is deconvolving the channel impulse response from the measurement data. Both frequency domain and time domain techniques were studied in this work. After a comparison, we examined a time domain technique known as the CLEAN algorithm for our channel modeling analysis. A detailed analysis of the CLEAN algorithm is given, as it is found that it is sufficient for our application.

The impact of per-path pulse distortion due to various mechanisms on the tap-delay line channel model is discussed. It is shown that with cautious interpretation of the channel impulse response, the tap-line delay channel model is still applicable to UWB.

Table of Contents

1	Introduction.....	1
1.1	Ultra-Wideband communications background.....	1
1.2	Motivation.....	5
1.3	Thesis Organization.....	7
2	Channel Measurement and Channel Modeling.....	9
2.1	Channel Sounding Techniques.....	9
2.2	Deterministic Channel Modeling vs. Statistical Channel Modeling.....	13
2.3	Large Scale Channel Modeling.....	14
2.4	Small Scale Channel Modeling.....	18
3	Deconvolution Techniques.....	22
3.1	Introduction.....	22
3.2	Frequency Domain Techniques.....	23
3.2.1	Inverse filtering.....	23
3.2.2	Van-Cittert deconvolution.....	28
3.3	Time domain technique: CLEAN algorithm.....	35
4	Performance of CLEAN.....	39
4.1	Delay/Amplitude Estimate Performance.....	39
4.2	Other super-resolution techniques.....	52
5	Impact of Deconvolution on CLEAN Regenerated Channel Model.....	57
5.1	Saleh-Valenzuela Model.....	57
5.2	Comparison of Channel Statistics.....	58
6	Impact of Discrete Assumption on UWB Channel Modeling.....	68
6.1	Frequency distortion of materials.....	68
6.2	Distortion due to reflection.....	74
6.3	Antenna induced distortion.....	80
6.4	Diffraction induced distortion.....	83
7	Conclusions and Future Work.....	86
	Appendix A: Signal distortions after passing through some common building materials.....	88
	Appendix B: Signal distortions due to reflections from some common shapes.....	101
	Bibliography.....	106
	Vita.....	110

List of Figures

Figure 1-1	Fractional bandwidth comparison.....	2
Figure 1-2	Gaussian monocycle pulse (a) and energy spectral density (b).....	3
Figure 2-1	Traditional time-domain direct pulse measurement system.....	11
Figure 2-2	Spread Spectrum Sliding Correlator Channel Measurement system.....	12
Figure 2-3	Vector Network Analyzer Measurement System.....	13
Figure 3-1	Transmitted Gaussian Pulse.....	26

Figure 3-2 True Channel impulse response	26
Figure 3-3 Received signal with SNR of 20dB	27
Figure 3-4 Continuous and discrete inverse filtering estimate of channel impulse response	27
Figure 3-5 Magnitude of the transfer function using direct division and the deconvolution filter with different filtering levels (number of iterations).....	31
Figure 3-6 Magnitude of the deconvolution filter using different number of iterations...	32
Figure 3-7 Results of frequency domain optimization criteria	33
Figure 3-8 Closer look at the results of frequency domain optimization criteria in stop band.....	33
Figure 3-9 Comparison of impulse response obtained using different number of iterations	34
Figure 3-10 Comparison of Van-Cittert deconvolution result using Bennia-Riad optimization criterion and the true channel impulse response.....	35
Figure 3-11 CLEAN deconvolution result.....	37
Figure 4-1 Simulated LOS Pulse	39
Figure 4-2 Sample of CLEAN estimate of CIR when paths are resolvable	41
Figure 4-3 Sample of comparison of reconstructed received signal and actual received signal when paths are resolvable.....	41
Figure 4-4 Sample of comparison of reconstructed received signal and desired part of received signal when paths are resolvable	42
Figure 4-5 Sample of CLEAN estimate of CIR when paths are not resolvable	45
Figure 4-6 Sample comparison of reconstructed received signal and actual received signal when paths are not resolvable	45
Figure 4-7 Sample comparison of reconstructed received signal and desired part of received signal when paths are not resolvable.....	46
Figure 4-8 Sample of CLEAN estimate of CIR when pulse is distorted and paths are resolvable	48
Figure 4-9 Sample comparison of reconstructed received signal and actual received signal when pulse is distorted and paths are resolvable	48
Figure 4-10 Sample comparison of reconstructed received signal and desired part of received signal when pulse is distorted and paths are resolvable	49
Figure 4-11 Sample of CLEAN estimate of CIR when pulse is distorted and paths are not resolvable	50
Figure 4-12 Sample of comparison of reconstructed received signal and actual received signal when pulse is distorted and paths are resolvable.....	51
Figure 4-13 Sample of comparison of reconstructed received signal and desired part of received signal when pulse is distorted and paths are resolvable	51
Figure 4-14 True Channel Impulse Response.....	55
Figure 4-15 Received Signal.....	55
Figure 4-16 LS Estimate of the CIR Without Noise.....	55
Figure 4-17 LS Estimate of the CIR with SNR=20dB	56
Figure 5-1 Mean Excess Delay CDF for Synthetic Channel and CLEAN Output with CLEAN path threshold 15dB.....	60
Figure 5-2 RMS delay spread CDF for Synthetic Channel and CLEAN Output with CLEAN path threshold 15dB.....	60

Figure 5-3 Number of Multipath CDF comparisons with CLEAN path threshold 15dB.	60
Figure 5-4 Mean Excess Delay CDF for Synthetic Channel and CLEAN Output with CLEAN path threshold 20dB.....	61
Figure 5-5 RMS delay spread CDF for Synthetic Channel and CLEAN Output with CLEAN path threshold 20dB.....	61
Figure 5-6 Number of Multipath CDF comparisons with CLEAN path threshold 20dB.	61
Figure 5-7 Mean Excess Delay CDF for Synthetic Channel and CLEAN Output with CLEAN path threshold 15dB at SNR=20dB	62
Figure 5-8 RMS delay spread CDF for Synthetic Channel and CLEAN Output with CLEAN path threshold 15dB at SNR=20dB	63
Figure 5-9 Number of Multipath CDF Comparisons with CLEAN path threshold 15dB at SNR=20dB.....	63
Figure 5-10 Mean Excess Delay CDF for Synthetic Channel and CLEAN Output with CLEAN path threshold 20dB at SNR=20dB	63
Figure 5-11 RMS delay spread CDF for Synthetic Channel and CLEAN Output with CLEAN path threshold 20dB at SNR=20dB	64
Figure 5-12 Number of Multipath CDF comparisons with CLEAN path threshold 20dB at SNR=20dB.....	64
Figure 5-13 The mean correlation between multipath components at any 2 excess delays (noise free)	66
Figure 5-14 The mean correlation between multipath components at any 2 excess delays (SNR=20dB)	66
Figure 6-1 Original and distorted UWB pulse after passing through Brick	70
Figure 6-2 Discrete Tap Channel Model Created by CLEAN Algorithm using the Distorted Pulse After Passing Through Brick (CLEAN threshold of 20 dB).....	70
Figure 6-3 Distorted UWB Pulse After Passing through Brick and Pulse Produced from CLEAN	71
Figure 6-4 Auto-correlation comparison between template pulse, distort pulse and CLEAN estimate of distorted pulse	73
Figure 6-5 Measurement Diagram.....	75
Figure 6-6 Line-of-sight signal (left) and signal reflected from a hemisphere of 6 inch diameter.....	76
Figure 6-7 Reflected pulse by a hemisphere and CLEAN estimate of the reflected pulse	77
Figure 6-8 CLEAN generated Impulse Response for signal reflected by a Hemisphere of 6 inch diameter with CLEAN threshold of 20 dB	77
Figure 6-9 Auto-correlation comparison between template pulse, distort pulse and CLEAN estimate of distorted pulse	79
Figure 6-10 Received Pulse from various elevation angles using Biconical Antennas....	81
Figure 6-11 Received pulse from elevation angles of zero degree (left) and 60 degrees (right) using Biconical antennas	82
Figure 6-12 Discrete time Impulse Response for received pulse at elevation angle of 60 degree using pulse received at boresight (0 degree elevation) as template and CLEAN threshold of 20dB	82
Figure 6-13 Received pulse with and without single edge diffraction using values given in [41] [42]	84

Figure 6-14 Discrete time Impulse Response due to a single edge diffraction along a single path with CLEAN threshold of 20dB.....	84
---	----

List of Tables

Table 3-1 Correlation comparison of Inverse Filtering using different thresholds at different SNRs	25
Table 4-1 MSE of Estimated Two Tap CIR for various Delays (SNR is infinite)	40
Table 4-2 CLEAN performance at different SNR when we consider the actual received signal if paths are resolvable.....	43
Table 4-3 CLEAN performance at different SNR when we consider the desired received signal if paths are resolvable.....	43
Table 4-4 CLEAN performance at different SNR when paths are not resolvable (received signal).....	46
Table 4-5 CLEAN performance at different SNR values when paths are not resolvable (desired signal).....	47
Table 4-6 CLEAN performance at different SNR when we consider the actual received signal if pulse is distorted and paths are resolvable.....	49
Table 4-7 CLEAN performance at different SNR values when we consider the desired received signal if the pulse is distorted and paths are resolvable	50
Table 4-8 CLEAN performance at different SNR when we consider the actual received signal if pulse is distorted and paths are not resolvable.....	51
Table 4-9 CLEAN performance at different SNR when we consider the desired received signal if pulse is distorted and paths are not resolvable.....	52
Table 5-1 Saleh-Valenzuela Model parameters for Bicone NLOS	58
Table 5-2 Bicone NLOS S_V model(path threshold for S_V=15dB CLEAN path threshold=15/20dB)	62
Table 5-3 Bicone NLOS S_V model ; path threshold=15dB CLEAN path threshold=15/20dB at different SNRs.....	64
Table 6-1 Discrete Channel Representation of UWB Pulse (TEM LOS Pulse) After Passing through Common Building Materials with CLEAN threshold of 20dB.....	74
Table 6-2 Discrete Channel Representation of UWB Pulse (TEM LOS Pulse) After Reflected by Common shapes with CLEAN threshold of 20dB	78
Table 6-3 Discrete Channel Representation of UWB Pulse (using Bicone antenna) Received at Various Elevation Angles with 20dB CLEAN threshold	83

1 Introduction

1.1 *Ultra-Wideband communications background*

Ultra-wideband (UWB) communication systems are highly promising because of their capabilities for high data rate information transmission with low power consumption and low interference and their immunity to multipath fading. More importantly, they have the potential to relieve the “spectrum drought” caused by the explosion of wireless systems in the past decade by operating in the same bands as existing narrowband (NB) systems [1]. UWB radiation is characterized by its extremely wide fractional bandwidth. Fractional bandwidth is defined as the ratio of the bandwidth occupied by the signal to the center frequency of the signal: $(f_h - f_L) / f_c$. In the literature, a UWB radio signal is defined as a signal whose 3dB fractional bandwidth is greater than 0.25 [43]. The FCC defined UWB signals as those which have a fractional bandwidth greater than 0.20 or a bandwidth greater than 500MHz measured at the -10dB points [2]. By comparison, the fractional bandwidth of a conventional narrowband radio signal is typically smaller than 0.01. A comparative illustration of the fractional bandwidth of UWB and NB signals is shown in Figure 1-1 Fractional bandwidth comparison.

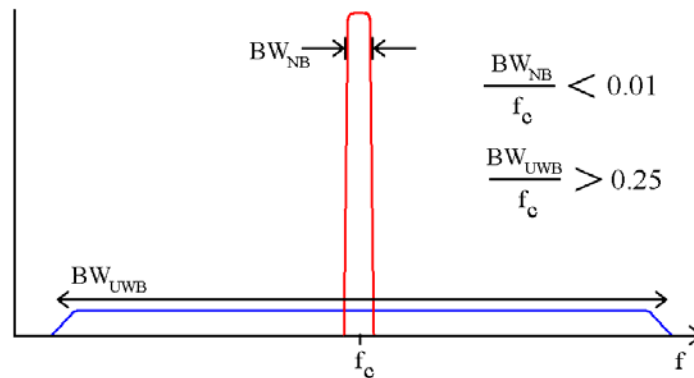


Figure 1-1 Fractional bandwidth comparison

The origin of UWB technology dates back to as early as 1962 when Ross [3] began to develop time-domain (impulse response) techniques for the characterization of linear time-invariant microwave structures. Through the late 1980's, this technology was alternately known as “carrier-free”, “baseband”, or “impulse radio”. The term “Ultra-Wideband” was introduced in a DARPA report in 1989. By that time, UWB techniques had experienced nearly 30 years of development.

While different methods could be employed to meet the bandwidth definitions of UWB signals, typically the term UWB also refers to systems that use impulse radio. Impulse radio is fundamentally different from traditional wireless communications in that it uses very short duration pulses as opposed to sinusoidal signals. The basic idea is to transmit and receive a train of extremely short duration pulses (on the order of a nanosecond) modulated by the data with very low duty cycle (on the order of 0.01, 0.001 or less). The short duration pulses, operating at ultra-low power, often times have a bandwidth over several GHz. A typical UWB pulse known as the Gaussian monocycle and its spectrum are shown in Figure 1-2. Throughout the work, unless otherwise stated, the use of the term UWB will also imply impulse radio.

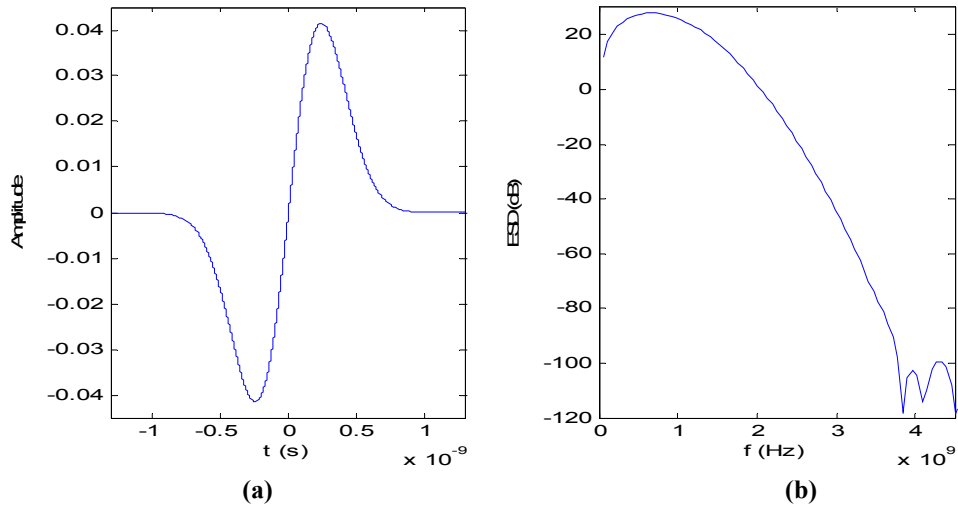


Figure 1-2 Gaussian monocycle pulse (a) and energy spectral density (b)

In wireless communications, the received signal is the sum of multiple replicas of the transmitted signal due to reflection, diffraction, scattering and etc. These replicas may arrive out of phase, thus canceling each other. This phenomenon is known as multipath fading. It can severely degrade the performance of communications systems. Because the UWB pulse is extremely short, pulses arriving at the receiver are mostly resolvable and thus the signal is highly immune to multipath fading. This can allow the communication system designer to substantially reduce the system fading margin. As a result UWB systems may not depend on diversity techniques as strongly as narrowband systems do. Due to the short duration of the pulses, UWB can also be used for precise positioning and tracking of devices by measuring the round trip delay at a UWB receiver. The ultra-low power will cause the least potential interference to existing radio systems and provide covert communications, which is very desirable for military applications. The low power spectral density results in the UWB signal being buried in the noise at the receiver; therefore it will be extremely difficult for an unauthorized receiver to either detect or

intercept the signal. Another attractive feature of UWB is that the devices can be inexpensive by making them nearly all “digital” with minimum RF components because of its “carrier-free” characteristic.

UWB technology has demonstrated great potential for communications, radar and geo-location applications. All these applications have a common architecture and it is possible to re-define the same UWB device for different applications in software [30]. For communications, UWB is proposed for many applications including indoor static wireless LANs [4], home-networking, asynchronous transfer mode multimedia [5], un-centralized multiple access communications, roadside automobile information services and secure military applications [6]. UWB technology has been well established in the radar community for decades and is widely used in ground penetrating radar for mining, wall/structure imaging, “stud finding”, and defect detection, through the wall imaging for law enforcement/rescue workers, vehicular radar for collision avoidance and ride performance enhancement, and improved resolution radar for a variety of civil and military applications. For geo-location, precision location is derived from round trip time-of-flight measurements using packet burst transmissions from the UWB rover and beacon transponders.

UWB is an evolving technology and provides many research challenges including antenna design, waveform design, receiver design, multi-user architectures for UWB systems, etc. Channel modeling is one of the challenging tasks involved in improving UWB technology. The extremely large bandwidth associated with UWB signals may make the use of traditional narrowband/wideband channel modeling inappropriate. Many

assumptions that are made for narrowband/wideband channel modeling may no longer hold for UWB channel modeling. For example, narrowband/wideband channel models assume that the received signal is the sum of delayed, phase shifted and attenuated copies of the transmitted signal. The interaction of these multiple replicas results in fading and possible frequency distortion. However, it is assumed that the individual copies are not distorted. When UWB signals are being used, this may not be true. Individual copies may be distorted thus introducing per-pulse frequency distortion in addition to the distortion seen in the total received signal. This means we must revisit the traditional model.

1.2 Motivation

The radio propagation channel is the principal contributor to many of the problems and limitations that beset mobile radio systems. Unlike wired channels that are stationary and predictable, radio channels are enormously random and do not offer easy analysis [7]. Hence, an accurate characterization of the channel is extremely important for the effective design, assessment and installation of radio communications systems. An accurate channel characterization for each frequency band, including physical understanding, key parameters and a detailed mathematical model of the channel, enables the designer or user of a wireless system to predict signal coverage, achievable data rate, and the specific performance attributes of alternative signaling and reception schemes [8]. However, if the model is particularly complex for analysis or simulation, it is of limited use to the designer or user who has finite time and resources to evaluate the system performance. It is very important for the system designer to trade off between a detailed description of the channel and the simplicity of the model for analysis and simulation uses.

The target applications for UWB systems include those where short range, fully mobile, wireless communications in a dense multipath and perhaps shadowed environment [32] are desirable. A more complete understanding of the potential of UWB communication systems in these scenarios requires the development of accurate models for the UWB propagation channel. If the random, time-varying radio channel is modeled as a time-varying linear filter, it can be completely characterized by its equivalent channel impulse response [1]. The widely used tap-delay line model was first suggested by Turin [9], assuming a stationary environment. At each point in a three-dimensional environment, the complex baseband channel is modeled as a linear filter [10], where its impulse response can be written as

$$h(t) = \sum_{k=0}^{N-1} \alpha_k e^{j\theta_k} \delta(t - \tau_k) \quad (1-1)$$

where N is the number of scaled α_k and time-delayed τ_k paths in the channel and θ_k is the phase associated with each path.

Since we are concerned with baseband UWB in this thesis, there is no phase associated with each path and Equation (1-1) can be simplified as [1],

$$h(t) = \sum_{k=0}^{N-1} \alpha_k \beta_k \delta(t - \tau_k) \quad (1-2)$$

where β_k is the polarity associated with each path.

The tap-delay line channel model is a simple but very practical model. It is based on the physical understanding of the received signal which is the sum of multiple replicas of the transmitted signal due to reflection, refraction, and scattering. This model has been used in mobile radio applications with great success [7] [31] and is widely applied to the UWB

indoor channel [1, 11, 12, 28, 29]. However, the applicability of this model still needs to be verified and is crucial to the whole UWB system design.

1.3 Thesis Organization

This thesis covers a range of topics related to the analysis of the applicability of the current tap-delay line channel model for UWB systems and compares different deconvolution techniques to extract the tap-delay line channel model.

Chapter 2 presents background material related to the channel characterization work. Discussion of traditional communications channel measurement and modeling techniques and their extensions to UWB applications are given.

Chapter 3 discusses some common deconvolution techniques in both the frequency domain and the time domain. An evaluation and comparison of these deconvolution techniques are presented. This work is necessary since the separation of the channel impulse response from the measurements typically requires deconvolution. It is necessary to choose a suitable deconvolution technique to facilitate the UWB channel modeling work in this thesis. We choose a time domain technique called CLEAN algorithm to process the measurement data for our analysis in this thesis. This technique is particularly useful since it directly results in a discrete channel impulse response.

Chapter 4 gives a detailed performance analysis of the CLEAN algorithm. Quantitative measures of the accuracy of the CLEAN algorithm are given for different scenarios. The

CLEAN algorithm is also shown to be robust to noise perturbation where some other super-resolution algorithms fail.

Chapter 5 continues the discussion of the impact of deconvolution on the CLEAN regenerated channel model. Comparisons are given between the channel statistics of the original channel and the CLEAN regenerated channel. Chapter 6 discusses the impact of possible pulse distortion from several mechanisms on the tap-delay line channel model. Chapter 7 provides an overall conclusion.

2 Channel Measurement and Channel Modeling

2.1 Channel Sounding Techniques

Radio communication channels can be generally classified as indoor (relatively short range, highly cluttered), stationary outdoor (relatively long range, some clutter), and mobile outdoor (similar to stationary but with dynamic characteristics). The focus of this work will be on stationary indoor channels (actually they are quasi-static channels due to the movement of people and objects in the environment, but these changes are assumed to occur very slowly relative to the data rate).

Because of the inherent randomness of wireless channels, modeling wireless channels is typically done in a statistical fashion based on measurements made specifically for an intended communication system and spectrum allocation. Much effort has already been taken to characterize indoor and outdoor radio propagation channels. The most applicable and commonly used models are based on realistic assumptions and reasonable theoretical explanations verified by extensive field measurements.

Channel modeling involves large scale modeling and small scale modeling, as we will discuss in detail in the following sections. The two types of modeling utilize the measurements in different ways. Large scale modeling is interested in predicting the mean signal strength for a given transmitter-receiver separation distance; it calculates the local average received power by averaging channel sounding measurements over a measurement track of 5λ to 40λ [7]. For small scale channel modeling, rapid

fluctuations in the received signal over the local area are of interest and the model includes the multipath structure of the channel (i.e. the channel impulse response). The characterization of the channel for both large and small scale modeling is done using channel sounding techniques.

A number of wideband channel probing techniques have been widely used to sound the channel. These techniques are typically classified as direct pulse measurements, spread spectrum sliding correlator measurements, and swept frequency measurements [7]. The overall concept of each of these techniques is to probe the channel with a suitable stimulus at one site and evaluate the response at another site in order to provide an estimate of the impulse response, which can in turn provide the most important information about the channel. A description and the tradeoffs involved with each of these measurement systems are presented here.

A simple channel sounding approach is the direct RF pulse system. The probing signal is detected with an envelope detector, and then digitally sampled, displayed and stored on a high speed digital sampling oscilloscope (DSO). The attraction of this system is its simplicity since off-the-shelf equipment is available. A block diagram of such a system is shown in Figure 2-1. The minimum resolvable delay between multipath components is approximated by the probing pulse width. The major drawback of this system is that it is subject to interference and noise, due to the wideband filter needed for multipath resolution. This can be somewhat mitigated by using averaging on the oscilloscope to obtain the local power delay profile. Proper and accurate triggering at the receiver can be

difficult, especially if the first pulse is blocked or greatly attenuated. Sometimes, a wired trigger may be necessary to provide a reliable reference. Another disadvantage of this system is that the phases of the individual multipath components cannot be retrieved, due to use of an envelope detector. However, we can obtain the phase information with the use of a coherent detector using this technique.

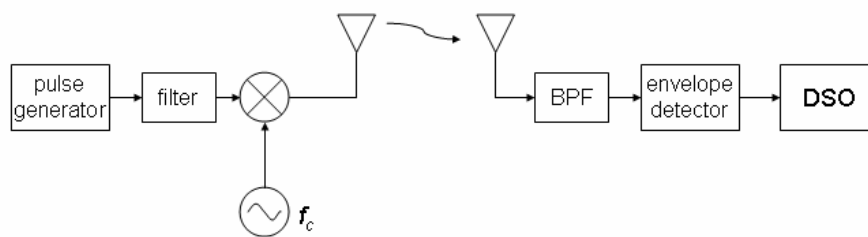


Figure 2-1 Traditional time-domain direct pulse measurement system

A block diagram of a spread spectrum sliding correlator channel measurement system is shown in Figure 2-2. This system uses a probing pulse of a sinusoidal carrier signal multiplied by a pseudo-noise (PN) sequence. Therefore, the probing signal has a wide null-to-null bandwidth of $2R_c$, where R_c is the chip rate. At the receiver, the received signal is filtered and then multiplied by the same PN sequence as used at the transmitter, although the chip rate at the receiver is slightly slower than the chip rate at the transmitter. When the PN sequence of the multipath component aligns with the PN sequence of the receiver, the receiver will have maximum correlation. Due to different chip rates, the PN sequence of the receiver slides past the PN sequences of the multipath components and provides a time expanded multipath profile of the channel. This measurement system has

the advantage of interference and noise rejection due to the processing gain of the spreading code. The time resolution of this system is $\Delta\tau = 2/R_c$.

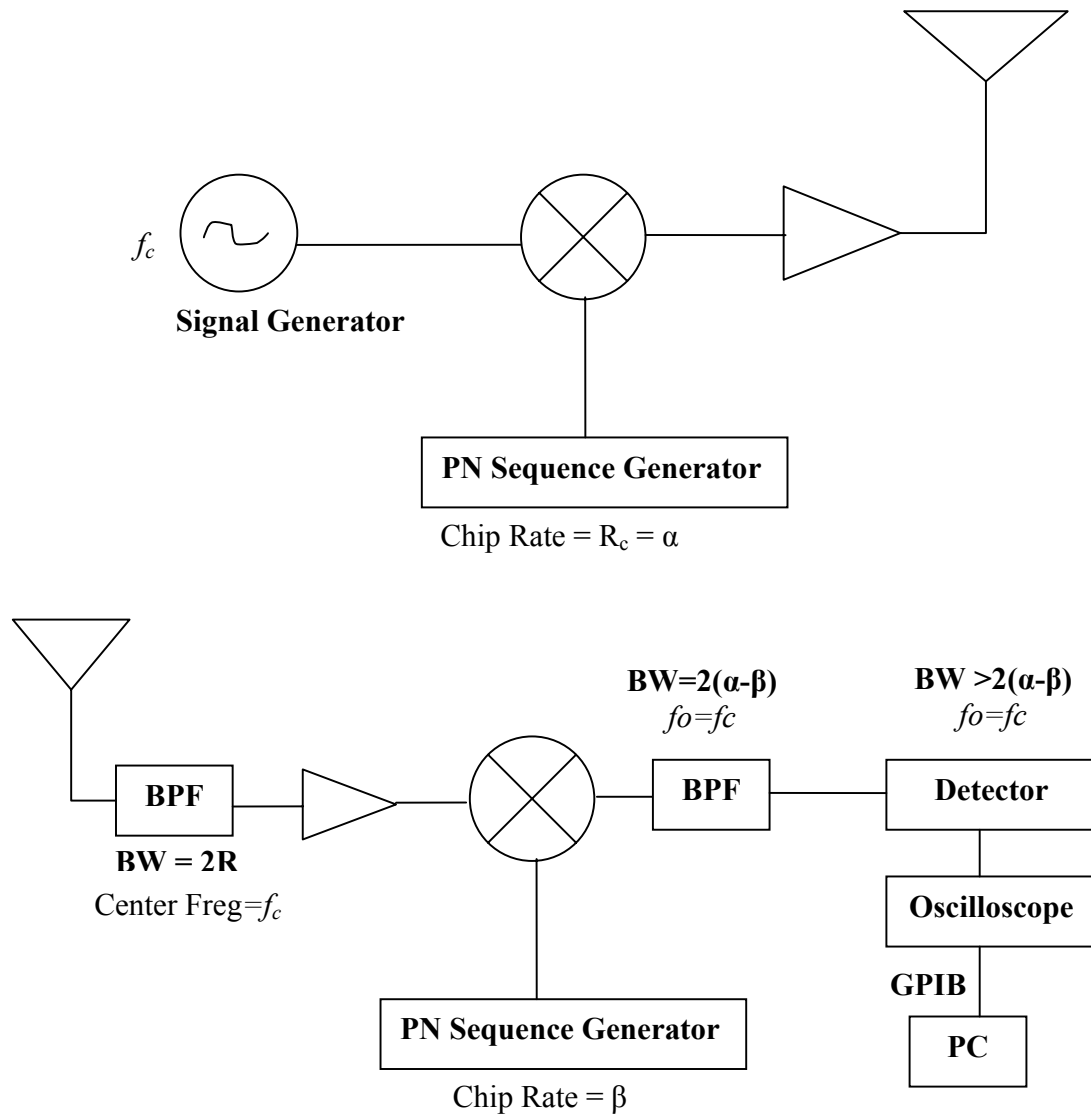


Figure 2-2 Spread Spectrum Sliding Correlator Channel Measurement system

Because of the dual relationship between time domain and frequency domain techniques, we can also measure the channel impulse response in the frequency domain. A frequency domain channel sounder, shown in Figure 2-3, uses a vector network analyzer (VNA) to measure the channel impulse response. The VNA measures the $S_{21}(\omega)$ s-parameter of the

channel over a given range of frequencies. $S_{21}(\omega)$ in this case also represents the frequency response of the channel: $H(\omega)$. Performing an inverse Fourier transform of the measured complex response, $H(\omega)$, produces the time domain impulse response of the radio channel: $h(t)$. This system requires a wired connection from each antenna to the VNA, so only short range measurements are practical for this measuring system. The impulse response obtained this way is bandlimited based on the bandwidth of the VNA. Also, performing impulse response measurements for time varying channels is difficult if the frequency sweep period of the measurement system is long compared to the changes in the channel, such as variations caused by the movement of objects in the propagation environment.

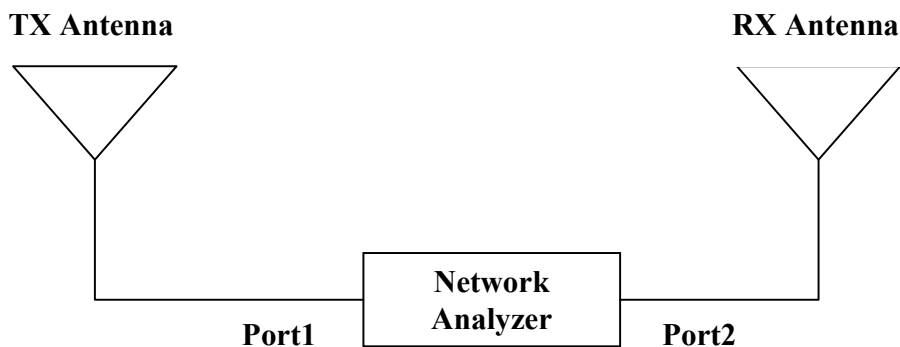


Figure 2-3 Vector Network Analyzer Measurement System

2.2 *Deterministic Channel Modeling vs. Statistical Channel Modeling*

Deterministic channel modeling, mainly utilizing ray-tracing techniques [34], is used for site-specific channel modeling. It attempts to model the exact interaction of the EM wave with the specific environment of interest. By comparison, statistical channel models

allow a general classification of the propagation environment properties by treating the channel parameters as random variables and modeling only the relevant statistics of the received signal. Deterministic channel models provide more accurate predictions of the radio wave propagation in a particular geometry over statistical channel models. Another advantage of a deterministic channel model is its reproducible behavior which is beneficial for easy comparison of different systems. However, deterministic channel modeling is computationally very intensive, contrary to virtually any statistical channel model. It is also difficult to accurately model all aspects of the environment. Thus the applications of deterministic modeling have been limited to a set of simplified geometries of rather small extents [35]. Statistical channel modeling is particularly useful in communication system development where the system must work in a wide variety of environments and where the performance is itself statistically characterized. It is the statistical modeling that we discuss in this thesis.

2.3 Large Scale Channel Modeling

The term “large scale” typically refers to the impact that the channel has on the transmitted signal over large distances and generally includes only average attenuation effects due to distance and large objects which are in the propagation path. Large scale modeling is concerned with predicting the mean signal strength for a given transmitter-receiver (T-R) separation distance, which is useful in estimating the radio coverage area of a transmitter.

For narrowband systems, when there is a clear, unobstructed line-of-sight (LOS) path between the transmitter and receiver, the free space received signal power is given by the Friis transmission equation

$$P_r(d) = \frac{P_t G_t G_r \lambda^2}{(4\pi)^2 d^2 L} \quad (2-1)$$

where d is the T-R separation distance in meters, P_t is the transmitted power, $P_r(d)$ is the received power, G_t is the transmit antenna gain, G_r is the receive antenna gain, L is the system loss factor not related to propagation ($L \geq 1$), and λ is the wavelength in meters.

The Friis free space equation is only valid for values of d which are in the far-field of the transmitting antenna. The far-field, or Fraunhofer region, of a transmitting antenna is defined as the region beyond the far-field distance d_f . The Fraunhofer distance is given by

$$d_f = \frac{2D^2}{\lambda} \quad (2-2)$$

where D is the largest physical linear dimension of the antenna.

The path loss, which represents signal attenuation as a positive quantity measured in dB, is defined as the difference (in dB) between the effective transmitted power and the received power, given by

$$PL(dB) = 10 \log_{10} \frac{P_t G_t}{P_r G_r} \quad (2-3)$$

In practice, a simpler approach to predict $P_r(d)$ rather than using Equation (2-1) is to estimate the received power based on a reference measurement $P_r(d_0)$ at distance d_0 in free space, given by

$$P_r(d) = P_r(d_0) \left(\frac{d_0}{d} \right)^2 \quad d \geq d_0 \geq d_f \quad (2-4)$$

However, the large bandwidth of UWB signals together with the Friis free space equation would suggest that the channel may distort the pulse and the Friis free space equation needs to be examined carefully before applying it to UWB. The analysis in [15] provides justification for applying the traditional path loss model to the analysis of UWB signals in free space. It showed that while the received power may be dependent on frequency, this is due to the antennas, not the path per se. The path loss in free space is not frequency dependent (it is defined independent of antennas used) [15], and the traditional narrowband models apply. Therefore, Equation (2-4) is applicable to UWB signals as the frequency dependence due to antenna effects is captured entirely in the reference measurement, $P_r(d_0)$.

For non-free space environments, the average received power needs to be modified as [7]

$$\overline{P}_r(d) = \overline{P}_r(d_0) \left(\frac{d_0}{d} \right)^n \quad (2-5)$$

where n is the path loss exponent and equals 2 in free space.

The path loss exponent n is typically determined by taking several measurements at various distances and performing a linear regression to obtain a least squares fit to the data. As in the free space case, the frequency dependence due to antennas is subsumed

into the reference measurement. However, it is still possible that the path loss exponent n could change with frequency due to the fact that diffraction, material penetration and other effects are frequency dependent. Currently, there is not a clear consensus on the dependence of path loss exponent n on frequency. Measurements from [15] [35] showed that the path loss exponent n does not vary with frequency. However, it should be noted that all the measurements were taken at relatively short distances. It is possible that larger distances may reveal frequency dependencies for NLOS channels due to frequency dependency of many materials.

The actual received power $P_r(d)$ observed at any given distance d will deviate from the average received power $\overline{P_r}(d)$ due to variations in the environment. This variation has been shown to follow a log-normal distribution in many measurements [7] [13] [14]. Thus the received signal power at a distance d can be modeled as

$$P_r(d)(dBm) = \overline{P_r}(d_0)(dBm) - 10n \log_{10}\left(\frac{d_0}{d}\right) + X_\sigma \quad (2-6)$$

where X_σ is a log-normal random variable with standard deviation σ .

The terms to be determined from the environments are the path loss exponent and the standard deviation of the shadowing. There are two ways to obtain these values. The most common way is to simply combine all measurements from similar environments and find the best fit to measured data [13] [15-17]. A second way is to determine the best fit for each specific environment and create a statistical model for the path loss exponent and shadowing deviation. In this approach [18] [19] the path loss exponent n is modeled as a

Gaussian random variable and the shadowing term X_σ is modeled as a lognormal random variable.

2.4 Small Scale Channel Modeling

Small scale channel modeling involves modeling small scale fading effects which include the local variation of the signal over short time or distance as well as the distortion of the transmitted waveform. Fading is caused by the interaction of multiple replicas of the transmitted signal at the receiver, and is also called multipath fading. Like path loss, small scale fading statistics are important metrics needed to effectively model a particular channel and facilitate the receiver design.

The small scale effects of the radio channel are commonly described by a time-varying linear filter and the received signal is given by

$$r(t) = s(t) * h(t, \tau) + n(t) \quad (2-7)$$

where $s(t)$ is the transmitted signal, $h(t, \tau)$ is the time varying channel impulse response, and $n(t)$ is additive Gaussian noise. If the channel is assumed to be static over the time interval of interest, the channel model is typically modeled as a time-invariant linear filter:

$$h(\tau) = \sum_{k=0}^{N-1} \alpha_k e^{j\theta_k} \delta(\tau - \tau_k) \quad (2-8)$$

The parameters of this model are as follows:

- δ is the Dirac delta function
- N is the number of resolvable multipaths
- τ_k are the arrival times of the multipaths

- distributions used to describe arrival times are:
 - Standard Poisson Model
 - Modified 2-State Poisson Model (Δ -K Model)
 - Modified Poisson (Weibull Interarrivals)
 - Double Poisson (Saleh-Valenzuela /Neyman-Scott)
- α_k are the path amplitude values
 - distributions used to describe amplitude values are:
 - Rayleigh
 - Rician
 - Lognormal
 - Nakagami (m-distribution)
 - Weibull
 - Suzuki
 - The distribution used to model the relative average values of the successive multipath component powers is an exponential decay within a cluster
- θ_k are the path phase values
 - the initial phase is a uniformly distributed random variable on $[0,2\pi)$
 - phase value is incremented by:
 - random Gaussian variable
 - deterministic value calculated from environment
 - θ_k only takes value of 0 and π as path polarity for baseband UWB channel modeling

Besides specific statistical channel multipath parameters, the channel can also be characterized by coarse statistics such as mean excess delay, RMS delay spread, and maximum excess delay that describe the time dispersive properties of the channel. These are useful as single number descriptions of the channel to estimate the performance and potential for intersymbol interference (ISI). These values tend to increase with greater transmitter/receiver separation. The mean excess delay is defined as [7]

$$\tau_m = \frac{\sum_k \alpha_k^2 \tau_k}{\sum_k \alpha_k^2} \quad (2-9)$$

RMS delay spread is defined as

$$\tau_{RMS} = \sqrt{\frac{\sum_k \alpha_k^2 \tau_k^2}{\sum_k \alpha_k^2} - \tau_m^2} \quad (2-10)$$

Various channel models have been developed to characterize the discrete channel impulse response, such as the Saleh-Valenzuela model, Δ -K model, etc. We will give a detailed description of the commonly used Saleh-Valenzuela model in Chapter 5.

Whether we want the specific channel multipath parameters in Equation (2-8) or the coarse parameters mentioned above, we need to have the channel impulse response on hand for further analysis and modeling. The channel impulse response is not readily available directly from the channel sounding measurements, which are convolution of

transmitted waveform, transmit antenna, channel and receive antenna. Thus, the separation of the channel impulse response from the measurements typically requires deconvolution. The following chapter is dedicated to different deconvolution techniques (both frequency and time domain) and their advantages and disadvantages.

3 Deconvolution Techniques

3.1 Introduction

Deconvolution is usually defined as a mathematical operation which is the inverse of a convolution operation, i.e. the operation of solving for $f(t)$ where $y(t) = f(t) * g(t)$ given $y(t)$ and $g(t)$ or only $y(t)$; the latter is more complicated and is usually referred to as blind deconvolution [20]. Deconvolution is a very powerful signal processing technique and is widely used in many applications. In seismic processing, $y(t)$ represents a series of acoustic reflections of an explosively generated signal due to rock inhomogeneities and $g(t)$ models the earth medium [21]. In image processing, which is crucial to astronomy, medical images, etc, the same problem arises for two-dimensional signals in which the two-dimensional version of $f(t)$ represents an image, while the two-dimensional version of $g(t)$ models a distortion due to a poor lens, for example [22]. The deconvolution problem is mathematically classified as an ill-posed problem [23]. By Hadamard's definition, a problem is well posed if a unique solution exists and the solution depends continuously on the data; otherwise, it is ill posed. Ill-posedness occurs in problems where the data or equations are inexact, i.e., they are only approximates. Consequently, the information represented by the data, or the equations are incomplete. Thus, there may not exist unique solutions to the deconvolution problem.

For this class of problems, more than one approximate solution may be achieved, some of which are "acceptable" estimates to the exact solution, and some of these acceptable solutions are just "better" estimates than others [23]. In selecting the "acceptable"

estimate for an ill-posed problem, subjective judgment must be made [24]. This subjective judgment acts as a substitute to the problem's missing information.

In the communications area, the extraction of the channel impulse response inevitably involves deconvolution. Assuming a time-invariant linear filter channel model, the received signal $y(t)$ is the convolution of the transmitted signal $x(t)$ and the channel impulse response $h(t)$ corrupted by white Gaussian noise $n(t)$. The mathematical model is given below:

$$y(t) = x(t) * h(t) + n(t) \quad (3-1)$$

By measuring $y(t)$ and $x(t)$, we want to deconvolve $h(t)$ to characterize the channel. This can be done in both frequency domain and time domain. We will discuss each approach in detail in the following sections.

3.2 Frequency Domain Techniques

3.2.1 Inverse filtering

In the frequency domain, the most straight forward deconvolution technique is known as inverse filtering [25]. Time domain convolution transforms into multiplication in the frequency domain, and using $X(j\omega)$, $H(j\omega)$ and $Y(j\omega)$ to denote the frequency domain forms of $x(t)$, $h(t)$ and $y(t)$ respectively, assuming no noise for now, Equation (3-1) transforms to

$$Y(j\omega) = X(j\omega) \cdot H(j\omega) \quad (3-2)$$

From (3-2), the frequency deconvolution representation is derived as

$$H(j\omega) = Y(j\omega) / X(j\omega) \quad (3-3)$$

Ideally, with the exact and complete knowledge of $X(j\omega)$ and $Y(j\omega)$, deconvolution can be exactly performed to compute $H(j\omega)$. By taking the inverse Fourier transform of $H(j\omega)$, we can get the perfect estimate of the discrete channel impulse response $h(t)$. Inverse filtering is a very simple algorithm to implement. However, in practice, the inverse filtering is highly unstable and inaccurate. When $Y(j\omega)$ is noisy, at frequencies where $X(j\omega)$ is small the estimate of $H(j\omega)$ will be unreliable and even undefined where $X(j\omega) = 0$. Therefore, $H(j\omega)$ at these frequencies can be zeroed out to minimize the impact of noise and make the algorithm stable.

$$H(j\omega) = \begin{cases} \frac{Y(j\omega)}{X(j\omega)}, & |X(j\omega)| > \text{threshold} \\ 0, & |X(j\omega)| < \text{threshold} \end{cases} \quad (3-4)$$

The continuous impulse response $h_c(t)$ is simply the inverse Fourier transform of $H(j\omega)$. This method effectively bandlimits the estimated signal $H(j\omega)$. Thus $h_c(t)$ will be the convolution of the true $h(t)$ and a sinc function. By taking the amplitude and time delay of the peak of $h_c(t)$ by inspection or according to some threshold rules (local maximum greater than 0.2 of the global maximum and/or keeping some number of most significant paths) [25], an estimate of discrete channel impulse response $h(t)$ can be derived.

Care must be taken when choosing the threshold for $H(j\omega)$. $h_c(t)$ will have a narrower mainlobe but bigger sidelobes when the threshold is bigger and a wider mainlobe but smaller sidelobes when the threshold is smaller. The narrow mainlobe is desirable for

pulse resolution while small sidelobes are desirable for false pulse rejection (large sidelobes may be mistaken as multipaths). Depending on the signal-to-noise-ratio (SNR) of the received signal, we need to choose this threshold carefully.

Generally speaking, the lower the SNR, the smaller the threshold should be. In practice, it would be beneficial to use the transmitted pulse, synthetic channel impulse response and estimated noise level to run some simple simulations to determine the appropriate threshold. To review the deconvolution accuracy and compare different thresholds, the reconstructed received signal $y'(t)$ (derived from corrupted signal $y(t)$ with different SNR values), and the simulated received signal (before adding Gaussian noise) $y_{noise\ free}(t) = x(t) \otimes h(t)$, are correlated. Table 3-1 gives an example of the correlation with different SNR values and thresholds when using a synthetic transmitted signal of a Gaussian pulse.

Table 3-1 Correlation comparison of Inverse Filtering using different thresholds at different SNRs

Threshold(dB) \ SNR (dB)	10	15	20	25	30	35	40
10	0.9618	0.9926	0.9944	0.9917	0.9500	0.9573	0.8801
20	0.9618	0.9920	0.9945	0.9949	0.9958	0.9871	0.9686
30	0.9620	0.9920	0.9956	0.9967	0.9956	0.9950	0.9857

As seen from Table 3-1, the optimum threshold for various SNR is in the range of 15-25 dB, and the high correlation shows that this modified frequency division deconvolution works reasonably well because the neglected parts of $H(j\omega)$ comprise relatively little energy [25]. An example of the transmitted Gaussian pulse, synthetic channel impulse response, received signal with SNR of 20dB, deconvolved channel impulse response

$h_c(t)$ using threshold of 25dB and the discrete impulse response $h(t)$ are given in Figure 3-1, Figure 3-2, Figure 3-3, and Figure 3-4 respectively.

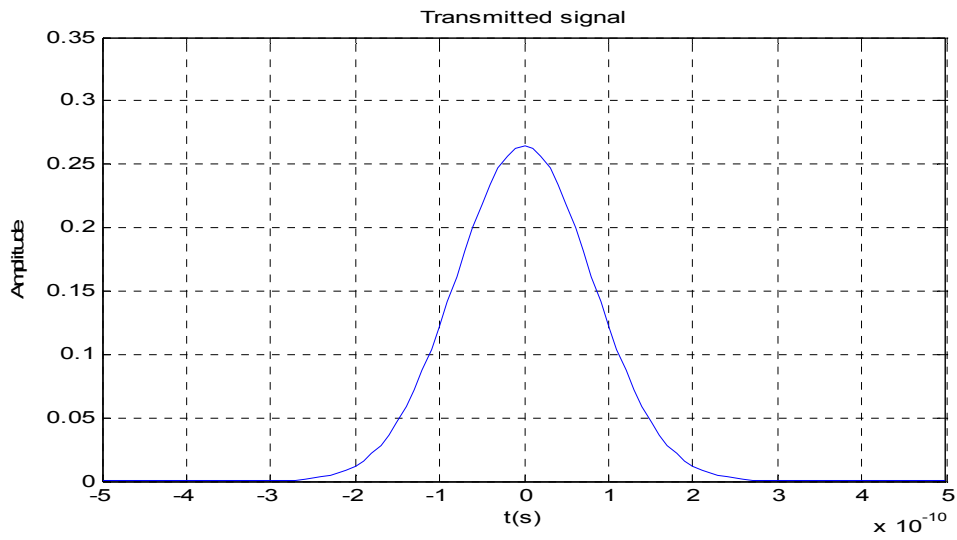


Figure 3-1 Transmitted Gaussian Pulse

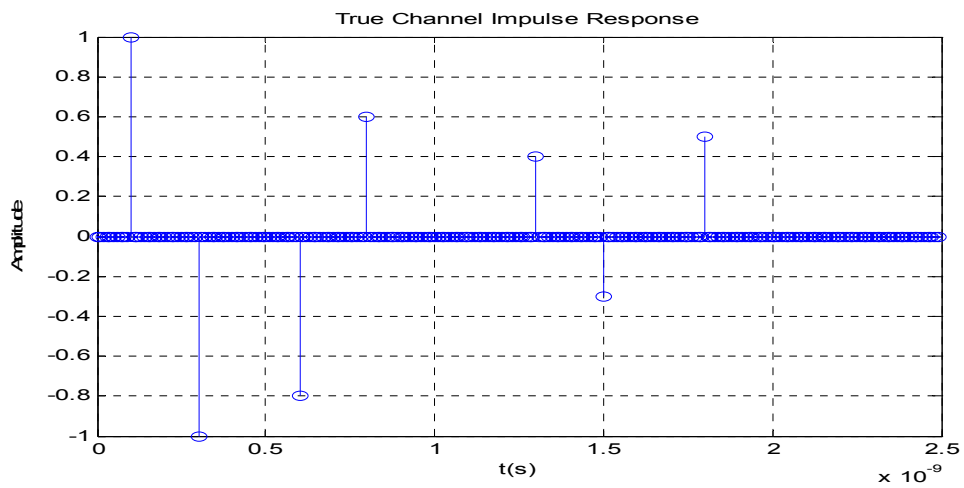


Figure 3-2 True Channel impulse response

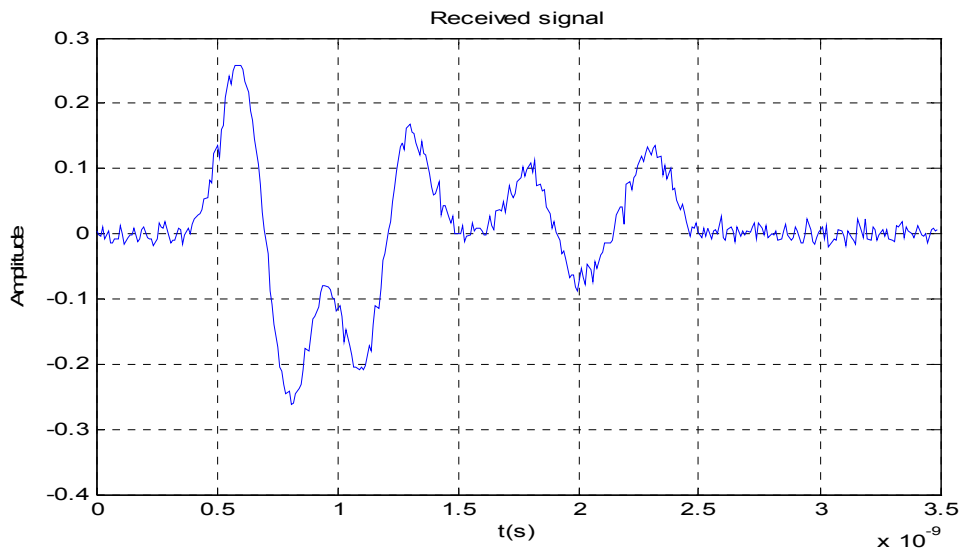


Figure 3-3 Received signal with SNR of 20dB

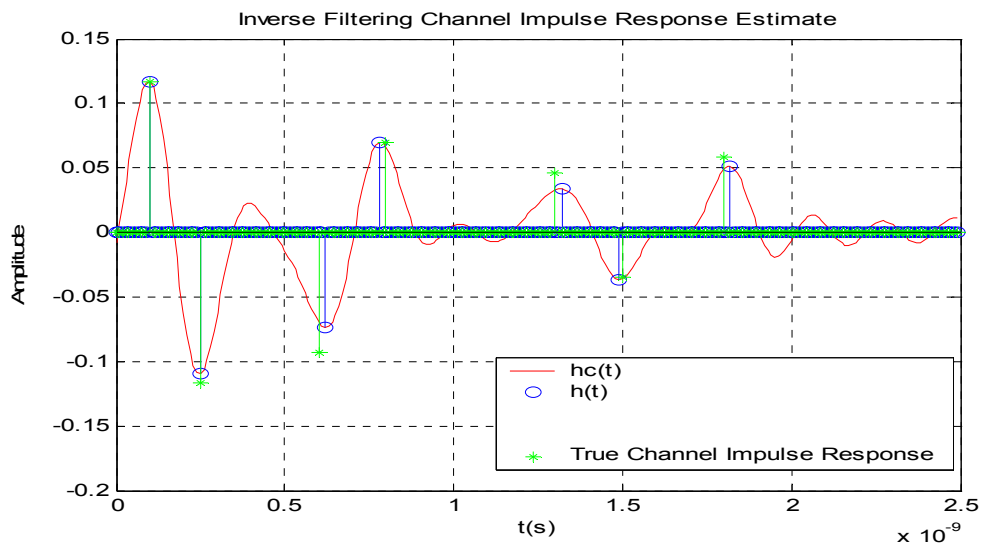


Figure 3-4 Continuous and discrete inverse filtering estimate of channel impulse response

In Figure 3-4, the true channel impulse responses are scaled for easy comparison with the inverse filtering deconvolution result. From Figure 3-4, we can see that the improved inverse filtering deconvolution estimates are pretty accurate compared to the true values. As presented in Table 3-1, the correlation is as high as 0.9949 for this case. One thing to notice is that the amplitudes of impulse response derived from inverse filtering are

smaller than the true values while the delay estimates are pretty accurate. This is because when we discretize the continuous channel impulse response, we discard part of the energy. Thus the amplitude is reduced. However, the relative amplitudes still remain.

3.2.2 Van-Cittert deconvolution

The Van-Cittert iterative deconvolution technique was first proposed and has been widely used as a time domain technique [26]. In the technique, the initial estimate $h_0(t)$ of channel impulse response $h(t)$ is set to be the received waveform $y(t)$, and successive estimate $h_i(t)$ is obtained iteratively by adding an error correction term to the previous iteration of $h_{i-1}(t)$:

$$h_i(t) = h_{i-1}(t) + [y(t) - h_{i-1}(t) * x(t)] \quad (3-5)$$

with $h_0(t) = y(t)$

This iterative process is somewhat intuitive and ideally, is ended whenever $h_i(t) * x(t) = y(t)$, which necessarily yields $h_i(t) = h(t)$.

The technique is very time consuming due to convolution performed at each iteration. Reference [26] proposed a Van-Cittert deconvolution procedure in the equivalent frequency domain. By turning the convolution into multiplication at each iteration, computation is reduced dramatically. Viewing this technique in the frequency domain is more helpful because of the Wiener-type filtering nature of this technique [26]. The conditions for the convergence of the Van-Cittert technique can be obtained in the frequency domain.

Taking the Fourier transform of (3-5), we obtain

$$H_i(f) = H_{i-1}(f) + [Y(f) - X(f)H_{i-1}(f)] \quad (3-6)$$

with $H_0(f) = Y(f)$

After successive substitutions, (3-6) yields the sequence:

$$H_i(f) = \{1 + [1 - X(f)] + [1 - X(f)]^2 + \dots + [1 - X(f)]^i\} Y(f) \quad (3-7)$$

From Equation (3-7), it can be seen that the sequence of $H_i(f)$ converges to the ratio $Y(f)/X(f)$ when $|1 - X(f)| < 1$. The Van-Cittert technique can actually be applied to any practical cases even when the convergence condition $|1 - X(f)| < 1$ is not satisfied by introducing parameter scaling and reblurring procedures [26]. The Van-Cittert procedure (i.e., Equation (3-6)) is then modified as

$$H_i(f) = H_{i-1}(f) + [\tilde{Y}(f) - \tilde{X}(f)H_{i-1}(f)] \quad (3-8)$$

$$H_0(f) = \tilde{Y}(f)$$

where

$$\tilde{Y}(f) = \frac{CX^*(f)Y(f)}{\max[|X(f)|^2]}$$

$$\tilde{X}(f) = \frac{CX^*(f)X(f)}{\max[|X(f)|^2]} = \frac{C|X(f)|^2}{\max[|X(f)|^2]}$$

where C is a constant less than 1.

To view the filtering nature of the Van-Cittert technique more clearly, we rewrite (3-8) as

$$H_i(f) = H_r(f) \cdot B(f) \quad (3-9)$$

where

$$H_r(f) = \tilde{Y}(f) / \tilde{X}(f) = Y(f) / X(f)$$

$$B(f) = 1 - [1 - \tilde{X}(f)]^{i+1}$$

For $i \rightarrow \infty$, $B(f)$ approaches unity at all frequencies as an all-pass filter (since the convergence condition $|1 - \tilde{X}(f)| < 1$ is guaranteed by the scaling and reblurring procedure). In this case, Van-Cittert deconvolution is the same as direct inverse filtering (without zeroing out certain frequencies). For a finite i , $H_r(f)$ is modified by a factor that suppresses its values at frequencies where $\tilde{X}(f)$ is small (i.e., regions with low SNR) [26]. The suppression is very high for small i and affects the entire frequency response of the signal. The filter acts as a stop-band over most frequencies. The optimum filter performance can be obtained with a large but not infinite number of iterations. However, the Van-Cittert technique doesn't tell what the optimum number of iterations is. The Bennis-Riad optimization criterion for iterative deconvolution can be jointly used with the Van-Cittert technique to optimize the number of iterations required to achieve acceptable (optimum) deconvolution results [26].

The Bennis-Riad optimization method suggests breaking the signal into a pass band (information region where $X(f)$ has significant energy) and stop band (noise region where $X(f)$ is negligible). For each band, the standard deviation of the difference $\{H_i(f) - H_{r(\text{same as } i=\infty)}(f)\}$ is normalized to a unity maximum value and can be plotted versus the number of iterations i . It is desirable that the standard deviation is minimum in the pass band and maximum in the stop band. The optimum estimate implies that

$H_{opt}(f)$ is well matched in the desired frequency range and minimized in the noise dominated stop band.

The same synthetic data used in inverse filtering section are used here to demonstrate the Van-Cittert deconvolution technique and the Bennis-Riad optimization criterion. The transmitted signal, synthetic channel impulse response and the received signal with SNR of 20dB are shown in Figure 3-1, Figure 3-2 and Figure 3-3 respectively.

The computed transfer function of the system under test is shown in Figure 3-5. In the figure, three cases are shown: the case of 2000 iterations, 20000 iterations, and the case of no filter (direct inverse filtering which is the same as the case of an infinite number of iterations). It can be seen from the figure that increasing the number of iterations increases the bandwidth of the filter. This results in a simultaneous increase in information content as well as the noise content.

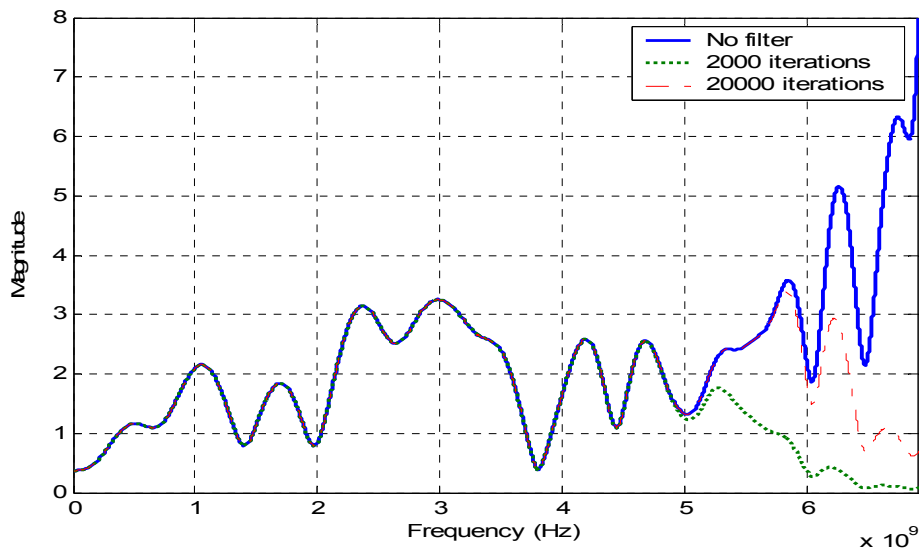


Figure 3-5 Magnitude of the transfer function using direct division and the deconvolution filter with different filtering levels (number of iterations)

A more direct view of the filtering nature of the Van-Cittert technique is shown in Figure 3-6. The figure plots the magnitude of the filter response $B(f)$ in Equation (3-8). The figure demonstrates the adaptive nature of this filter with its pass-band coinciding with the information frequency band and its stop-band affecting the noise interval. The number of iterations clearly affects the filter's bandwidth. The larger the number of iterations, the wider the filter's bandwidth is, although this does not necessarily improve the accuracy of the deconvolution result. We need to trade off between the fidelity of the signal and the noise content.

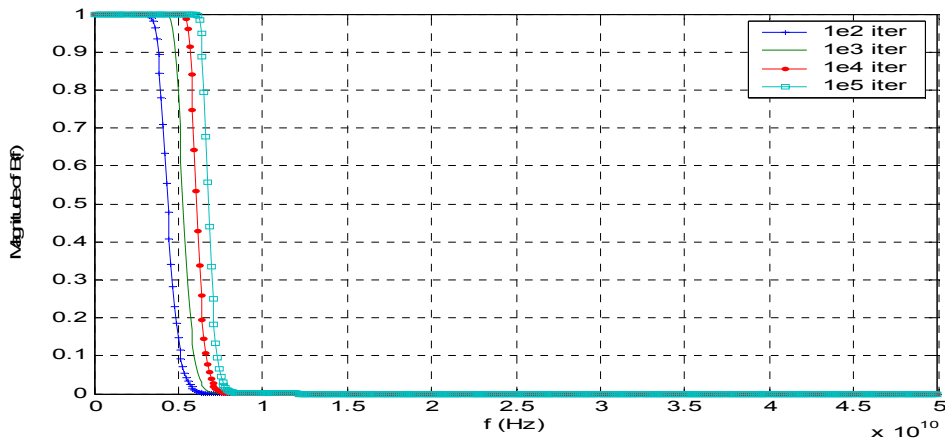


Figure 3-6 Magnitude of the deconvolution filter using different number of iterations

To apply the Bennis-Riad optimization criterion, the frequency band of interest is divided into two major intervals: the first interval is pass band where the power spectrum of the information signal $X(f)$ is above -25dB of its maximum, the second is the stop band where the power spectrum of $X(f)$ is between -25dB and -100dB. The standard deviation for each frequency band is computed for various numbers of iterations. The results were then normalized to a maximum of unity for each frequency band respectively.

Figure 3-7 shows the results versus the number of iterations i. Figure 3-8 gives a closer look at the standard deviation in the stop band.

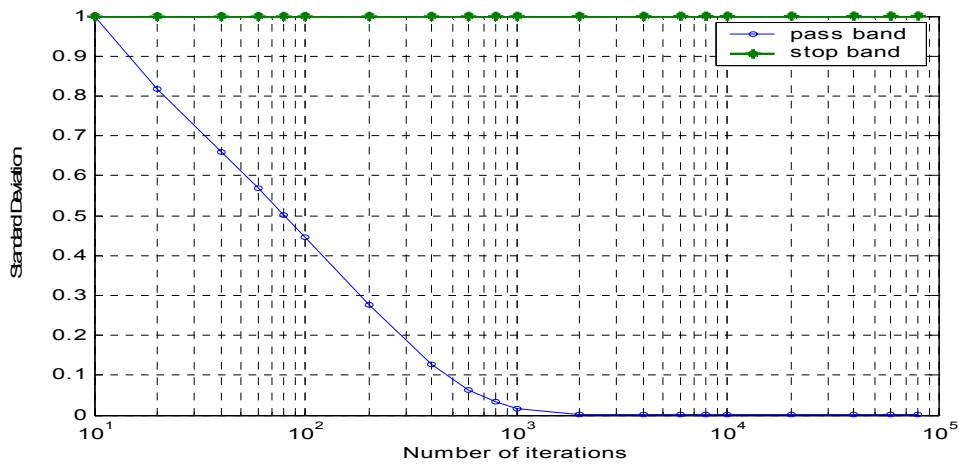


Figure 3-7 Results of frequency domain optimization criteria

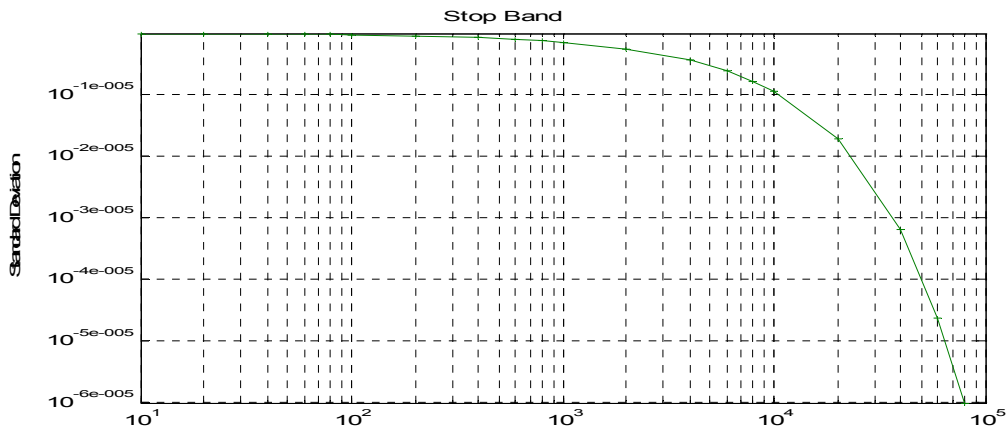


Figure 3-8 Closer look at the results of frequency domain optimization criteria in stop band

In Figure 3-7, the decline of the pass band curve is an indication of the continued improvement in the deconvolution accuracy as the number of iterations increases. The improvement stops after about 4000 iterations as the standard deviation in this region is a constant zero, which means that in the information band we have the information we need. On the other hand, the stop band curve begins to decrease after 20000 iterations as

seen from Figure 3-8, which means after 20000 iterations the estimate $H_i(f)$ contains some noise content. So the acceptable deconvolution estimates are obtained for a number of iterations between 4000 and 20000. The comparison of deconvolution result, $h(t)$, for a small, optimum and large number of iterations is shown in Figure 3-9. To examine the accuracy of the deconvolution result using the optimum number of iteration, the result is compared with the true channel impulse response in Figure 3-10. For easy comparison, the true channel impulse response is normalized with respect to the computed deconvolution result.

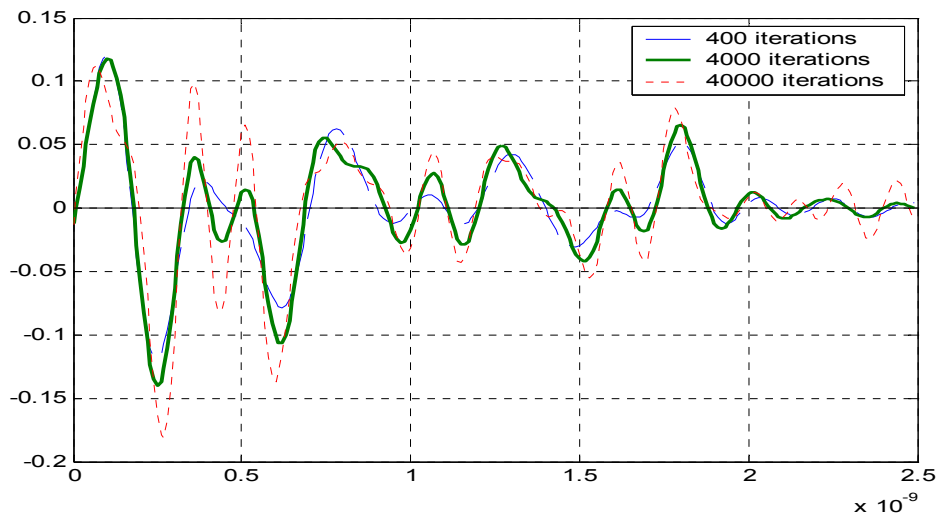


Figure 3-9 Comparison of impulse response obtained using different number of iterations

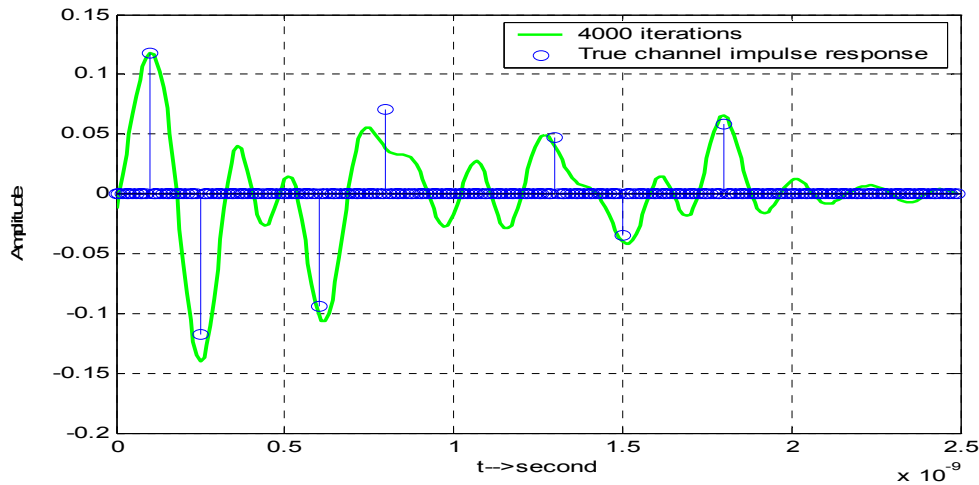


Figure 3-10 Comparison of Van-Cittert deconvolution result using Bennis-Riad optimization criterion and the true channel impulse response

Comparing Figure 3-10 with Figure 3-4, it can be seen that the result using Van-Cittert technique with Bennis-Riad optimization criterion is not as accurate as the improved inverse filtering. It is worth noting that both inverse filtering and Van-Cittert deconvolution has the capability of super-resolution as seen from Figure 3-4 and Figure 3-10 (recall that transmitted pulse width is about 0.6 ns and the taps are separated by as closely as 0.2 ns). The notion of super-resolution and more detailed discussion will be given in Chapter 4. If we discretize the deconvolution result $h(t)$ by picking the local maximum peaks of the continuous waveforms, we may end up with either picking false peaks or omitting some real peaks. So the Van-Cittert method is not suitable for our purposes.

3.3 Time domain technique: CLEAN algorithm

The CLEAN algorithm is a widely used time domain deconvolution technique. The CLEAN algorithm, first introduced in [27], and well established in the radio astronomy

and microwave communities has been applied to impulsive UWB measurements in [1, 11, 12, 28, 29]. The CLEAN algorithm is preferred because of its ability to produce a discrete CIR in time. In other words, it assumes that the channel is a series of impulses, consistent with the commonly assumed tapped-delay line channel model [7] [8] as:

$$h(t) = \sum_{k=0}^{N-1} \alpha_k \beta_k \delta(t - \tau_k) \quad (3-10)$$

where N is the number of scaled α_k and time-delayed τ_k paths in the channel and β_k is the polarity associated with each path.

The received signal $y(t)$ from propagation measurements can be represented as

$$y(t) = p_{rx,LOS}(t) * h(t) \quad (3-11)$$

where $p_{rx,LOS}(t)$ is pulse shape received along the LOS path and can be isolated from a LOS measurement via time gating. Note that the resulting pulse shape includes the effects of the transmit and receive antennas.

To extract the CIR from measurements of the received waveform $y(t)$, we first need to take an LOS measurement to obtain the template for the CLEAN algorithm. The algorithm searches the received waveform iteratively with the template to find the maximum correlation [5]. The steps involved are:

1. Calculate the autocorrelation of the template $r_{ss}(t)$ and the cross-correlation of the template with the received waveform $r_{sy}(t)$
2. Find the largest correlation peak in $r_{sy}(t)$, record the normalized amplitudes α_k and the relative time delay τ_k of the correlation peak.

3. Subtract $r_{ss}(t)$ scaled by α_k from $r_{sy}(t)$ at the time delay τ_k .
4. If a stopping criterion (a minimum threshold on the peak correlation) is not met, go to step 2. Otherwise, stop.

To get a general idea of CLEAN performance on deconvolution accuracy, we use the same synthetic data as used in frequency domain technique section to demonstrate the technique.

The transmitted signal, true channel impulse response and the received signal with an SNR of 20dB are shown in Figure 3-1, Figure 3-2 and Figure 3-3 respectively.

The CLEAN deconvolution result using CLEAN threshold of 15dB compared with the true channel impulse response is shown in Figure 3-11.

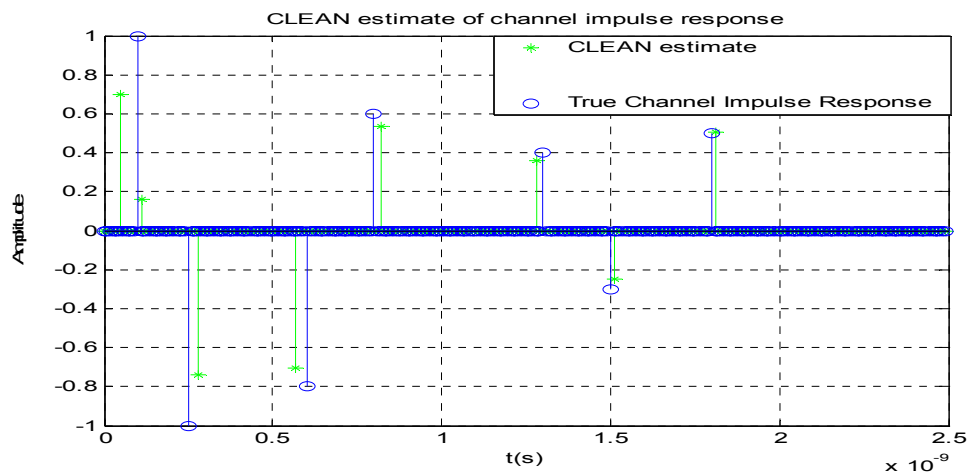


Figure 3-11 CLEAN deconvolution result

The transmitted pulse width is approximately 0.5 ns. When arriving pulses are separated by much less than the pulse width as the first four pulses are, CLEAN generates close but not the exact time delay and the corresponding amplitude. CLEAN will give perfect estimates when arriving pulses are resolvable and noise is reasonable. The correlation of

the reconstructed received signal using CLEAN generated taps and the originally received signal without noise is 0.9787. This correlation will improve as we increase the CLEAN threshold, and the correlation is 0.9965 when the threshold is 30dB. As the threshold increases, CLEAN will generate more paths to represent the noise and distortion of the signal. Depending on our interest (to better represent the distorted and noise corrupted signal or to have a more accurate estimate of the real paths), we can choose the CLEAN threshold accordingly. CLEAN is more resistant to noise perturbation than inverse filtering. As the SNR goes from 20dB to 0dB, the correlation between the received signal and reconstructed received signal using inverse filtering deconvolution decreases from 0.9949 to 0.9231, while the correlation using CLEAN decreases from 0.9787 to 0.9481.

A more thorough discussion of CLEAN will be presented in the next two chapters.

4 Performance of CLEAN

4.1 Delay/Amplitude Estimate Performance

The goal of this section is to examine the accuracy of the CLEAN algorithm in extracting the CIR for different stopping criteria. CLEAN has been characterized using simulated impulse response data to define its performance limits. The signal-to-noise ratio (SNR) of a typical measured LOS pulse in the data sets we have considered is about 50dB while the average SNR of the non-line-of-sight (NLOS) measurements is from 10dB to 30dB [13]. The SNR here is defined as SNR per pulse. Thus, we will also examine these ranges of SNR in our simulation analysis.

Synthetic data was created by assuming an LOS pulse and a discrete tap impulse response for the channel. The received signal was then created by convolving the pulse with the channel impulse response and adding noise. The LOS pulse assumed is a Gaussian pulse with 1 GHz bandwidth and a center frequency of 4 GHz, shown in Figure 4-1. The pulse duration is about 1 ns.

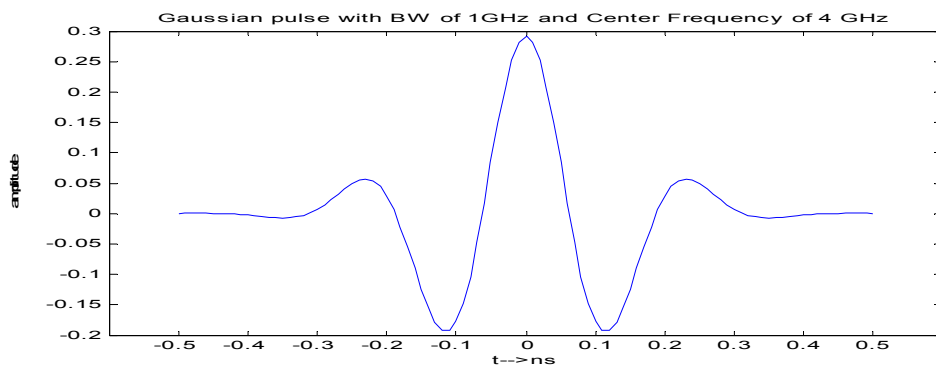


Figure 4-1 Simulated LOS Pulse

The received LOS pulse is the transmitted pulse corrupted by additive white Gaussian noise (AWGN) with an SNR of 50dB. This is used as the template in the CLEAN algorithm.

First, we assume the CIR is a two tap channel and the signal is received with infinite SNR. The separation between the two taps is 1 ns, meaning that the multipath components are resolvable. The amplitude of the first tap is $\sqrt{0.6}$ and the amplitude of the second tap is $\sqrt{0.4}$ (note we assume the channel has unity energy). It can be shown that the CLEAN algorithm generates a perfect estimate of the CIR in the absence of noise if the two paths are resolvable. Thus, we are more interested in the scenario where the delay is less than the pulse duration. Table 4-1 presents the Mean Square Error (MSE) between the regenerated and original CIR as the delay between the paths varies between 0 and 1ns in absence of noise. The MSE is defined as the energy of the difference between the true CIR and CLEAN reconstructed CIR divided by the length of the CIR.

Table 4-1 MSE of Estimated Two Tap CIR for various Delays (SNR is infinite)

Delay (ns)	0.1	0.2	0.3	0.4	0.5	0.6	0.7	0.8	0.9	1
MSE of CIR	0.0141	0.0195	0.0169	4.5171e-5	0.3892e-5	0.0076e-5	0	0	0	0

Recall that the pulse width is 1 ns. CLEAN can produce a perfect estimate of the CIR even when the delay is only 0.7 ns, which means the two paths are not completely resolvable. In fact, the MSE is very low even for relative delays as low as 0.4 ns. CLEAN clearly has sub-pulse-width resolution in the absence of noise.

We next examine the impact of noise on the algorithm. Path thresholds of 15dB and 20dB for the CLEAN algorithm were both examined. A sample of the CLEAN estimation of the CIR is plotted in Figure 4-2. Example comparisons of the reconstructed signal, actual received signal and the desired part of received signal at an SNR of 10dB for path threshold of 15 dB are shown in Figure 4-3 and Figure 4-4.

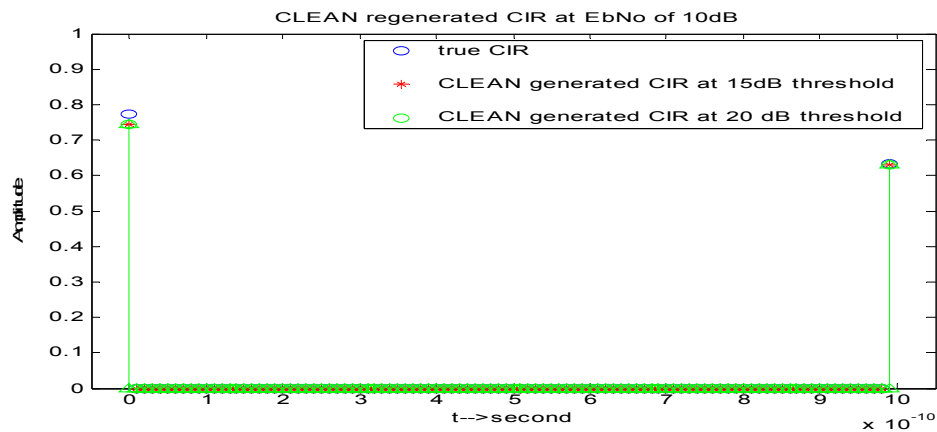


Figure 4-2 Sample of CLEAN estimate of CIR when paths are resolvable

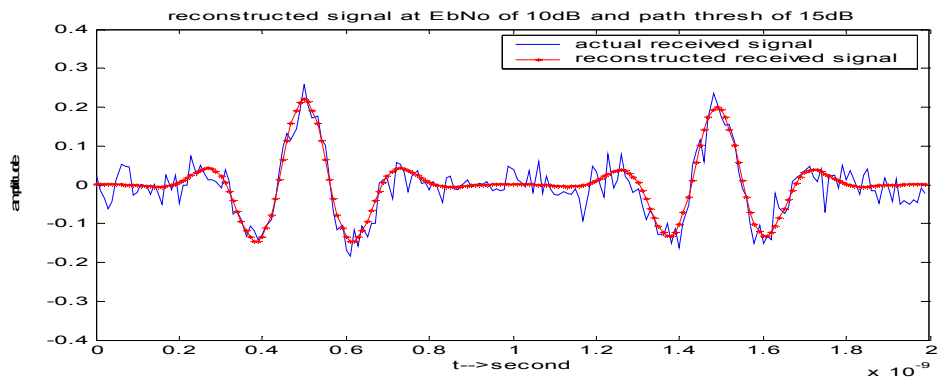


Figure 4-3 Sample of comparison of reconstructed received signal and actual received signal when paths are resolvable

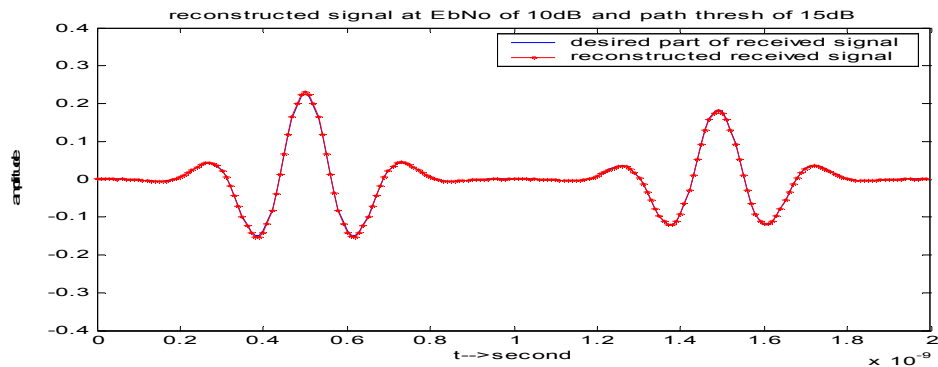


Figure 4-4 Sample of comparison of reconstructed received signal and desired part of received signal when paths are resolvable

As can be seen from the above figures, CLEAN is fairly accurate at representing the true signal at even moderately low SNR (recall that most measurements used have an SNR of 10dB to 30dB) when the paths are resolvable. While MSE of the CIR is the direct measure of the algorithm's accuracy, a comparison between the CLEAN regenerated received signal and the actual received signal will be more useful when the MSEs of CIR for different thresholds are very close or we are more interested in the received waveforms rather than the CIR. Here, we define two additional measures to characterize the accuracy of CLEAN, relative error and correlation. The relative error between the received signal and the reconstructed received signal is defined as the ratio of the energy of the difference between the two signals to the energy of the received signal. The relative error between the desired part of the received signal (i.e., excluding noise) and the reconstructed received signal is defined as the ratio of the energy of the difference between the two signals to the energy of the desired part of received signal. A comparison of the relative error and correlation between the estimated signal, the received and the desired part of received signal for different SNRs and path thresholds is shown in Table 4-2 and Table 4-3 respectively.

Table 4-2 CLEAN performance at different SNR when we consider the actual received signal if paths are resolvable

SNR (dB)	10	15	20	25	30
MSE of CIR 1e-4 (15dB/20dB threshold)	0.6668/ 0.7986	0.0626/ 0.0628	0.0200/ 0.0200	0.0063/ 0.0063	0.0020/ 0.0020
Relative Error (15dB/20dB threshold)	0.1641/ 0.1630	0.0584/ 0.0584	0.0192/ 0.0192	0.0062/ 0.0062	0.0020/ 0.0020
Correlation (15dB/20dB threshold)	0.9142/ 0.9148	0.9704/ 0.9704	0.9903/ 0.9903	0.9969/ 0.9969	0.9990/ 0.9990

Table 4-3 CLEAN performance at different SNR when we consider the desired received signal if paths are resolvable

SNR (dB)	10	15	20	25	30
MSE of CIR 1e-4 (15dB/20dB threshold)	0.6144/ 0.7542	0.0693/ 0.0697	0.0201/ 0.0201	0.0062/ 0.0062	0.0020/ 0.0020
Relative Error (15dB/20dB threshold)	0.0021/ 0.0035	0.0006/ 0.0006	0.0002/ 0.0002	0.0001/ 0.0001	0.0000/ 0.0000
Correlation (15dB/20dB threshold)	0.9994/ 0.9988	0.9998/ 0.9998	0.9999/ 0.9999	1.0000/ 1.0000	1.0000/ 1.0000

CLEAN is pretty accurate at representing the desired signal even at low SNR when the paths are resolvable. It can be seen from the MSE of the CIR that a path threshold of 15dB for the CLEAN algorithm performs better than 20dB at low SNR and the same as 20dB threshold at moderate SNR. This is due to the fact that the actual multipath components are fairly strong. Thus, the higher threshold will capture more noise.

It is worth noting that the error between the reconstructed signal and desired received signal is much smaller than the error between the reconstructed signal and actual received signal. This is because CLEAN doesn't represent the noise in the signal at the thresholds used. It also implies that when we calculate the relative error from measurements, the calculated error will actually be significantly larger than the true error since we can't extract the desired part of the received signal. We can only calculate the relative error

between the noisy received signal and CLEAN reconstructed signal, which magnifies the error since it includes noise. A path threshold of 15dB has better performance when we consider the desired part of the received signal while a path threshold of 20dB has a better performance when we consider the actual received signal at low SNR and they have identical performance at moderate SNR. This is because the 20dB threshold is more sensitive to noise, which means that the noise will have a bigger impact on the CIR and the reconstructed signal which is not desirable. Since we only care about the desired received signal, a 15dB threshold is a better stopping criterion when the two paths are resolvable and the paths have relatively large gains. If the paths were weaker, a higher stopping threshold could be more useful. In general, we want the stopping threshold to be large enough to capture the majority of the signal power without capturing substantial noise.

The above simulation was repeated with only a change in the CIR. Now the CIR is simulated as a two tap model, with the separation between the two taps being 0.2 ns, which means that the paths are not resolvable. A sample of the CLEAN estimation of the CIR and the reconstructed signals at an SNR of 10dB is shown in Figure 4-5, Figure 4-6 and Figure 4-7 respectively.

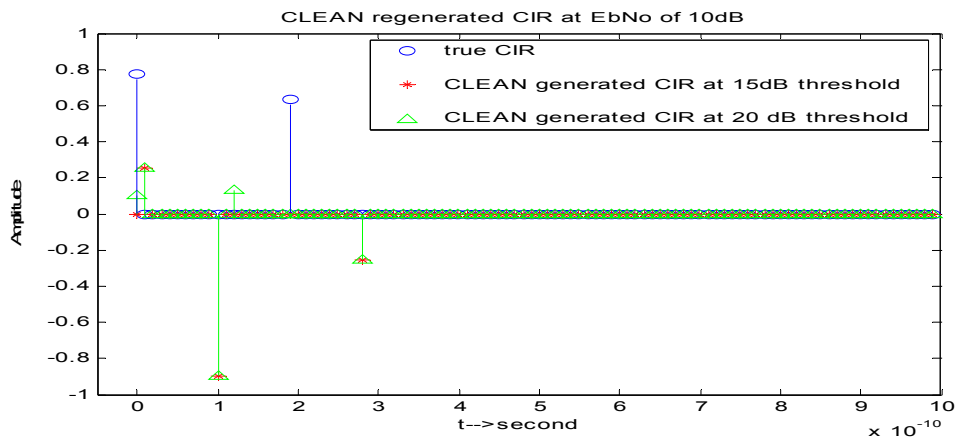


Figure 4-5 Sample of CLEAN estimate of CIR when paths are not resolvable

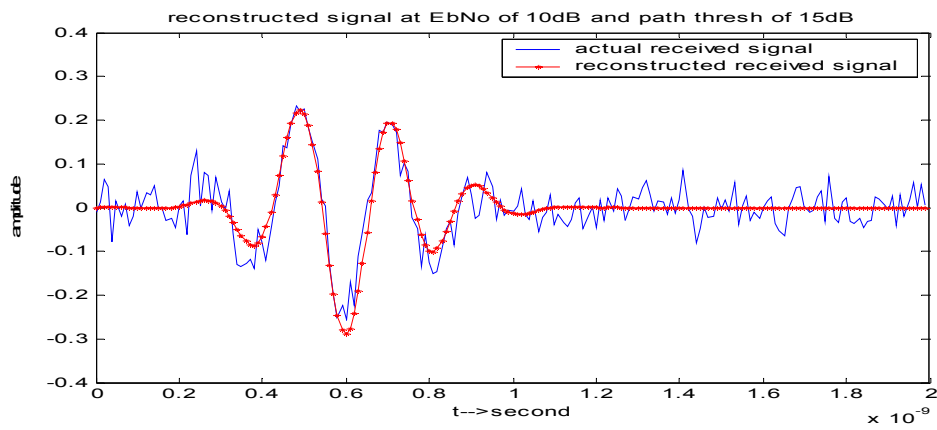


Figure 4-6 Sample comparison of reconstructed received signal and actual received signal when paths are not resolvable

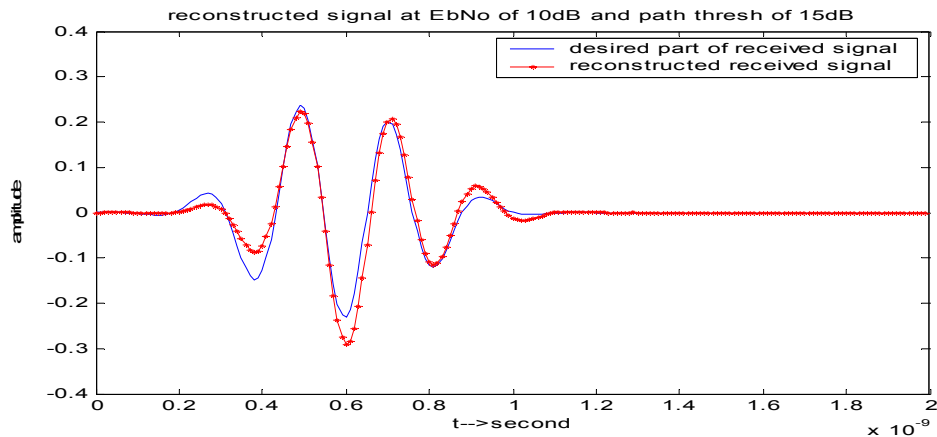


Figure 4-7 Sample comparison of reconstructed received signal and desired part of received signal when paths are not resolvable

When the paths are not resolvable and are very close to each other, CLEAN can't give a good estimate of the CIR. However, the reconstructed received signal still closely resembles the true signal. A comparison of the error between the estimated signal, actual received and the desired part of the received signal for different SNR values and path thresholds is shown in Table 4-4 and Table 4-5 respectively.

Table 4-4 CLEAN performance at different SNR when paths are not resolvable (received signal)

SNR (dB)	10	15	20	25	30
MSE of CIR (15dB/20dB threshold)	0.0196/ 0.0197	0.0195/ 0.0195	0.0195/ 0.0193	0.0195/ 0.0193	0.0195/ 0.0194
Relative Error (15dB/20dB threshold)	0.2245/ 0.1936	0.1332/ 0.0983	0.1001/ 0.0614	0.0889/ 0.0484	0.0852/ 0.0444
Correlation (15dB/20dB threshold)	0.8827/ 0.8983	0.9333/ 0.9500	0.9510/ 0.9692	0.9568/ 0.9758	0.9588/ 0.9779

Table 4-5 CLEAN performance at different SNR values when paths are not resolvable (desired signal)

SNR (dB)	10	15	20	25	30
MSE of CIR (15dB/20dB threshold)	0.0196/ 0.0198	0.0195/ 0.0195	0.0195/ 0.0193	0.0195/ 0.0193	0.0195/ 0.0194
Relative Error (15dB/20dB threshold)	0.0842/ 0.0509	0.0833/ 0.0470	0.0836/ 0.0444	0.0836/ 0.0429	0.0836/ 0.0427
Correlation (15dB/20dB threshold)	0.9601/ 0.9752	0.9600/ 0.9768	0.9597/ 0.9780	0.9596/ 0.9786	0.9597/ 0.9787

The MSE of CIR, Relative Error and Correlation are all much worse than the previous case when the paths are resolvable. A threshold of 20dB performs much better than 15dB in terms of Relative Error and Correlation while it has almost identical performance as the 15dB threshold in terms of the MSE of CIR, different from the resolvable paths case. Note that the MSE is dominated by the fact that the pulses aren't resolvable, rather than the noise. This can be seen by the fact that MSE is insensitive to SNR and by comparing it with the MSE at infinite SNR given in Table 4-1.

Pulses which arrive at the receiver via different paths may experience different distortion. Up until this point, we have assumed that each of the received pulses has the same shape, and that their shape is the same as the template. A more realistic situation is that each path is associated with a different pulse shape due to diffraction or some other distortion. To examine this case, we simulate the CIR as in the resolvable paths case. However the pulse associated with the second path is now different from the LOS pulse. Specifically, we assume that second pulse has passed through brick and thus experiences severe frequency domain distortion. (Please see Chapter 6 for a more detailed description of the material-dependent effects.) Both the LOS pulse and the distorted pulse are from

measurements. Further, we only use the LOS pulse as the template in CLEAN. A sample of the CLEAN estimation of the CIR and the reconstructed signals at an SNR of 10dB is shown in Figure 4-8, Figure 4-9 and Figure 4-10.

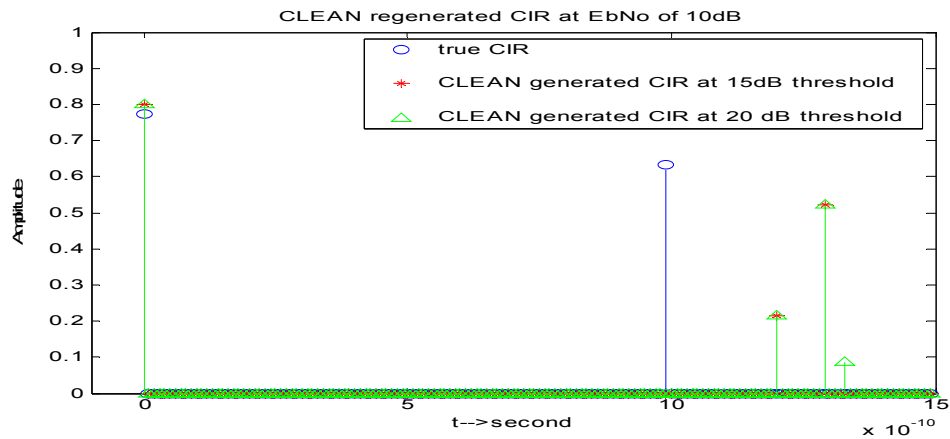


Figure 4-8 Sample of CLEAN estimate of CIR when pulse is distorted and paths are resolvable

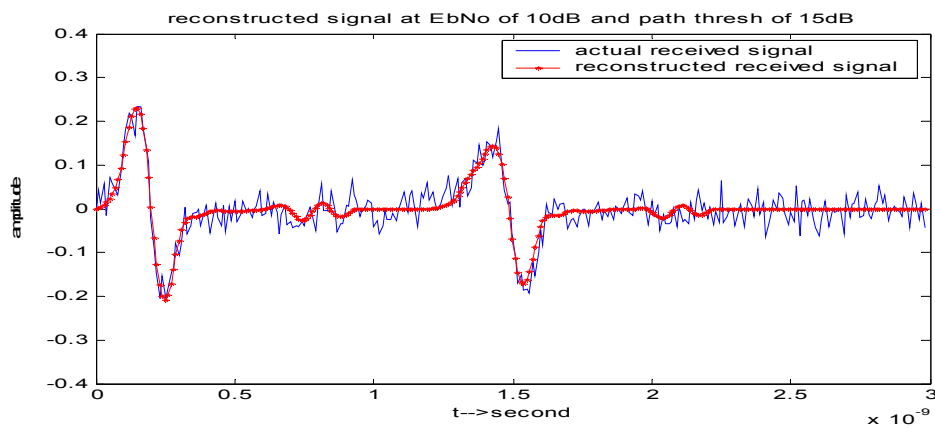


Figure 4-9 Sample comparison of reconstructed received signal and actual received signal when pulse is distorted and paths are resolvable

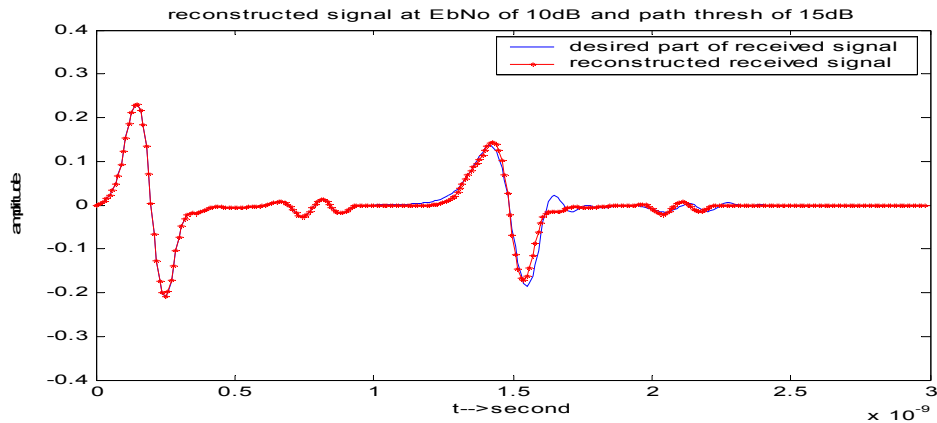


Figure 4-10 Sample comparison of reconstructed received signal and desired part of received signal when pulse is distorted and paths are resolvable

When different pulse shapes are associated with different paths and we use only the LOS pulse as a template, CLEAN can't give a good estimate of the CIR. It must use multiple taps to represent the distortion as will be discussed in more detail later in Chapter 6. However, we should note that the reconstructed received signal still resembles the true received signal.

A comparison of the error between the estimated signal, the actual received signal and the desired part of the received signal for different SNR values and path thresholds is shown in Table 4-6 and Table 4-7 respectively.

Table 4-6 CLEAN performance at different SNR when we consider the actual received signal if pulse is distorted and paths are resolvable

SNR (dB)	10	15	20	25	30
MSE of CIR (15dB/20dB threshold)	0.0052/ 0.0053	0.0052/ 0.0053	0.0052/ 0.0053	0.0052/ 0.0053	0.0052/ 0.0053
Relative Error (15dB/20dB threshold)	0.1825/ 0.1714	0.0791/ 0.0684	0.0399/ 0.0297	0.0268/ 0.0165	0.0227/ 0.0123
Correlation (15dB/20dB threshold)	0.9044/ 0.9103	0.9599/ 0.9653	0.9802/ 0.9851	0.9869/ 0.9917	0.9890/ 0.9938

Table 4-7 CLEAN performance at different SNR values when we consider the desired received signal if the pulse is distorted and paths are resolvable

SNR (dB)	10	15	20	25	30
MSE of CIR (15dB/20dB threshold)	0.0052/ 0.0053	0.0052/ 0.0053	0.0052/ 0.0053	0.0052/ 0.0053	0.0052/ 0.0053
Relative Error (15dB/20dB threshold)	0.0275/ 0.0164	0.0231/ 0.0121	0.0211/ 0.0108	0.0209/ 0.0105	0.0208/ 0.0104
Correlation (15dB/20dB threshold)	0.9867/ 0.9922	0.9888/ 0.9941	0.9898/ 0.9946	0.9899/ 0.9948	0.9899/ 0.9948

The CLEAN performance for different thresholds is similar to the case where there is no pulse distortion and the pulses are not resolvable. Since pulse distortion is likely in our measurements, a 20dB threshold will provide better performance than a 15dB threshold when we use CLEAN on our actual measurements. For completeness, we repeat the above simulation for the irresolvable paths case. Examples are shown in Figures 4-11 to 4-13 and the performance is summarized in Table 4-8 and Table 4-9.

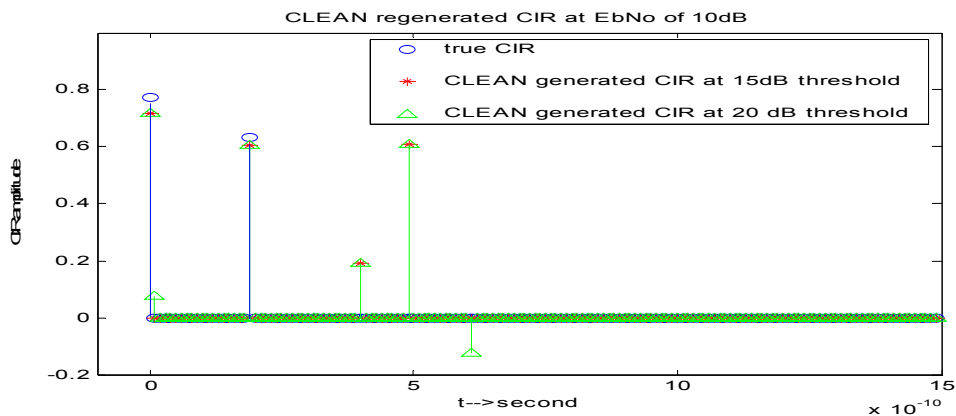


Figure 4-11 Sample of CLEAN estimate of CIR when pulse is distorted and paths are not resolvable

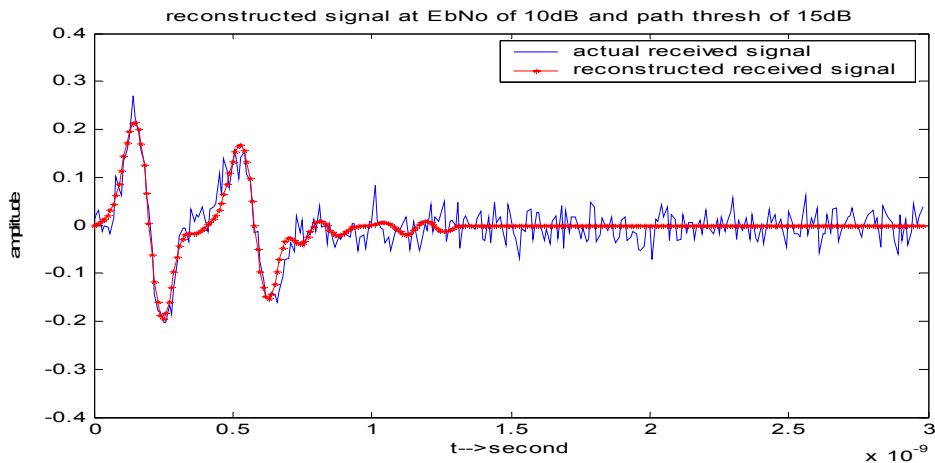


Figure 4-12 Sample of comparison of reconstructed received signal and actual received signal when pulse is distorted and paths are resolvable

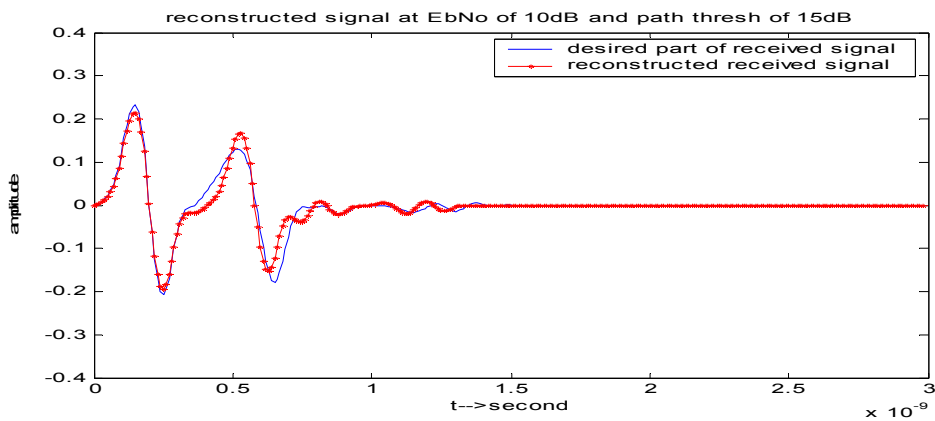


Figure 4-13 Sample of comparison of reconstructed received signal and desired part of received signal when pulse is distorted and paths are resolvable

Table 4-8 CLEAN performance at different SNR when we consider the actual received signal if pulse is distorted and paths are not resolvable

SNR (dB)	10	15	20	25	30
MSE of CIR (15dB/20dB threshold)	0.0052/ 0.0053	0.0052/ 0.0053	0.0052/ 0.0053	0.0052/ 0.0053	0.0052/ 0.0053
Relative Error (15dB/20dB threshold)	0.1893/ 0.1786	0.0826/ 0.0719	0.0416/ 0.0311	0.0282/ 0.0175	0.0239/ 0.0131
Correlation (15dB/20dB threshold)	0.9009/ 0.9064	0.9585/ 0.9635	0.9798/ 0.9845	0.9867/ 0.9914	0.9889/ 0.9936

Table 4-9 CLEAN performance at different SNR when we consider the desired received signal if pulse is distorted and paths are not resolvable

SNR (dB)	10	15	20	25	30
MSE of CIR (15dB/20dB threshold)	0.0052/ 0.0053	0.0052/ 0.0053	0.0052/ 0.0053	0.0052/ 0.0053	0.0052/ 0.0053
Relative Error (15dB/20dB threshold)	0.0280/ 0.0174	0.0237/ 0.0128	0.0223/ 0.0115	0.0219/ 0.0112	0.0219/ 0.0111
Correlation (15dB/20dB threshold)	0.9867/ 0.9917	0.9889/ 0.9938	0.9897/ 0.9944	0.9899/ 0.9946	0.9899/ 0.9946

The performance for different thresholds is consistent with the above resolvable paths case. Thus, we may conclude that a 20dB threshold will be a better stopping criterion for the CLEAN algorithm.

4.2 Other super-resolution techniques

There is no specific definition of super-resolution. For the deconvolution of the CIR from measurements, the traditional method is to use a matched filter to find the delay and corresponding amplitude of each multipath. The resolution of a matched filter is the duration of the transmitted signal autocorrelation function (within this resolution, it is indeed an optimal estimator in white Gaussian noise). Thus, any deconvolution algorithm that has better resolution than that of the matched filter is said to be capable of super-resolution. As seen from Table 4-1, the CLEAN algorithm is capable of sub-pulse-width resolution (the pulse width is smaller than the duration of the auto-correlation function of the pulse). We are interested in its advantage over other existing super-resolution algorithms in UWB system analysis.

As demonstrated in Chapter 3, the deconvolution techniques (inverse filtering and Van-Cittert technique) are super-resolution algorithms. The Maximum Likelihood Estimator

(MLE) is another super-resolution algorithm used to estimate both delay and amplitude in CIR deconvolution [36]. However, direct implementation of MLE is usually not practical because it is a non-linear least squares problem which involves a high order search (the order is equal to the number of paths). Another disadvantage of MLE is that it must know the number of path before calculation, which is itself a parameter that needs to be obtained from measurements. In white Gaussian noise, the Least Squares Estimator (LSE) is also the MLE [37]. A non-iterative LSE was proposed in [38] and was shown to be a better estimate of the CIR than the iterative method of Projection Onto Convex Sets (POCS) [39] [40], which is a super-resolution algorithm used to find a feasible solution that satisfies the various constraints on the CIR.

We will take a closer look at the non-iterative LSE and compare its performance with CLEAN in the following.

The received signal can written in a vector-matrix form as

$$\underline{y} = \underline{X}\underline{h} + \underline{n} \quad (4-1)$$

where the vectors \underline{y} , \underline{h} and \underline{n} are formed from the samples of $y(t)$, $h(t)$ and $n(t)$ in

Equation (3-1), respectively. The matrix \underline{X} is a circular matrix formed from the samples of the transmitted waveform $x(t)$.

As we know, the length of \underline{y} equals the sum of length \underline{x} and \underline{h} minus one. To make the Equation (4-1) feasible, both \underline{x} and \underline{h} are zero padded to be the same length as \underline{y} . Since the CIR vector \underline{h} has non-zero elements only on the indicator set E, consider a different model from Equation (4-1):

$$\underline{y} = \underline{X} \underline{\tilde{I}}_E \underline{h} + \underline{n} \quad (4-2)$$

where $\underline{\tilde{I}}_E$ is a diagonal matrix with entries equal to one if the index on the diagonal belong to the indicator set E and other entries equal to zero.

This is equivalent to forcing the elements of \underline{h} outside the indicator set to be zero.

Equation (4-2) can be rewritten as

$$\underline{y} = \underline{X}_E \underline{h}_E + \underline{n} \quad (4-3)$$

where $\underline{X}_E = \underline{X} \underline{I}_E$ and \underline{I}_E contains the non-zero columns of $\underline{\tilde{I}}_E$. The matrix \underline{X}_E contains only those columns of \underline{X} corresponding to the indicator set and \underline{h}_E is a vector of the same number of elements as in E.

The LS estimate can be computed as

$$\underline{h}_E = (\underline{X}_E^T \underline{X}_E)^{-1} \underline{X}_E^T \underline{y} \quad (4-4)$$

By exploiting the circular properties of matrix \underline{X} and the structure of \underline{X}_E , the calculations can be greatly simplified by the use of the Fast Fourier Transform (FFT) and Inverse Fast Fourier Transform (IFFT) operations. More detailed description of the calculation simplification can be found in [38].

The non-iterative LS deconvolution algorithm is first examined using synthetic data without noise. The probing signal is shown in Figure 4-1. The true channel impulse response and the received signal are shown in Figure 4-14 and Figure 4-15 respectively. As can be seen from the received signal, the first two paths are two closely spaced and it appears as one waveform at the receiver. The result of LS deconvolution is shown in Figure 4-16. Clearly, LS is perfect estimating the unresolvable multipaths in the absence of noise.

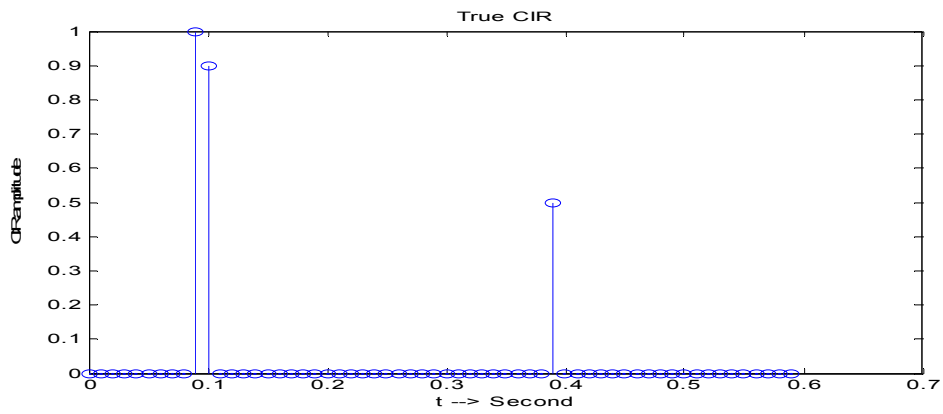


Figure 4-14 True Channel Impulse Response

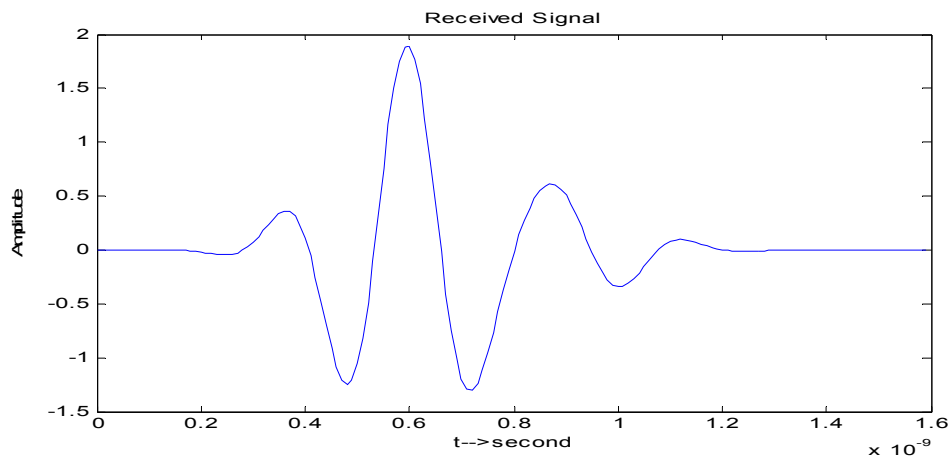


Figure 4-15 Received Signal

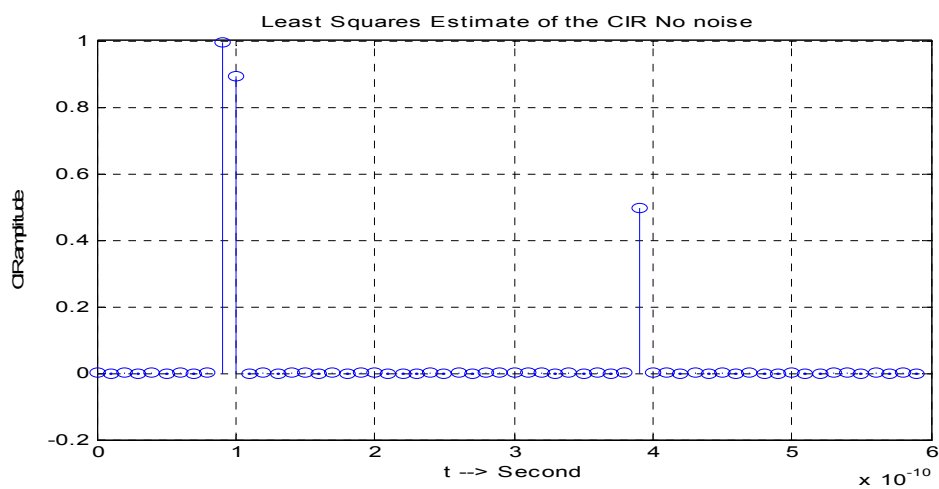


Figure 4-16 LS Estimate of the CIR Without Noise

However, to make the analysis more practical, we now add noise to the received signal. The SNR is 20dB. Figure 4-17 shows the LS estimate of the CIR with the white Gaussian noise.

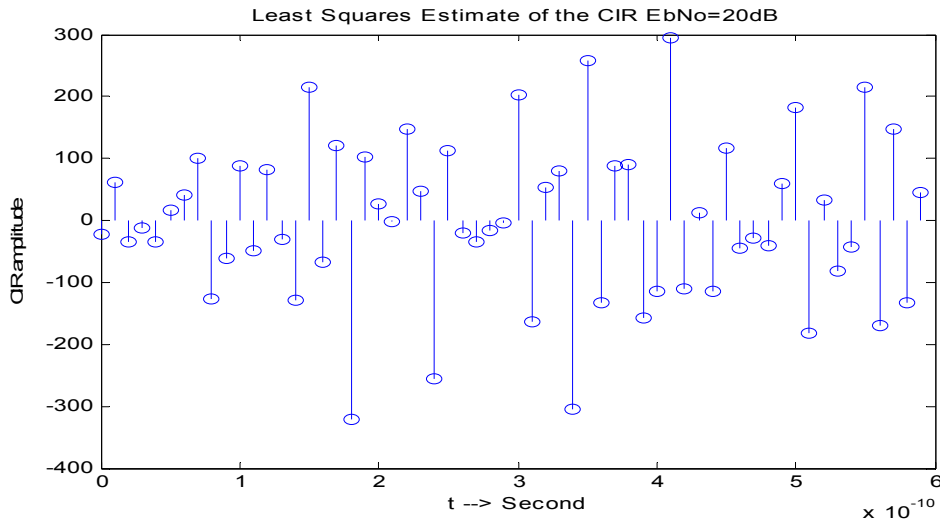


Figure 4-17 LS Estimate of the CIR with SNR=20dB

As seen from Figure 4-17, the LS algorithm completely collapses in the presence of noise. So even though the LS algorithm shows superior capability of super-resolution without noise, it is not applicable in real applications, while CLEAN has been shown to have a strong noise suppression capability.

5 Impact of Deconvolution on CLEAN Regenerated Channel Model

To get a better idea of how the CLEAN deconvolution algorithm performs in a much more realistic scenario, we use channel impulse responses generated from a realistic (i.e. derived from measurements) UWB channel model rather than the simple synthetic channel impulse responses. We evaluate the accuracy of the CLEAN algorithm by comparing the statistics of the regenerated channel and the original channel model.

5.1 Saleh-Valenzuela Model

The Saleh-Valenzuela (S-V) model was first developed for wideband channels [44]. The work in [16] found that UWB measurement data fit a modified version of the S-V model well. We will use the modified S-V model as our UWB channel model to test the CLEAN algorithm.

The S-V model is a tapped delay line model given by

$$h(t) = \sum_{l=0}^L \sum_{k=0}^K \beta_{k,l} \delta(t - T_l - \tau_{k,l}) \quad (5-1)$$

It is assumed that the multipath components arrive in clusters. The inner summation is over the rays in the l^{th} cluster while the outer summation is over the clusters. The cluster arrival rate follows a Poisson distribution and within each cluster the ray arrival rate also obeys a Poisson distribution. The average power of both the clusters and the rays within

the clusters are assumed to decay exponentially. The magnitudes of the path amplitudes are assumed to follow a lognormal distribution and the polarity of each path is random.

In brief, this model is characterized by 5 parameters:

- Λ is the mean cluster arrival rate
- λ is the mean ray arrival rate (within a cluster)
- Γ is the cluster exponential decay factor
- γ is the ray exponential decay factor
- σ is the standard deviation of the lognormal distributed path powers

A search was performed to find appropriate parameters that generate impulse responses with the same characteristics as the measured impulse responses. The characteristics that determined the fit of the simulated responses to the measured responses were mean excess delay, RMS delay spread, and number of multipath components above the -15 dB threshold. The parameters that we used in the following simulations were obtained using Bicone NLOS measurement data [13] and are given in Table 5-1.

Table 5-1 Saleh-Valenzuela Model parameters for Bicone NLOS

Parameter	$1/\Lambda$ (second)	$1/\lambda$ (second)	Γ	γ	σ
Value	5.2e-9	0.8e-9	12.0e-9	5.0e-9	5

5.2 Comparison of Channel Statistics

The statistics of the Saleh-Valenzuela model and the CLEAN regenerated channel using the measured Bicone NLOS channel parameters for different CLEAN thresholds are shown in Figure 5-1 to Figure 5-6 and Table 5-2. Specifically we examine the Cumulative Distribution Function (CDF) of the mean excess delay, Root Mean Square

(RMS) delay spread and the number of paths for the synthetic channel. It can be seen that the regenerated channel taps accurately reflect the delay statistics. However, the CLEAN output has significantly fewer multipath components than the original data when we use the 15dB threshold for CLEAN. However, the difference is reduced substantially when we use the 20dB threshold. This is because since there are multiple sets of taps that provide similar received signals, CLEAN will tend to use fewer taps to represent the same shape when many paths are spaced very close to each other. And as we observed in our previous simulations, CLEAN will generate more paths as we increase the threshold to minimize the error. A 20dB threshold is obviously a better choice here since it perfectly matches the delay statistics and generates only slightly fewer paths.

Further, it is reasonable to expect that the delay statistics will match better than the CIR statistics. When the multipath is not resolvable, CLEAN can't accurately represent the CIR, although it can accurately represent the reconstructed received signal. The mean excess delay and RMS delay spread are more critical to the reconstructed signal than the number of multipath. Ultimately, CLEAN is pretty accurate at regenerating the synthetic data in the sense that both models will produce very similar received signals.

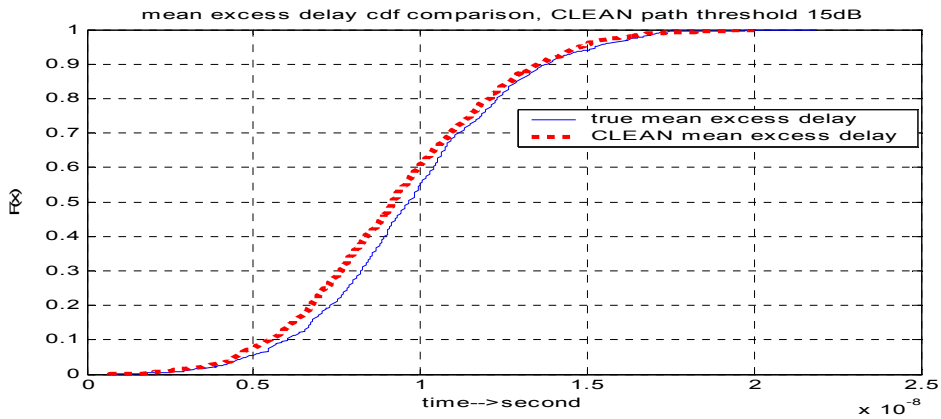


Figure 5-1 Mean Excess Delay CDF for Synthetic Channel and CLEAN Output with CLEAN path threshold 15dB

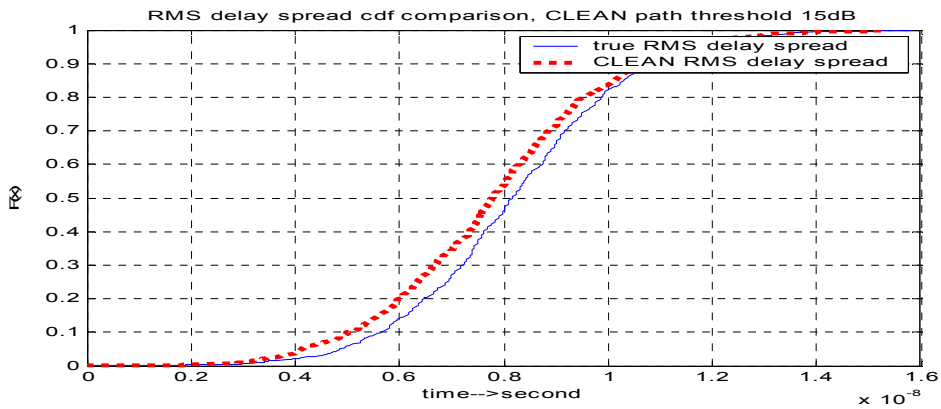


Figure 5-2 RMS delay spread CDF for Synthetic Channel and CLEAN Output with CLEAN path threshold 15dB

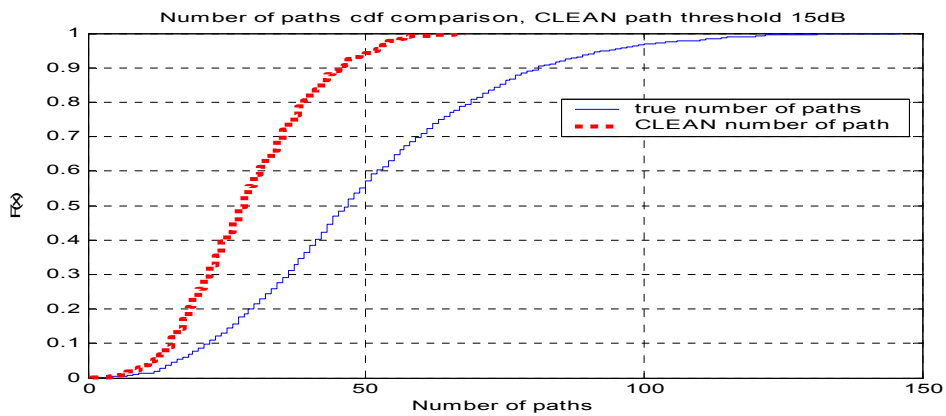


Figure 5-3 Number of Multipath CDF comparisons with CLEAN path threshold 15dB

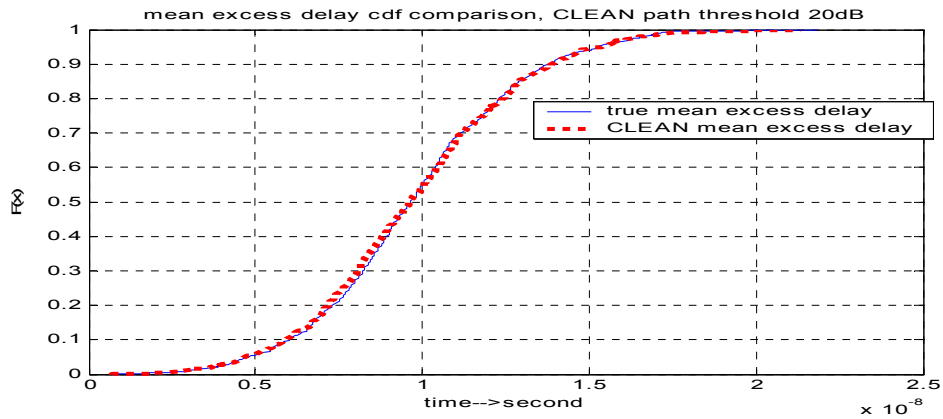


Figure 5-4 Mean Excess Delay CDF for Synthetic Channel and CLEAN Output with CLEAN path threshold 20dB

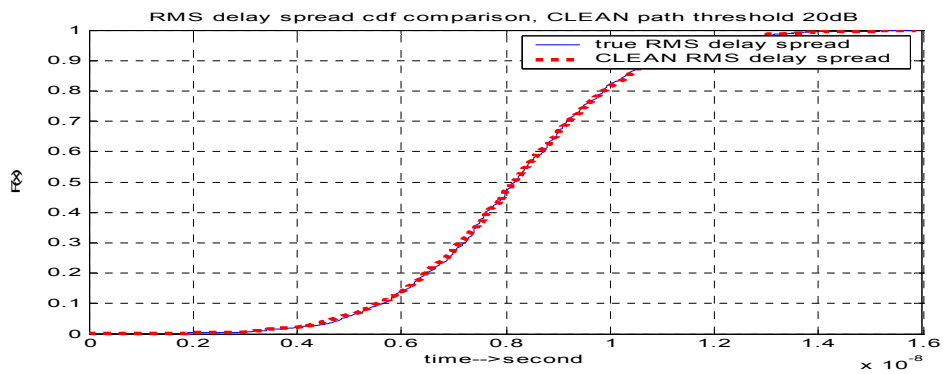


Figure 5-5 RMS delay spread CDF for Synthetic Channel and CLEAN Output with CLEAN path threshold 20dB

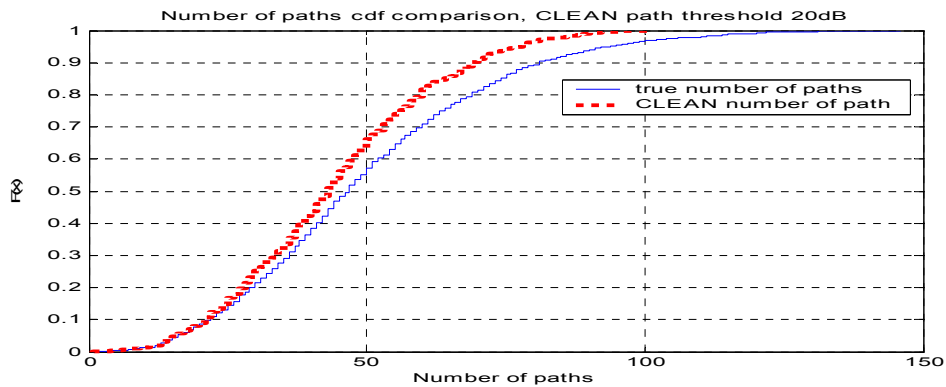


Figure 5-6 Number of Multipath CDF comparisons with CLEAN path threshold 20dB

Table 5-2 Bicone NLOS S_V model(path threshold for S_V=15dB CLEAN path threshold=15/20dB)

Statistics	S_V channel model	CLEAN regenerated channel model (15dBthreshold)	CLEAN regenerated channel model (20dBthreshold)
Mean Excess Delay (ns)	9.8054	9.3709	9.7762
RMS Delay Spread (ns)	8.2062	7.8323	8.2072
Number of Paths	49.7670	29.0360	44.2110
Relative Error between Received Signal and Reconstructed Signal	0.0860		0.0252
Correlation between Received Signal and Reconstructed Signal	0.9562		0.9875

We repeated the above simulation with the addition of Gaussian noise in the received signal. The SNR used here is defined as SNR per pulse. From Table 5-3 we can see that at very low SNR (10dB and 15dB) a 15dB path threshold is actually better because a bigger threshold results in noise spikes being mistaken as multipath components. For moderate SNR, the CLEAN algorithm performance is almost identical to the previous case without noise, as can be seen from Figure 5-7 to Figure 5-12 and Table 5-3, which means 20dB is a better threshold.

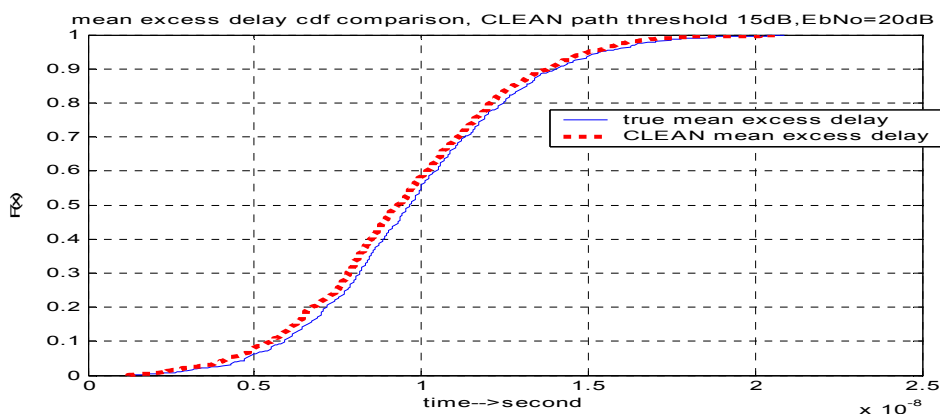


Figure 5-7 Mean Excess Delay CDF for Synthetic Channel and CLEAN Output with CLEAN path threshold 15dB at SNR=20dB

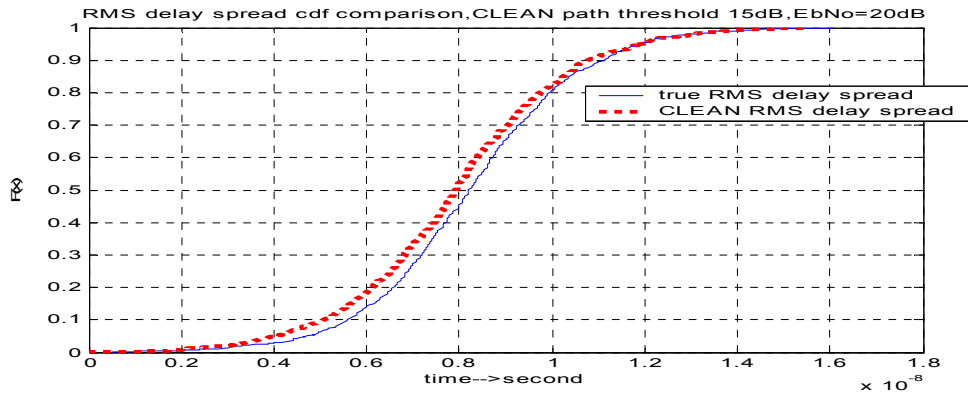


Figure 5-8 RMS delay spread CDF for Synthetic Channel and CLEAN Output with CLEAN path threshold 15dB at SNR=20dB

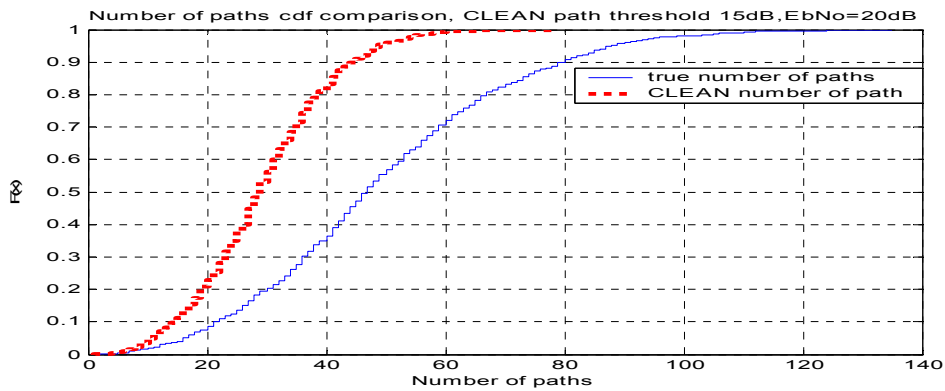


Figure 5-9 Number of Multipath CDF Comparisons with CLEAN path threshold 15dB at SNR=20dB

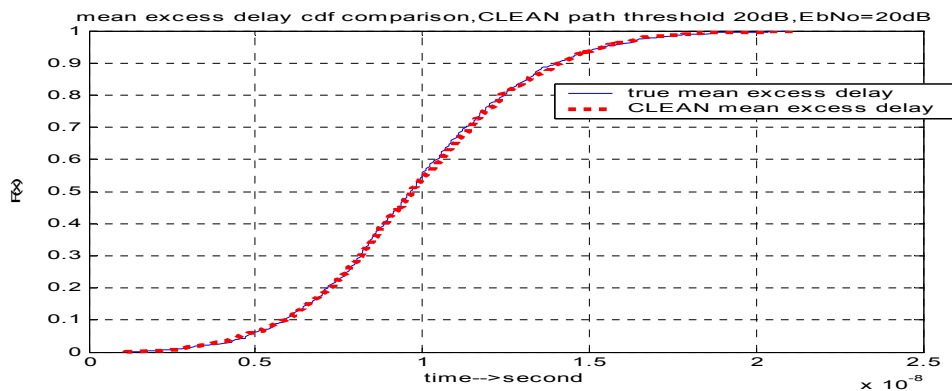


Figure 5-10 Mean Excess Delay CDF for Synthetic Channel and CLEAN Output with CLEAN path threshold 20dB at SNR=20dB

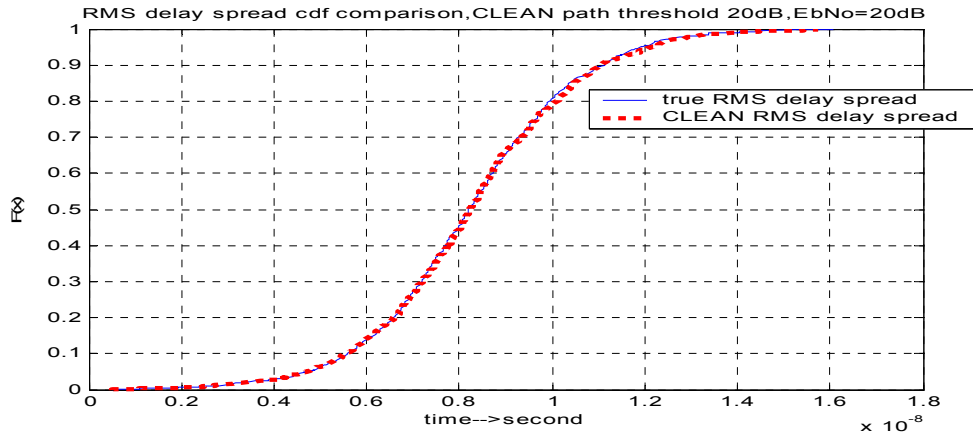


Figure 5-11 RMS delay spread CDF for Synthetic Channel and CLEAN Output with CLEAN path threshold 20dB at SNR=20dB

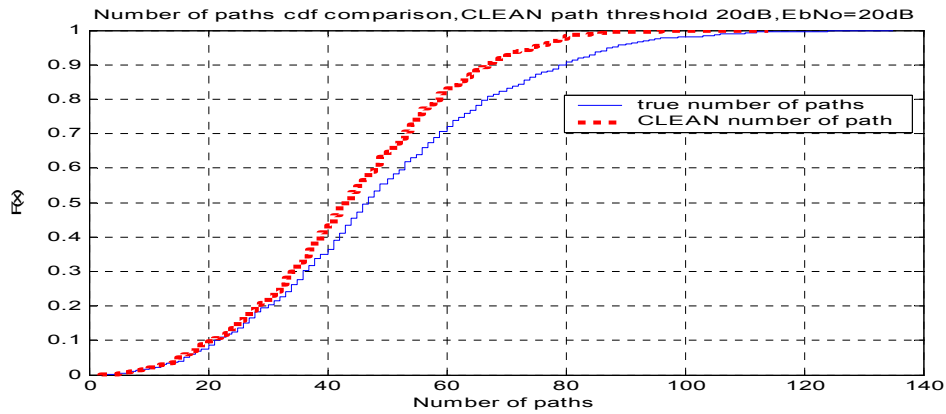


Figure 5-12 Number of Multipath CDF comparisons with CLEAN path threshold 20dB at SNR=20dB

Table 5-3 Bicone NLOS S_V model ; path threshold=15dB CLEAN path threshold=15/20dB at different SNRs

SNR (dB)	10	15	20	25	30
Mean Excess Delay (ns)	9.9047/	9.6719/	9.8321/	9.7606/	9.7953/
(S_V model/15dB/20dB CLEAN threshold)	10.671/ 16.130	9.6684/ 10.889	9.4837/ 9.8601	9.3671/ 9.7708	9.4024/ 9.8049
RMS Delay Spread (ns)	8.2119/	8.0622/	8.2504/	8.0892/	8.2093/
(S_V model/15dB/20dB CLEAN threshold)	10.153/ 19.884	8.1037/ 11.551	7.9389/ 8.2831	7.7422/ 8.1186	7.8151/ 8.1979
Number of Paths	50.1120/	47.9410/	49.1900/	50.2770/	49.8400/
(S_V model/15dB/20dB CLEAN threshold)	54.3040/ 379.1960	43.0720/ 163.497	29.3490/ 43.9150	29.4250/ 44.6720	29.3770/ 44.3410

Relative Error between reconstructed signal and actual received signal /desired received signal /15dB//20dB CLEAN threshold	0.6794/ 0.0590// 0.6258/ 0.1495	0.4183/ 0.0299// 0.3907/ 0.0352	0.2461/ 0.3002// 0.1983/ 0.0264	0.1488/ 0.1547// 0.0878/ 0.0260	0.1047/ 0.1070// 0.0459/ 0.0253
Correlation between reconstructed signal and actual received signal /desired received signal /15dB//20dB CLEAN threshold	0.5658/ 0.9707// 0.6116/ 0.9318	0.7626/ 0.9851// 0.7804/ 0.9826	0.8684/ 0.9570// 0.8955/ 0.9869	0.9250/ 0.9558// 0.9553/ 0.9871	0.9464/ 0.9566// 0.9769/ 0.9874

In wireless communications, the scatters are assumed to be independent which implies that there should be no correlation introduced in the channel. The temporal correlation between different multipath components in a received signal profile is of interest. In Figure 5-13, a comparison of the mean autocorrelation of received signal and CLEAN estimate of received signal of noise free case is plotted versus the excess delay. It is seen that the multipath components of the true channel are uncorrelated after an excess delay roughly equivalent to the pulse duration which is about 5 ns. The autocorrelation of the multipath components of the CLEAN generated channel overlaps with that of the true channel which demonstrates that no correlation is introduced by CLEAN regenerated channel model. Figure 5-14 plots the mean autocorrelation of received signal and CLEAN estimate of received signal when the SNR is 20 dB. The autocorrelation of the multipath components of the CLEAN generated channel doesn't overlap exactly with that of the true channel, but they still matches quite well. More importantly, there is no correlation between multipath components introduced by CLEAN regenerated channel model even in presence of noise. This is important for UWB receiver diversity design.

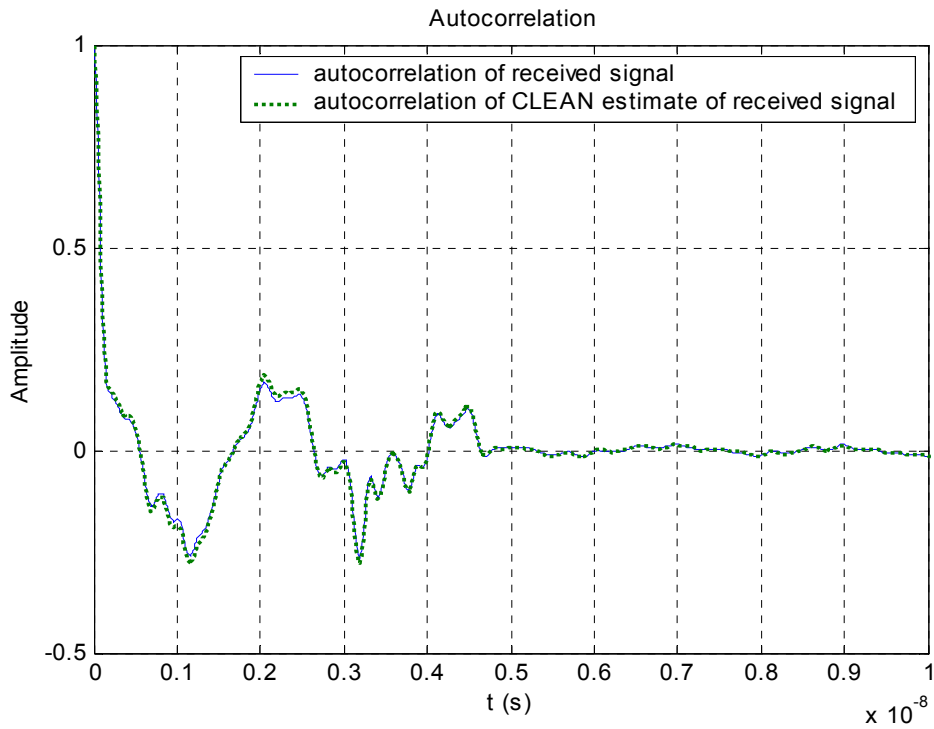


Figure 5-13 The mean correlation between multipath components at any 2 excess delays (noise free)

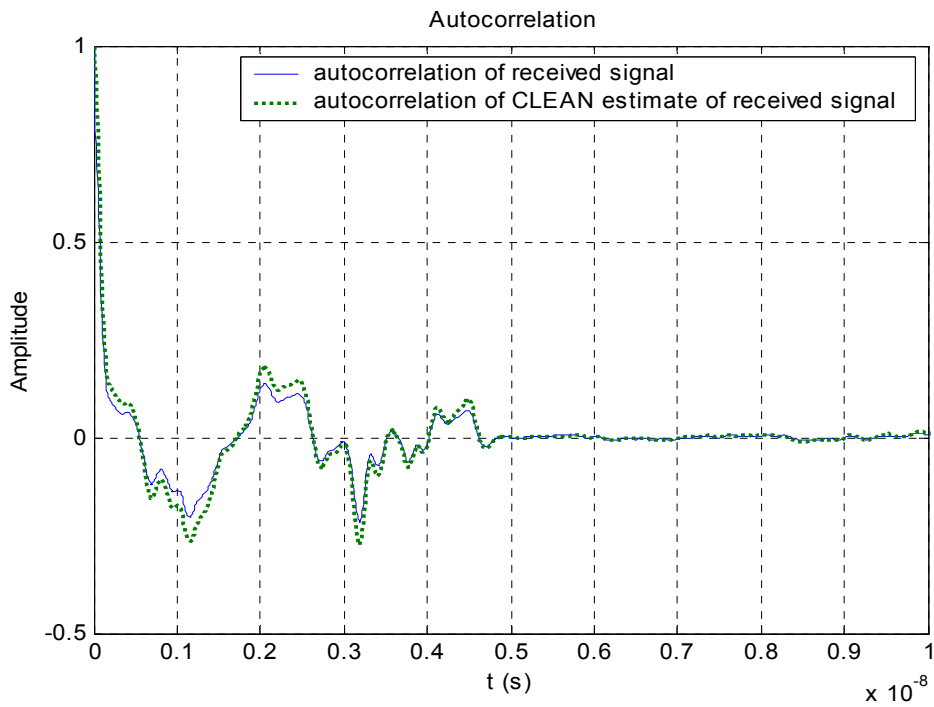


Figure 5-14 The mean correlation between multipath components at any 2 excess delays (SNR=20dB)

In conclusion, we can say that CLEAN is fairly accurate at representing the statistics of the underlying channel even if it doesn't accurately represent the actual channel taps and it will not introduce correlation into multipath components in the regenerated channel model. Since we are primarily interested in the effect that the channel has on the transmitted signal (i.e., the characteristics of the received signal) we conclude that CLEAN is sufficient for UWB channel modeling.

6 Impact of Discrete Assumption on UWB Channel Modeling

A fundamental assumption of the tap-delay line channel model given in Equation (1-2), is that the received signal is simply the sum of scaled and time shifted versions of the line-of-sight pulse. For moderate or even wide bandwidth signals, this assumption is reasonable. However, for UWB pulses with extremely large bandwidth, this assumption may no longer be valid. Instead, the received signal will be the sum of distorted and time-shifted pulses in general. Pulse distortion can occur due to the pulse passing through materials that are frequency dependent, from reflection, diffraction or from the antenna itself.

In this chapter, we will investigate the impact of using a discrete-tap channel model in the presence of per path distortion or other channel effects which violate the assumption that the received signal is simply a sum of scaled and time-shifted versions of the line-of sight signal. We will address two basic questions: (1) “what is the direct impact of our assumption on the resulting model?”, and (2) “How does this pulse distortion influence our interpretation of the model?”

6.1 Frequency distortion of materials

As presented in [13], typical material characterization shows that the insertion transfer function varies over the large frequency span of UWB signals, which means frequency

responses of typical materials are not constant over the entire signal spectrum. In other words, UWB signals with extremely large bandwidth may experience frequency distortion after passing through materials.

Figure 6-1 plots the received line-of-sight pulse using a TEM horn antenna with and without the material of brick present. The original pulse has pulse duration of roughly one nanosecond and a 10 dB bandwidth of approximately 6 GHz. As can be observed from Figure 6-1, the pulse is obviously distorted due to the frequency dependent nature of the material. The classic tap-delay line channel model cannot explicitly account for this distortion without modification. However, the model can incorporate the effect of distortion implicitly. Physically, there is a single path that exhibits frequency distortion. Thus, using a single path of the form given in Equation (1-2), we cannot represent the distorted pulse. Nevertheless, the model can accurately represent the pulse if we relax the restriction that we use a single path. As observed from Figure 6-2, which plots the impulse response determined by CLEAN, it uses two extra taps to account for the distortion exhibited along a single path. We shall refer to such extra paths as “phantom paths” since the model includes them to represent the per-path frequency distortion rather than independent temporal echoes. The modeled pulse using CLEAN generated taps (including phantom paths) very closely represents the true distorted pulse as seen from Figure 6-3. The accuracy can be seen from the mean square error (MSE) between the modeled pulse and the true distorted pulse which is on the order of 10^{-4} . Similar plots for wallboard, cloth partition, a wooden door, concrete blocks, Styrofoam, glass and plywood

are given in Appendix A. The MSEs for these materials are even smaller than the MSE of brick as summarized in Table 6-1.

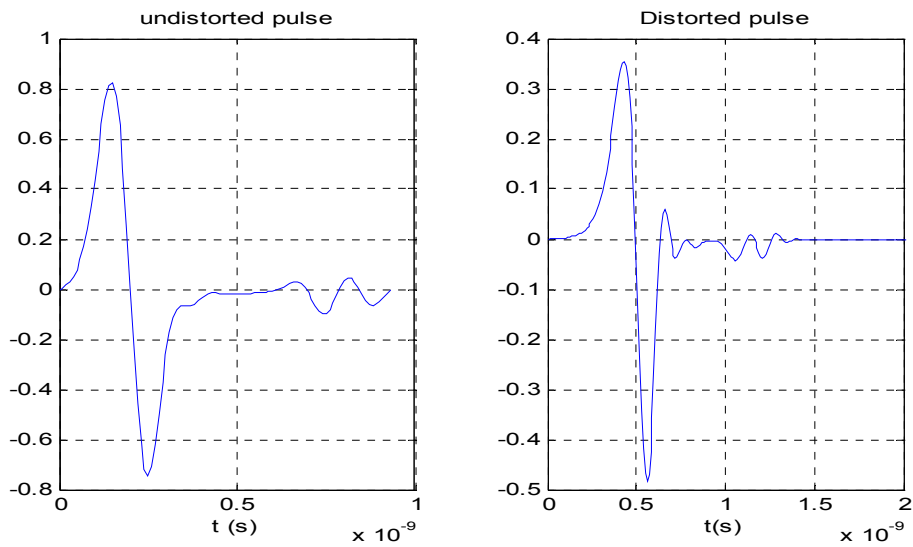


Figure 6-1 Original and distorted UWB pulse after passing through Brick

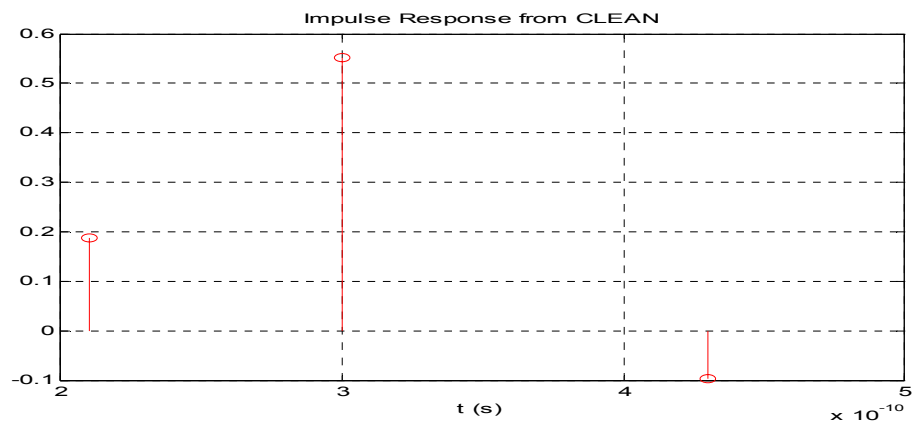


Figure 6-2 Discrete Tap Channel Model Created by CLEAN Algorithm using the Distorted Pulse After Passing Through Brick (CLEAN threshold of 20 dB)

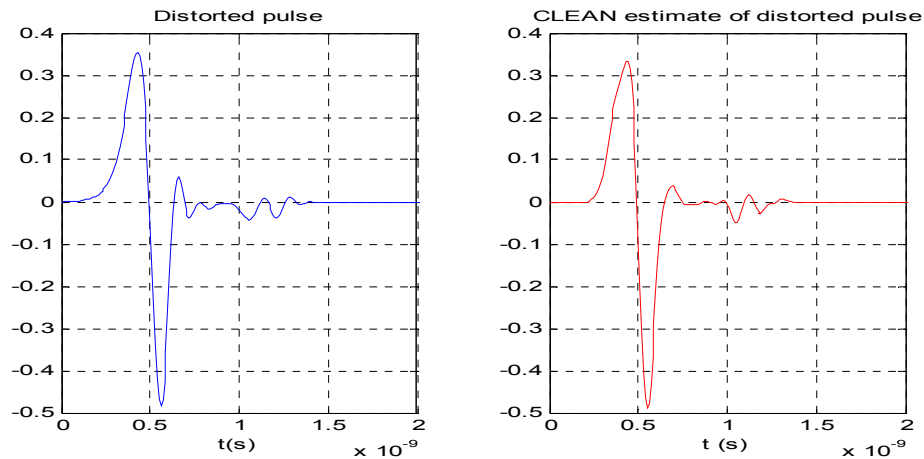


Figure 6-3 Distorted UWB Pulse After Passing through Brick and Pulse Produced from CLEAN

Another thing worthy of notice is that after the UWB pulse passes through materials, the resulting energy loss varies substantially for different kinds of materials as summarized in Table 6-1. For example, the energy loss in the distorted pulse after passing through concrete blocks is as large as 13.62 dB while there is almost no energy loss for foam. Table 6-1 also presents the percent energy measure which describes the relative strength of the phantom paths. A large percent energy measure signifies that the phantom paths are weak relative to the main path which represents the actual temporal echo. When we run CLEAN on the distorted pulse resulting from concrete blocks, we will need two extra taps to represent the frequency distortion. However, the received signal is a sum of distorted pulses via different paths; when we run CLEAN on the summed signal, these extra taps may be too far below the CLEAN threshold to be detected due to the large attenuation associated with those materials.

Standard wireless channel models assumes uncorrelated scattering. However, as we see from Figure 6-2, CLEAN has created multipaths to represent one temporal echo, which implies that these paths are now correlated because they are really representing one true path. Figure 6-4 plots the autocorrelation of the template (line-of-sight) pulse, distorted received pulse and CLEAN estimate of distorted pulse. However, the multipath components are uncorrelated after an excess delay roughly equivalent to the template pulse duration which is about 0.9 ns for all three cases. So no correlation is introduced to the multipath components in the CLEAN regenerated channel model. This is not surprising when we notice that the phantom paths are within about 0.1 ns of the true path, which is a lot smaller than the pulse duration and the relatively low strength of the phantom paths.

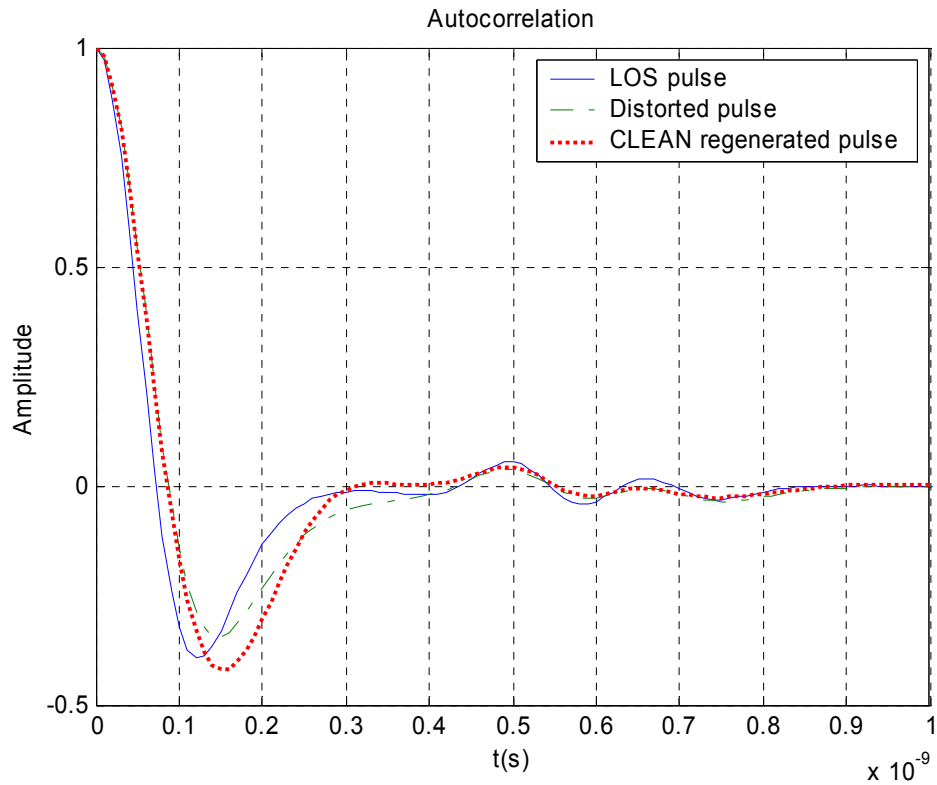


Figure 6-4 Auto-correlation comparison between template pulse, distort pulse and CLEAN estimate of distorted pulse

In conclusion, the discrete tap-delay line channel model can be used to represent path specific frequency distortion; however, the model must include phantom paths in order to accommodate the distortion. Care must be taken when using such a model when pulse distortion is expected, since we must interpret the model output correctly. The phantom paths will not cause much trouble at our CLEAN output of realistic measurements since the large attenuation of some materials eliminates a majority of the phantom paths in a line-of-sight environment. However, in the case of non-line-of-sight, we need to be more cautious interpreting the CLEAN output.

Table 6-1 Discrete Channel Representation of UWB Pulse (TEM LOS Pulse) After Passing through Common Building Materials with CLEAN threshold of 20dB

Material	Energy in Dominant CIR Component	Components in CIR	Energy Loss in Distorted Pulse (dB)	MSE between distorted pulse and CLEAN regenerated pulse
Brick	87.2%	3	4.44	1.5053e-004
Wallboard	100%	1	0.44	2.1057e-005
Cloth Partition	98.0%	2	1.48	4.5064e-005
Wooden Door	98.7%	2	1.42	1.4352e-005
Glass	100%	1	0.90	6.8488e-005
Concrete Block	90.1%	3	13.62	3.1605e-005
Foam	100%	1	0.03	2.3279e-005
Plywood	100%	1	1.54	1.2924e-005
Structure Wood	100%	1	1.27	2.9494e-005

6.2 Distortion due to reflection

To examine the impact of reflections, measurements were taken in an anechoic chamber to characterize the UWB pulse distortion caused by reflections from common shapes. This phenomenon was captured in a series of measurements take by the Virginia Tech Antenna Group (VTAG) [13]. The “free-space reference”, “non-reflected” and “reflected” signals are measured for the different materials as shown in Figure 6-5. The “free-space reference” signal was used as the template and the “non-reflected” pulse was removed from the received signal before running the CLEAN algorithm.

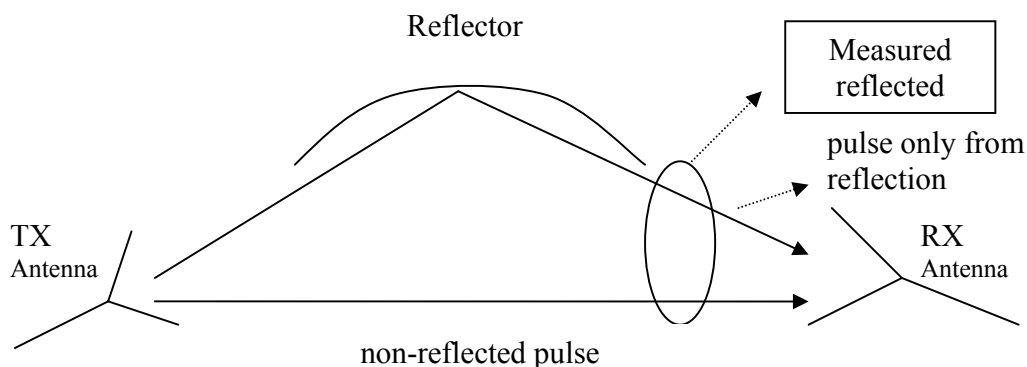


Figure 6-5 Measurement Diagram

As an example, consider a UWB pulse reflected by a hemisphere. The transmit and receive antennas were both pointed at the hemisphere to ensure the hemisphere was at the boresight of both antennas. Additionally, the non-reflected (i.e. direct) path was removed by taking a measurement without the hemisphere present. The received “free-space reference” pulse and the received reflected pulse (excluding the direct path) are plotted in Figure 6-6. Both signals are normalized for easy comparison. The reflection causes two effects. First, it inverts the pulse as expected. Second, it also rings at the resonant frequency of the sphere. As a result, the received pulse is followed by a slow oscillation. While the true CIR is a single path, CLEAN will attempt to model the ringing effect by introducing several phantom paths as shown in Figure 6-8. It essentially builds an FIR filter to approximate the frequency distortion of the pulse due to reflection. As a result, the CLEAN algorithm is accurate at regenerating the distorted pulse, although it will again create several phantom paths. A comparison of the reflected pulse and CLEAN estimate is plotted in Figure 6-7. The MSE between the reflected pulse and CLEAN estimate is only $3.1251e-005$. Similar plots for pulses reflected from a cube at 0 degree, a

cube at 45 degrees and a cylinder are given in Appendix B. Discrete channel representations of the UWB pulse after being reflected from common shapes are summarized in Table 6-2. While the additional paths are well below the specular path (more than 15 dB for the hemisphere), clearly the impulse response needs to include a large number of additional phantom paths in order to accurately represent the reflected signal. Those additional phantom paths may be suppressed when the total received signal has a line-of-sight signal or other less attenuated replicas present due to the energy loss and relatively low energy in the phantom paths caused by reflection. However, in a NLOS environment, we need to interpret the CLEAN output carefully to avoid mistaking those phantom paths as real paths.

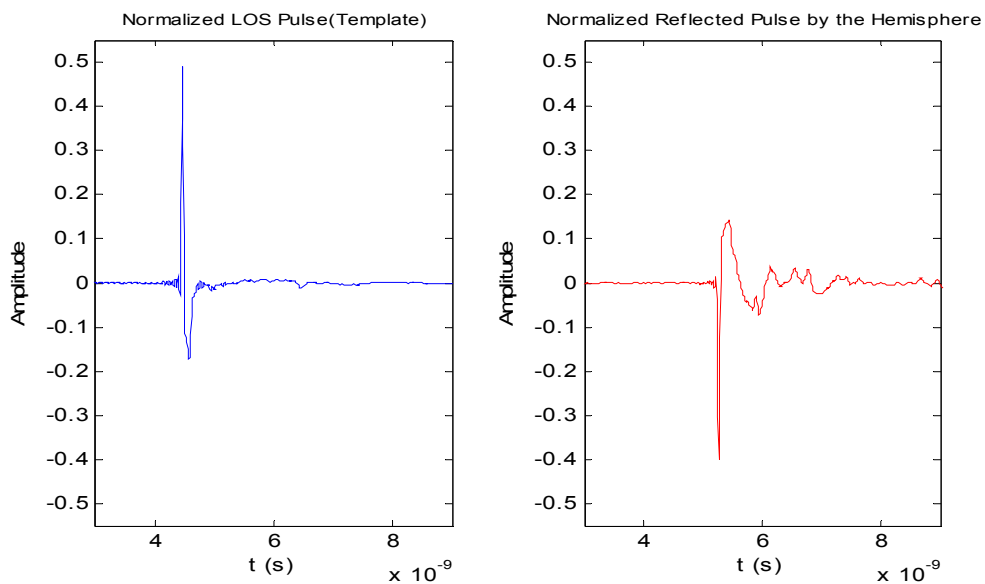


Figure 6-6 Line-of-sight signal (left) and signal reflected from a hemisphere of 6 inch diameter

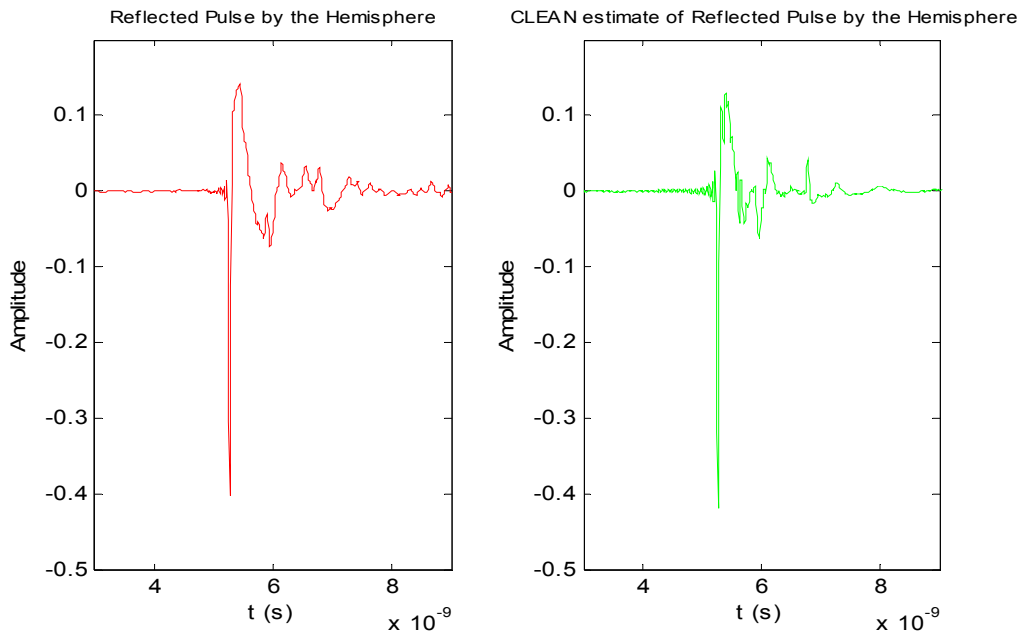


Figure 6-7 Reflected pulse by a hemisphere and CLEAN estimate of the reflected pulse

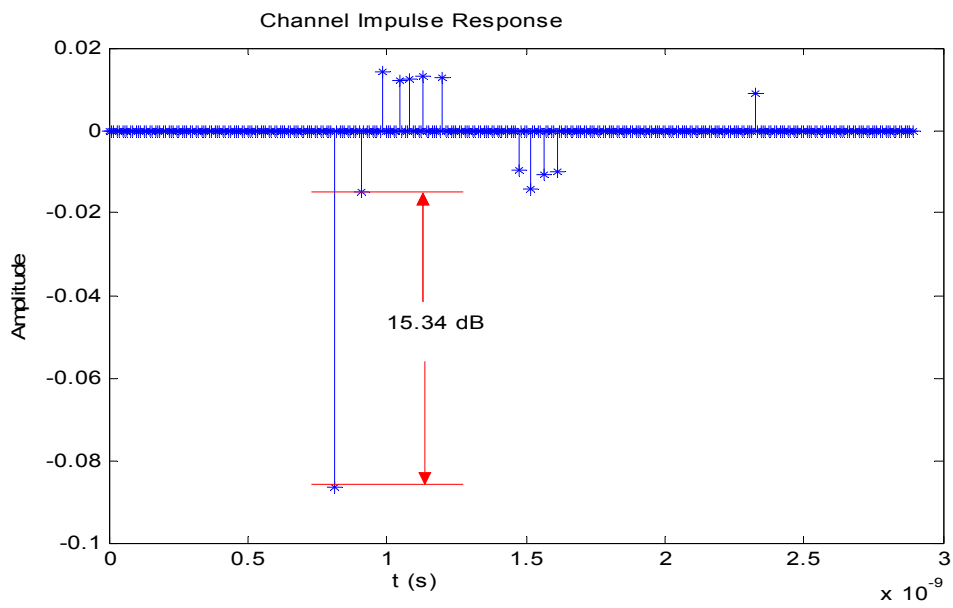


Figure 6-8 CLEAN generated Impulse Response for signal reflected by a Hemisphere of 6 inch diameter with CLEAN threshold of 20 dB

Table 6-2 Discrete Channel Representation of UWB Pulse (TEM LOS Pulse) After Reflected by Common shapes with CLEAN threshold of 20dB

Material	Energy in Dominant CIR Component	Correlation between the Reflected Pulse and Template	Components in CIR
Hemisphere	81.90%	85.23%	12
Cylinder	91.43%	84.35%	6
Cube at 0 degree	65.13%	67.85%	18
Cube at 45 degree	85.41%	80.27%	7

Again, we need to check if correlation is introduced into multipath components as a result of CLEAN generated phantom paths. Figure 6-9 plots the autocorrelation of the template (line-of-sight) pulse, the distorted received pulse and CLEAN estimate of distorted pulse. While the multipath components of the true channel are uncorrelated after an excess delay roughly equal to the duration of the template (line-of-sight) pulse which is about 0.5 ns, the multipath components of the CLEAN regenerated channel are uncorrelated after an excess delay about 1 ns. The phantom paths have introduced small correlation to the multipath components in CLEAN regenerated channel model. This may potentially have an adverse effect on the use of time diversity in UWB receiver design.

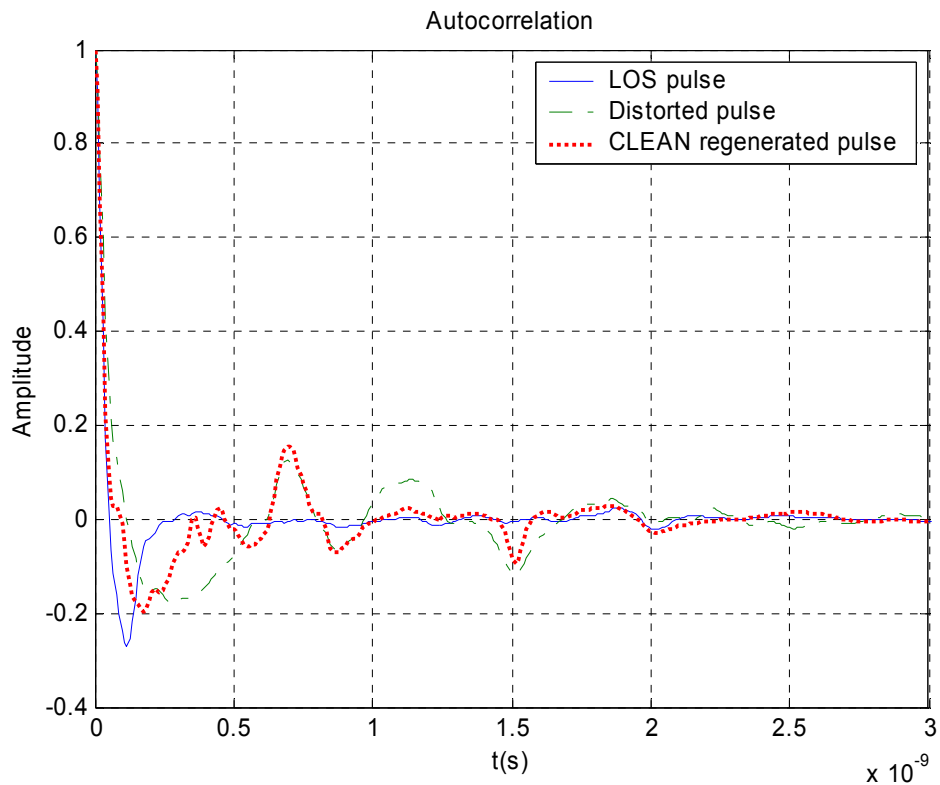


Figure 6-9 Auto-correlation comparison between template pulse, distort pulse and CLEAN estimate of distorted pulse

The classical model can easily represent the specular component, but does not assume the existence of the resonant components. Similar to the above discussion for UWB pulses passing through common building materials, care must be taken when reflections are expected to explain the model output correctly. These phantom paths are not likely to appear in many LOS measurements while may be present in NLOS measurements. Furthermore, we need to be aware that the existence of phantom paths may violate the uncorrelated scatters of standard channel model. Correlation is introduced into the multipath components of the CLEAN regenerated channel model.

6.3 Antenna induced distortion

Another potential source of pulse distortion in UWB systems comes from the antenna itself. The impulse response of the antenna may change with both elevation and azimuth angle. Clearly the change is more pronounced for directional antennas such as the TEM Horn antenna than omni-directional antennas such as the bicone antenna. Nevertheless, even omni-directional antennas suffer from pulse distortion. Specifically, the pulse shape transmitted or received at various elevation angles will be different (distorted) from that observed at boresight. This can be seen in Figure 6-10 which plots the received pulse using bicone antennas measured at different elevation angles. Figure 6-11 plots a closer comparison of the received pulse at zero degrees and sixty degrees respectively. Note that as expected, the amplitude of the received pulse amplitude is reduced at higher elevation angles due to less antenna gain at those angles. The pulse is also distorted as compared to the pulse transmitted (or received) at zero degree elevation. If we assume that the zero degree elevation angle pulse is the nominal pulse shape (template for CLEAN), the pulse at sixty degrees can be represented using the discrete channel impulse response shown in Figure 6-12. Thus, if a pulse is received at an elevation angle rather than boresight, the discrete channel model will account for the resulting pulse distortion by again using additional paths as demonstrated in Table 6-3. As seen from Table 6-3, the received pulse at other elevation angles suffer from energy loss (more than 10 dB for 90 degrees elevation angle) and low cross-correlation (virtually zero cross-correlation for 90 degrees elevation angle) between the nominal pulse shape (received at boresight) and from other elevation angles would suggest that using a single pulse shape for the matched filter receiver is far from optimal. If we are not able to match individual elevation angles of

arriving pulses, the channel model will use phantom paths to represent this mismatch. For elevation angles near 90 degrees, the received signal is negligible due to the large energy loss and virtually zero cross-correlation. However, for pulses arriving from small elevation angles, they may cause a small number of phantom paths, which clearly biases the number of paths at the output of CLEAN.

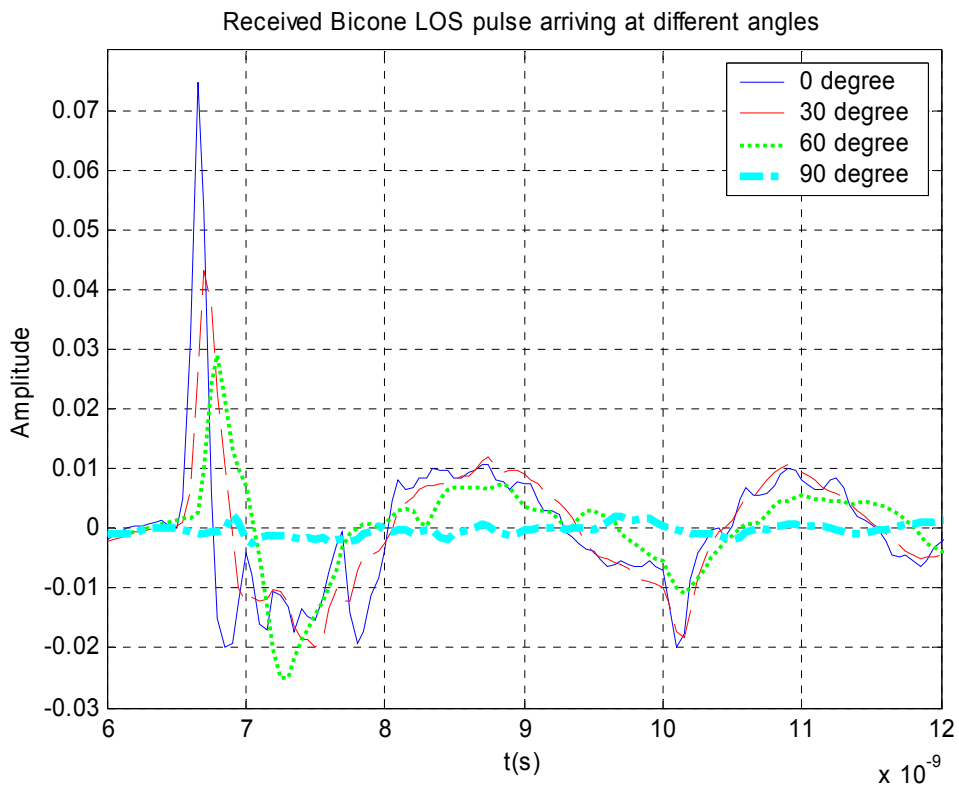


Figure 6-10 Received Pulse from various elevation angles using Biconical Antennas

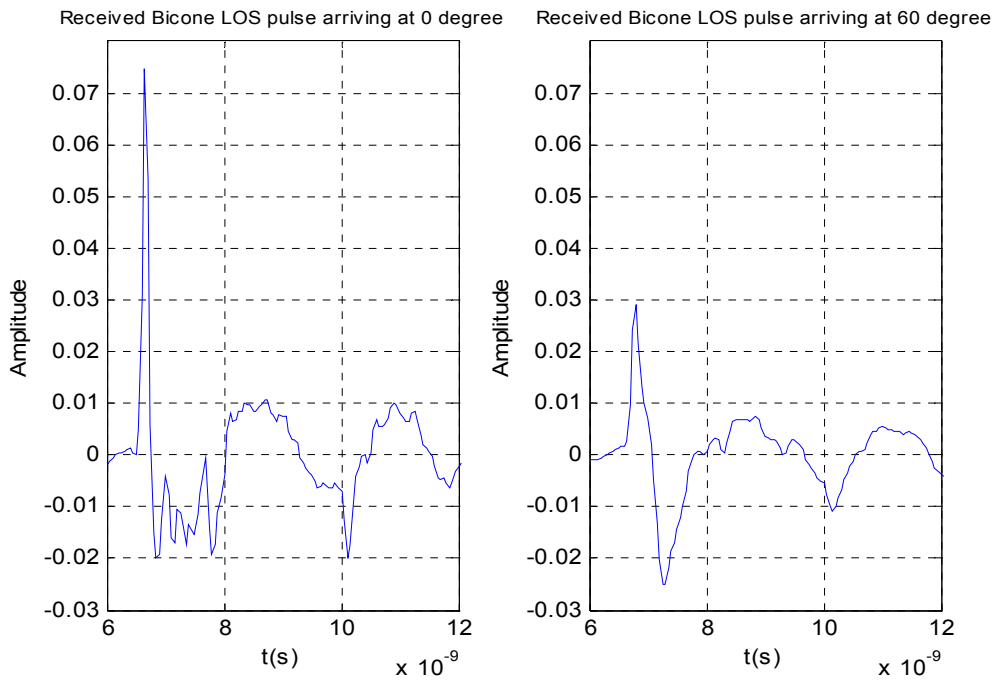


Figure 6-11 Received pulse from elevation angles of zero degree (left) and 60 degrees (right) using Biconical antennas

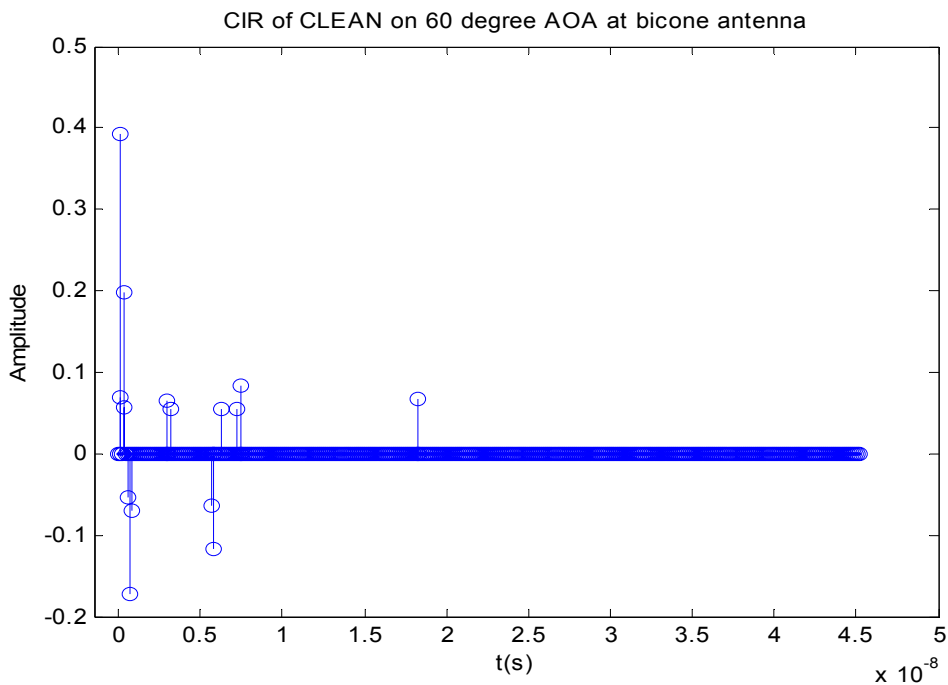


Figure 6-12 Discrete time Impulse Response for received pulse at elevation angle of 60 degree using pulse received at boresight (0 degree elevation) as template and CLEAN threshold of 20dB

Table 6-3 Discrete Channel Representation of UWB Pulse (using Bicone antenna) Received at Various Elevation Angles with 20dB CLEAN threshold

Elevation Angle (degrees)	Energy in Dominant CIR Component	Components in IR	Energy Loss in Distorted Pulse (dB)	Cross-Correlation between pulses received at 0 and different elevation angles
30	83.23%	4	1.45	73.74%
60	54.59%	15	3.33	36.51%
90	7.46%	130	10.67	0.10%

6.4 Diffraction induced distortion

Finally, an additional cause of frequency distortion is diffraction. Diffraction on a single path can be modeled in the frequency domain as [41, 42]

$$H(\omega) = \beta e^{j\varphi} \omega^\alpha e^{-j\omega\tau} \quad (6-1)$$

where α depends on the diffraction being modeled. For example, when the pulse experiences single edge diffraction, it can be shown that $\alpha = -0.5$ [41] [42]. Consider the received line-of-sight pulse shown in Figure 6-13 (left) and the received pulse after single edge diffraction given in Equation (6-1) (right). Again, the frequency dependent distortion can not be explicitly accounted for in the discrete time tap-delay line model. Using the CLEAN algorithm, we can create a discrete time impulse response to represent the distorted pulse as shown in Figure 6-14.

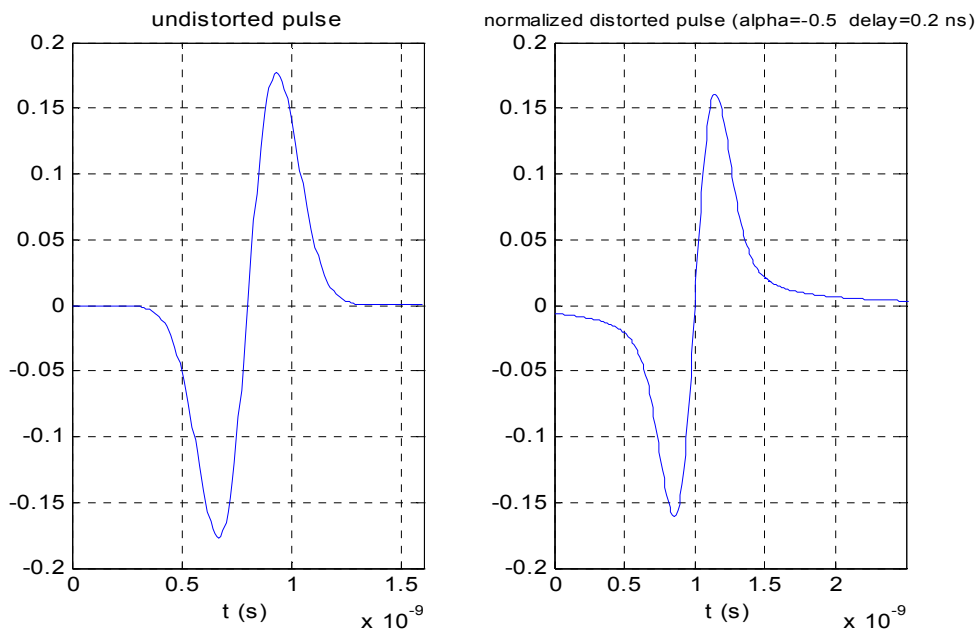


Figure 6-13 Received pulse with and without single edge diffraction using values given in [41] [42]

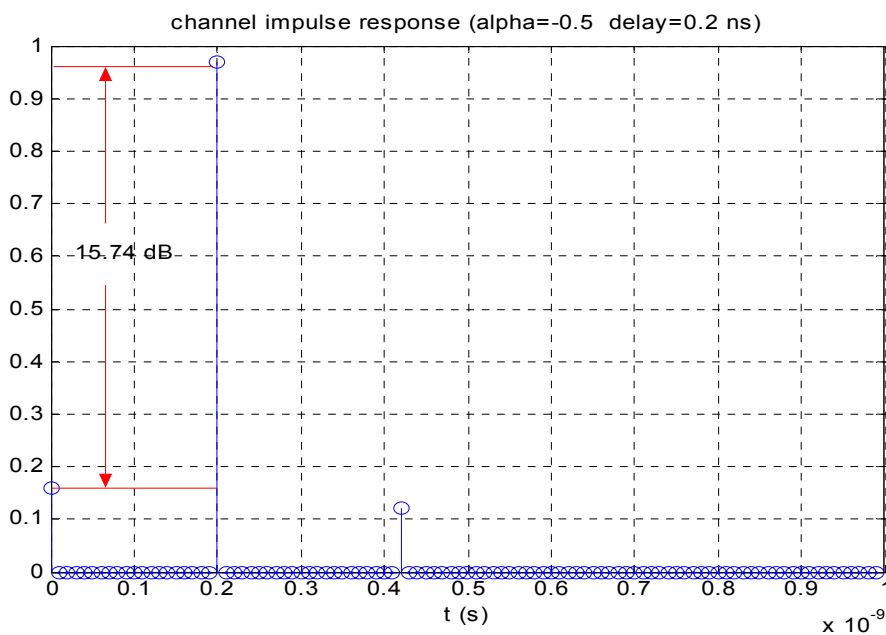


Figure 6-14 Discrete time Impulse Response due to a single edge diffraction along a single path with CLEAN threshold of 20dB

In conclusion it is clear that single path frequency distortion can arise from several different mechanisms when UWB signals are employed. This frequency distortion is not

explicitly represented by the discrete time tap delay line channel model that is commonly assumed. However, as we have shown, the model can implicitly represent this distortion by the inclusions of "phantom paths". Care must be taken when interpreting the model since each path in the model does not necessarily represent a separate independent time path. Antenna-induced distortion may be a more critical issue at the CLEAN output while the phantom paths induced by other frequency distortion mechanisms can be eliminated by choosing appropriate CLEAN threshold due to their large energy loss. For UWB systems we must understand that the channel model is more of a "black box" than in wideband systems where we can generally view each path in the model as a physical transmission path. This places more burdens on the researcher to understand what characteristics of the channel are most important to the issue under study. If the receiver is impacted only by the delay spread, temporal correlation, or other statistics of the received signal, the discrete time model is sufficiently accurate. However, if the model is being used as a guide for the number of necessary Rake fingers or physical interpretations of the model, care must be taken when interpreting the model output.

7 Conclusions and Future Work

This thesis has discussed a range of topics related to ultra-wideband channel modeling. Significant work on choosing and evaluating an appropriate deconvolution technique to extract the channel impulse response from measurement data was presented. Based on the work, issues in the applicability of the tap-delay line model were studied from channel impulse responses extracted by the CLEAN algorithm.

Three different methods of deconvolution were discussed in Chapter 3. The widely used frequency domain techniques: improved inverse filtering and Van-Cittert deconvolution with Bennis-Riad optimization criteria were explained and their performances were evaluated. A time domain technique known as the CLEAN algorithm was presented that has the advantage of an inherent ability to produce a discrete CIR in time, which takes the form of the tap-delay line channel model. A comprehensive study of CLEAN performance was carried out in Chapter 4. Different thresholds for CLEAN were also examined and we came to the conclusion that a 20 dB threshold is better than a 15 dB threshold as a stopping criteria for the CLEAN algorithm.

Chapter 5 studied the impact of deconvolution on the CLEAN regenerated channel model. We used a simulated Saleh-Valenzuela channel model to compare the statistics of the “true” channel and CLEAN estimate of the channel. It was demonstrated that CLEAN is fairly accurate when representing the statistics of the true channel, even if it may not accurately represent the actual channel taps when they are not resolvable. Since we were

primarily interested in the impact that the channel has on the transmitted signal, we concluded that CLEAN is sufficient for our purposes.

Chapter 6 explored potentials in UWB communications that may violate our traditional tap-delay line model assumptions. Per-path distortion may occur when a pulse passes through a material, after reflection and diffraction. Even the elevation angle of the receiving antenna (or the transmit antenna) also introduces pulse distortion. The tap-delay line model cannot account for the pulse distortion implicitly. However, it is able to represent the distortion explicitly by introducing “phantom paths” in the channel model. We need to interpret the output of CLEAN algorithm carefully to avoid mistaking phantom paths as real paths. The tap-delay line channel model was found to be still applicable for UWB as discussed in Chapter 6.

Some researchers derived the discrete channel model by binning the continuous channel impulse response. It would be interesting to compare the binned continuous time channel model with the discrete time channel model derived from the CLEAN algorithm (or other super-resolution algorithms) in the future. How to extend the discrete tap-delay line channel model to include the distortions from various mechanisms will be another interesting and challenging research topic.

Appendix A: Signal distortions after passing through some common building materials

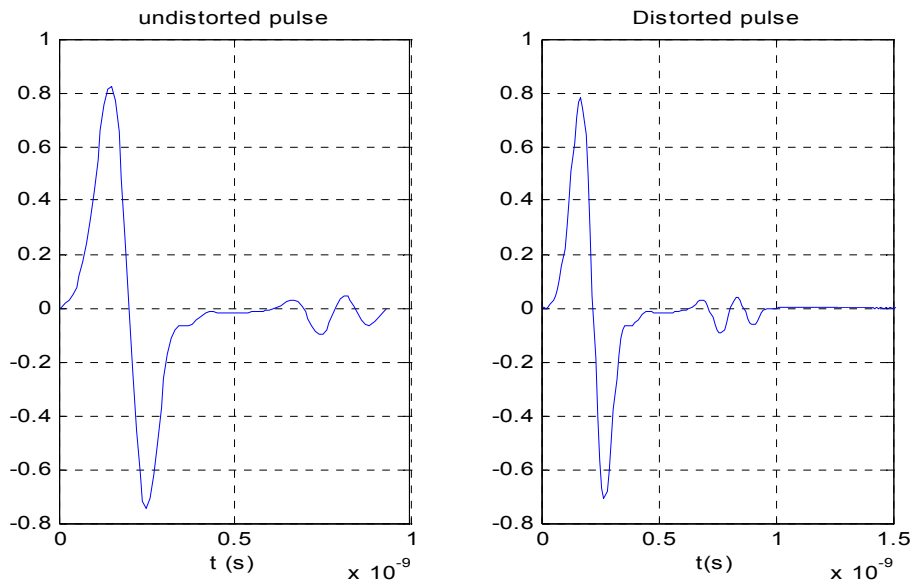


Figure A-1 Original and distorted UWB pulse after passing through wall board

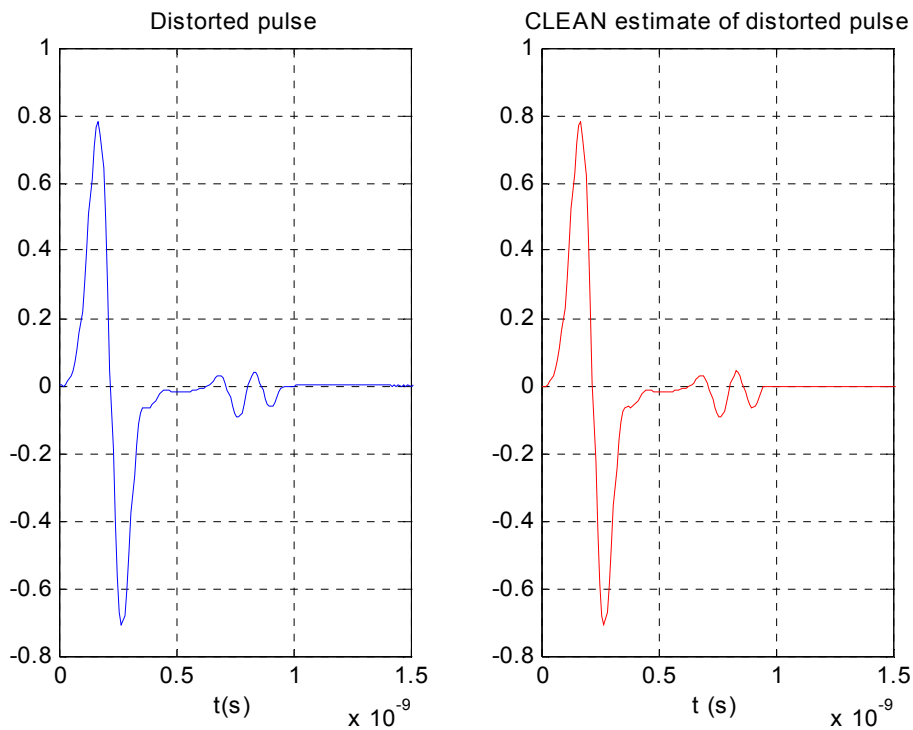


Figure A-2 Distorted UWB Pulse After Passing through wall board and Pulse Produced from CLEAN

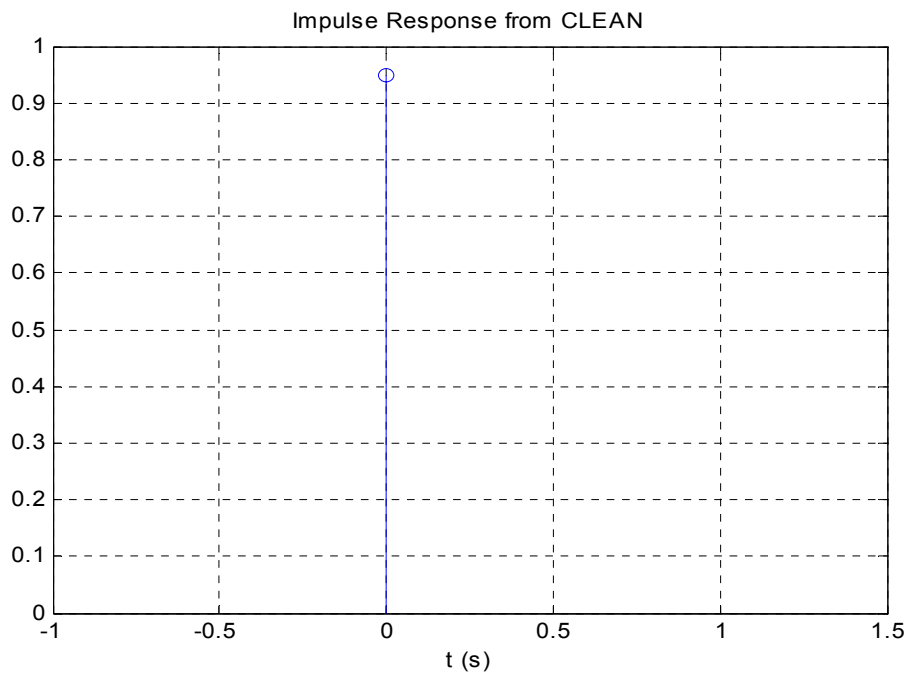


Figure A-3 Discrete Tap Channel Model Created by CLEAN Algorithm using the Distorted Pulse After Passing Through Wall Board (CLEAN threshold of 20 dB)

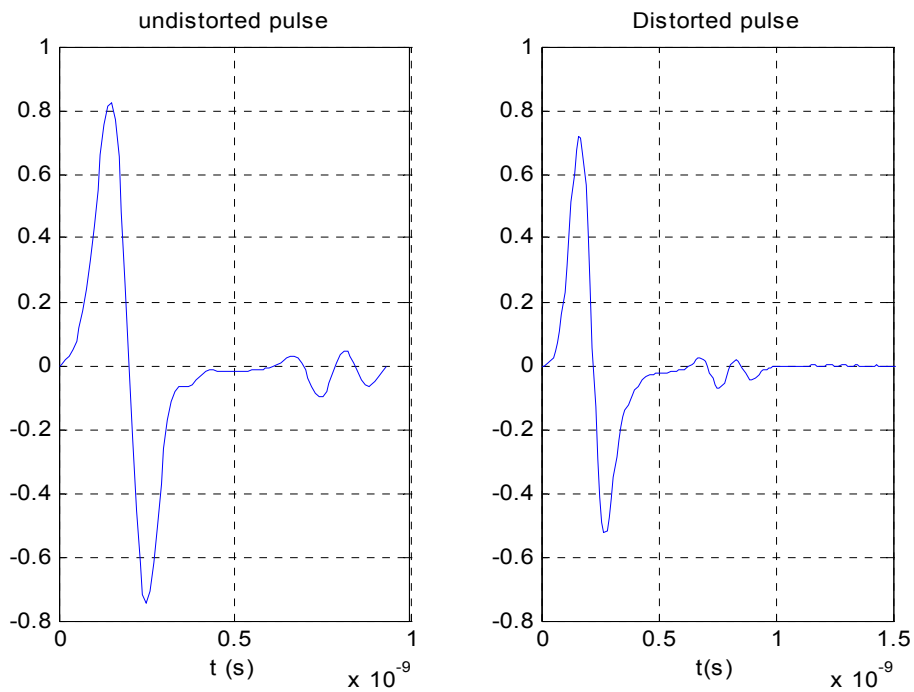


Figure A-4 Original and distorted UWB pulse after passing through cloth partition

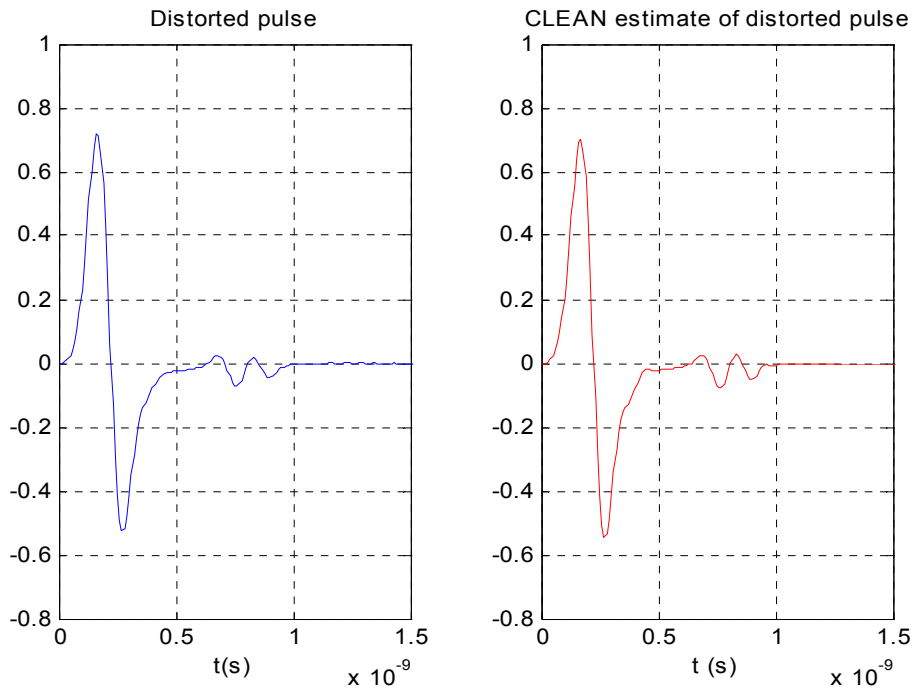


Figure A-5 Distorted UWB Pulse After Passing through cloth partition and Pulse Produced from CLEAN

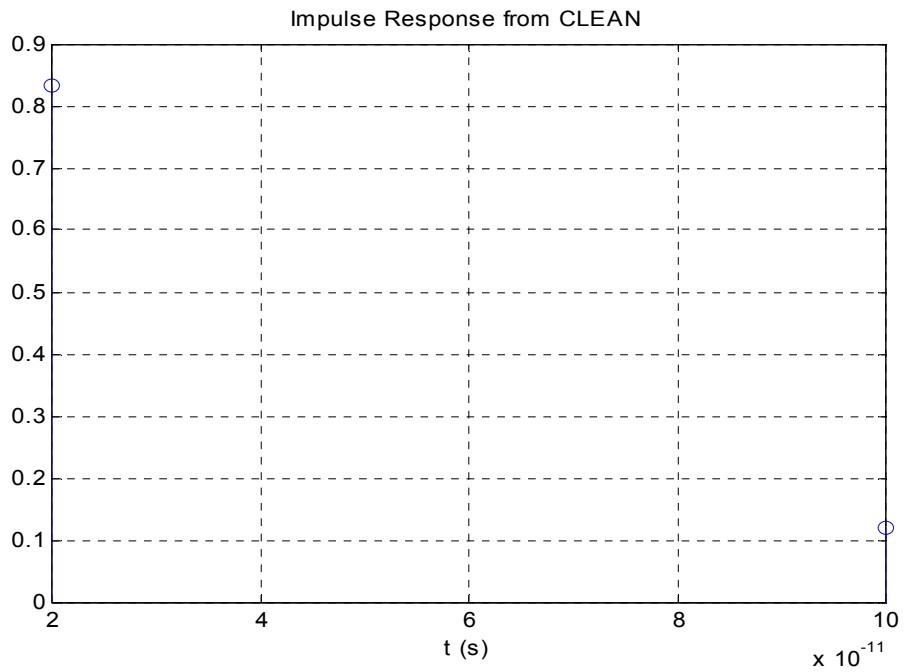


Figure A-6 Discrete Tap Channel Model Created by CLEAN Algorithm using the Distorted Pulse After Passing Through Cloth Partition (CLEAN threshold of 20 dB)

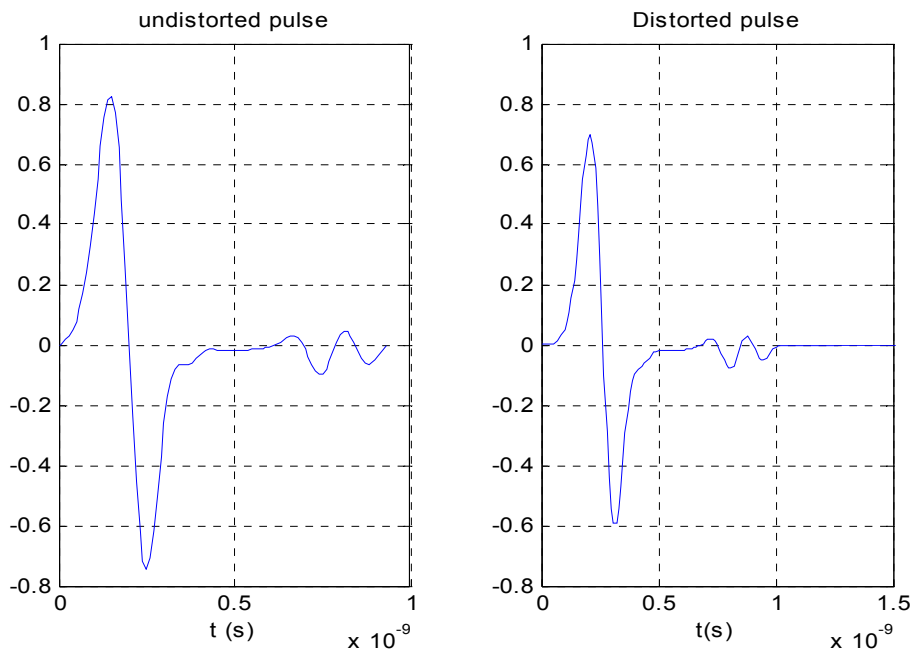


Figure A-7 Original and distorted UWB pulse after passing through door

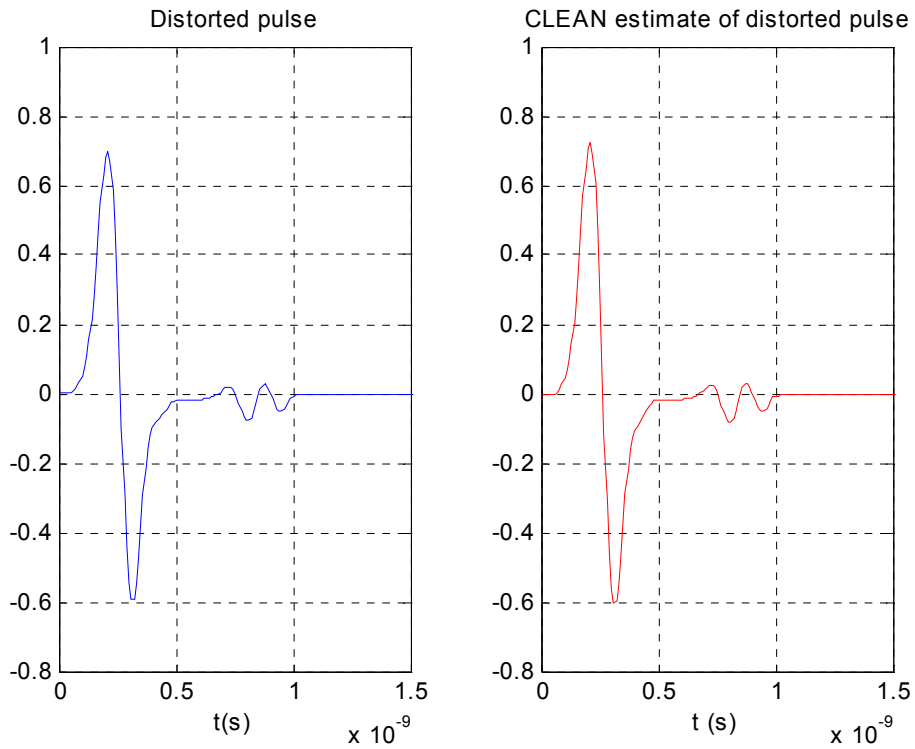


Figure A-8 Distorted UWB Pulse After Passing through door and Pulse Produced from CLEAN

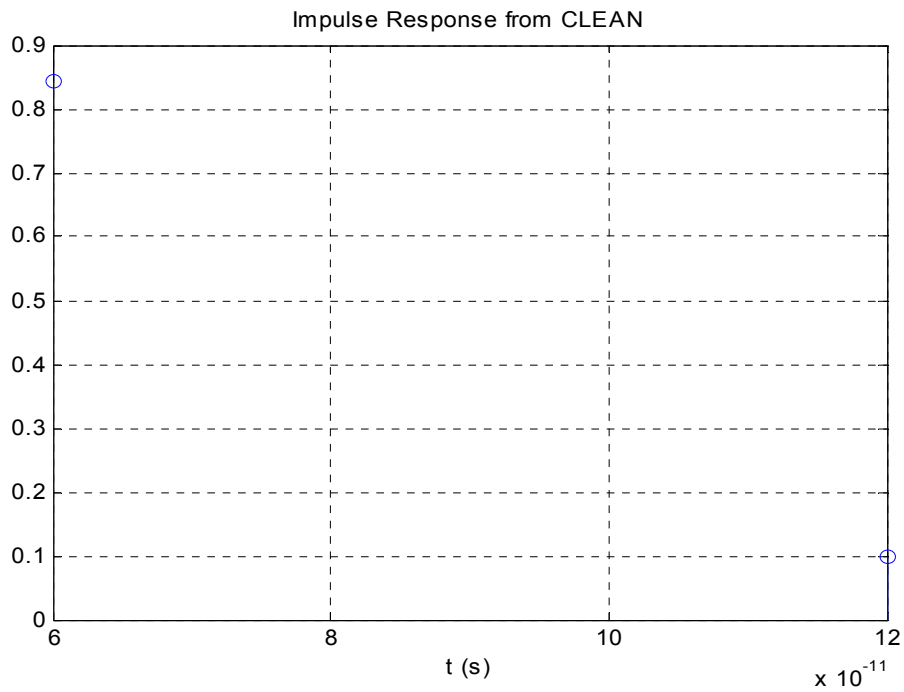


Figure A-9 Discrete Tap Channel Model Created by CLEAN Algorithm using the Distorted Pulse After Passing Through Door (CLEAN threshold of 20 dB)

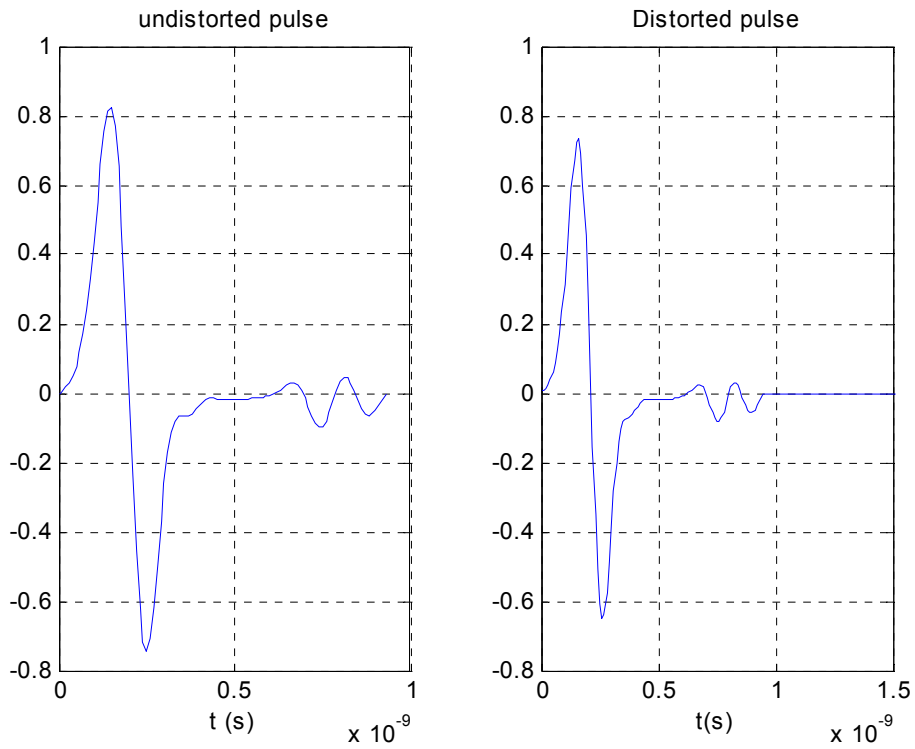


Figure A-10 Original and distorted UWB pulse after passing through glass

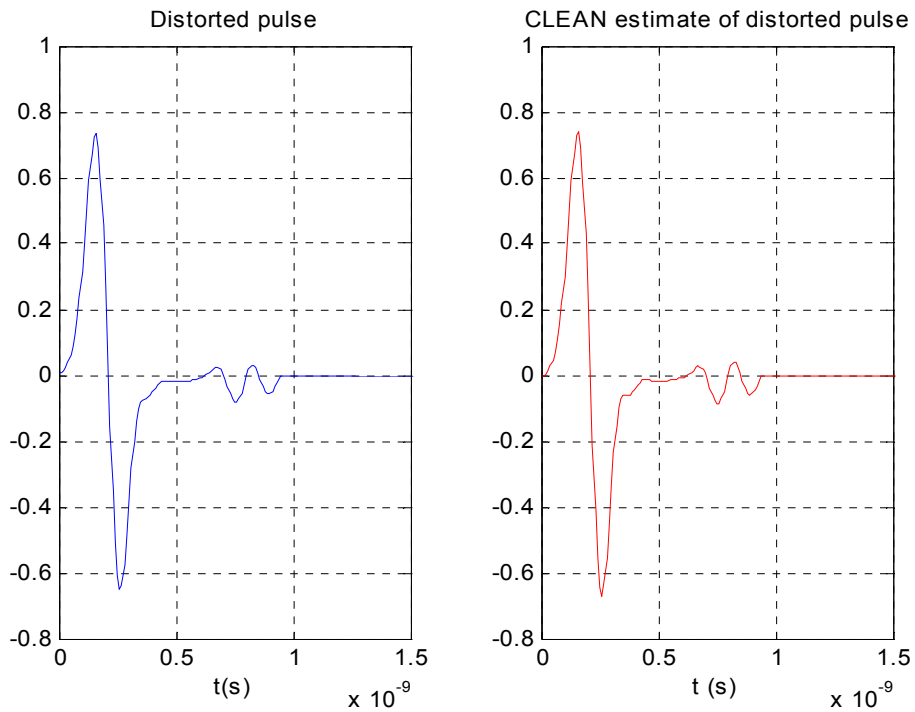


Figure A-11 Distorted UWB Pulse After Passing through glass and Pulse Produced from CLEAN

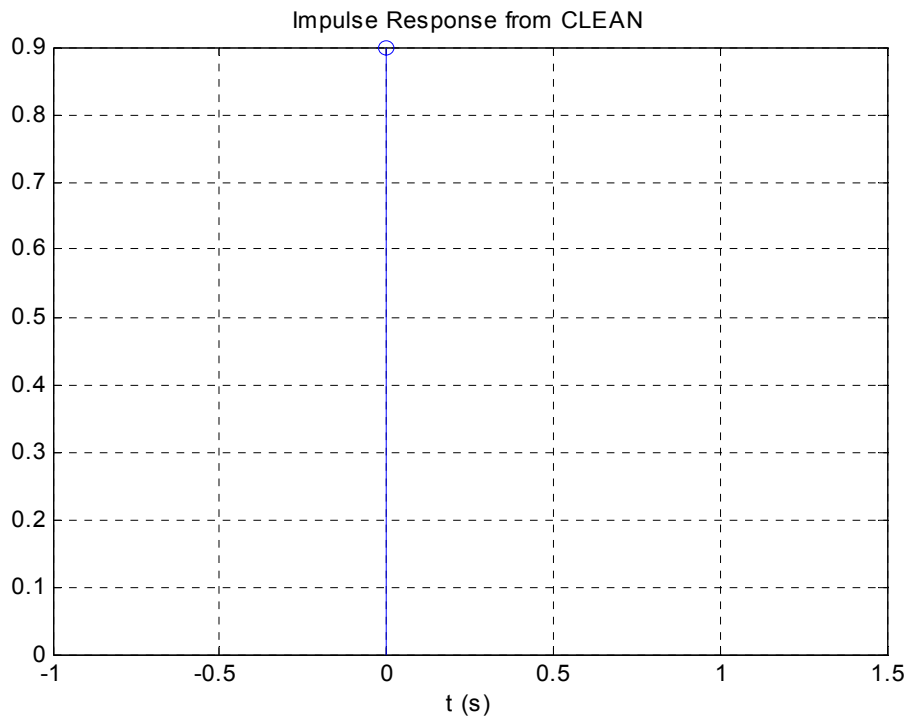


Figure A-12 Discrete Tap Channel Model Created by CLEAN Algorithm using the Distorted Pulse After Passing Through Glass (CLEAN threshold of 20 dB)

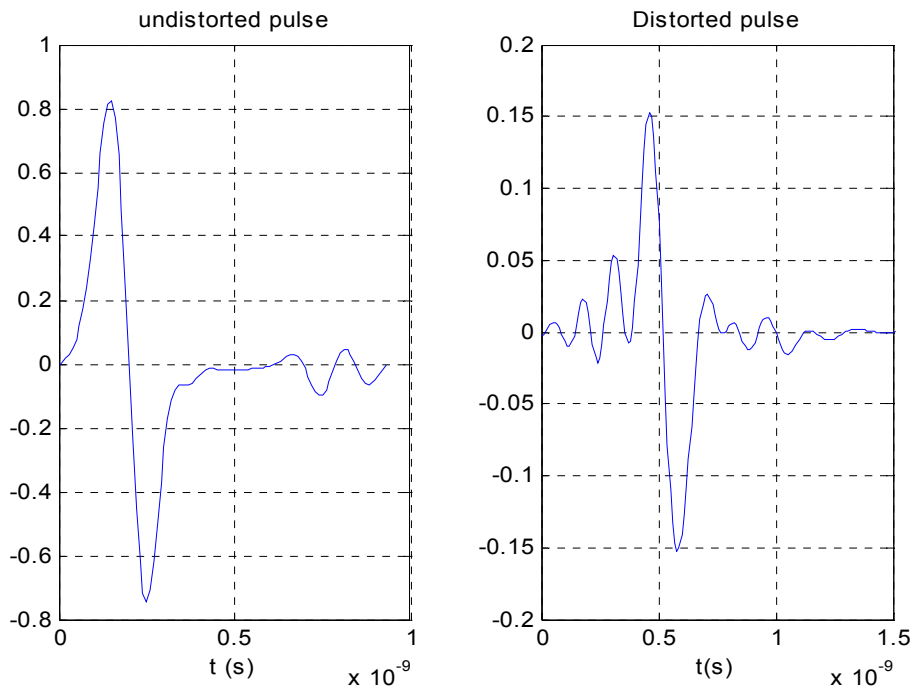


Figure A-13 Original and distorted UWB pulse after passing through concrete block

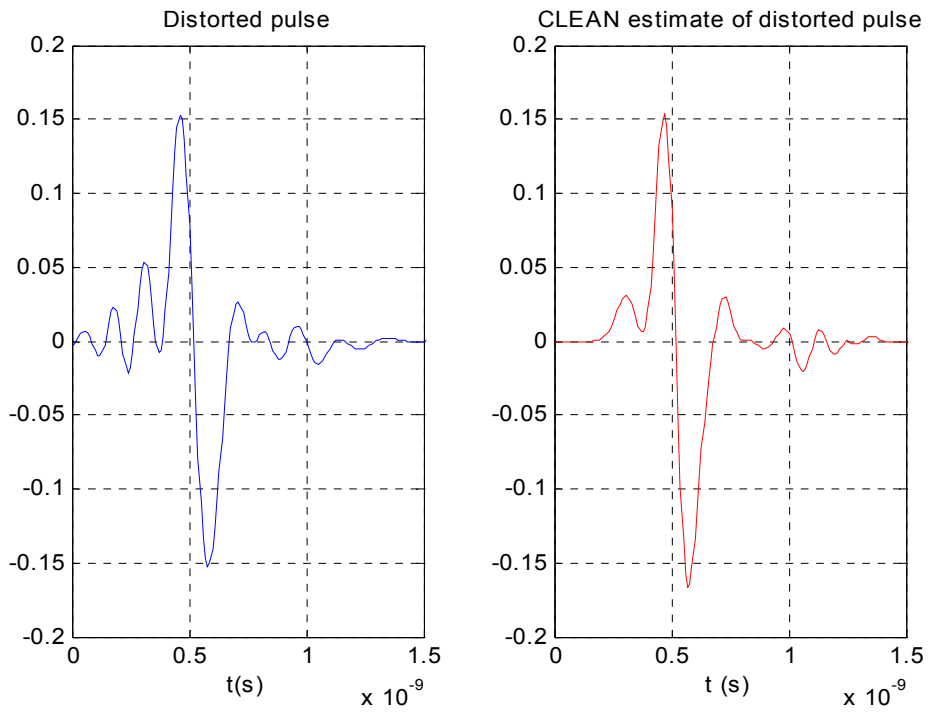


Figure A-14 Distorted UWB Pulse After Passing through concrete block and Pulse Produced from CLEAN

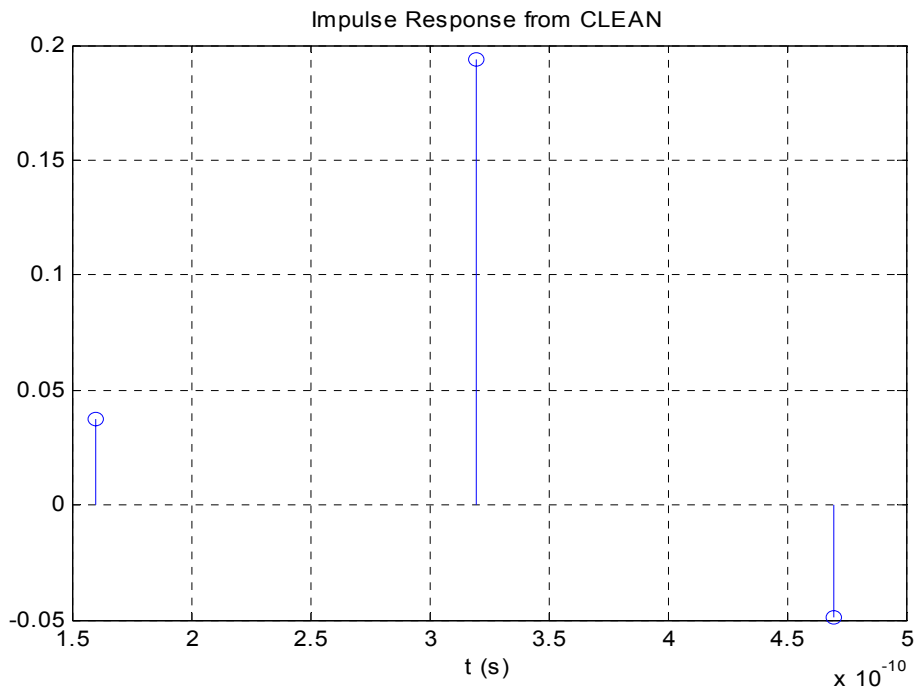


Figure A-15 Discrete Tap Channel Model Created by CLEAN Algorithm using the Distorted Pulse After Passing Through concrete block (CLEAN threshold of 20 dB)

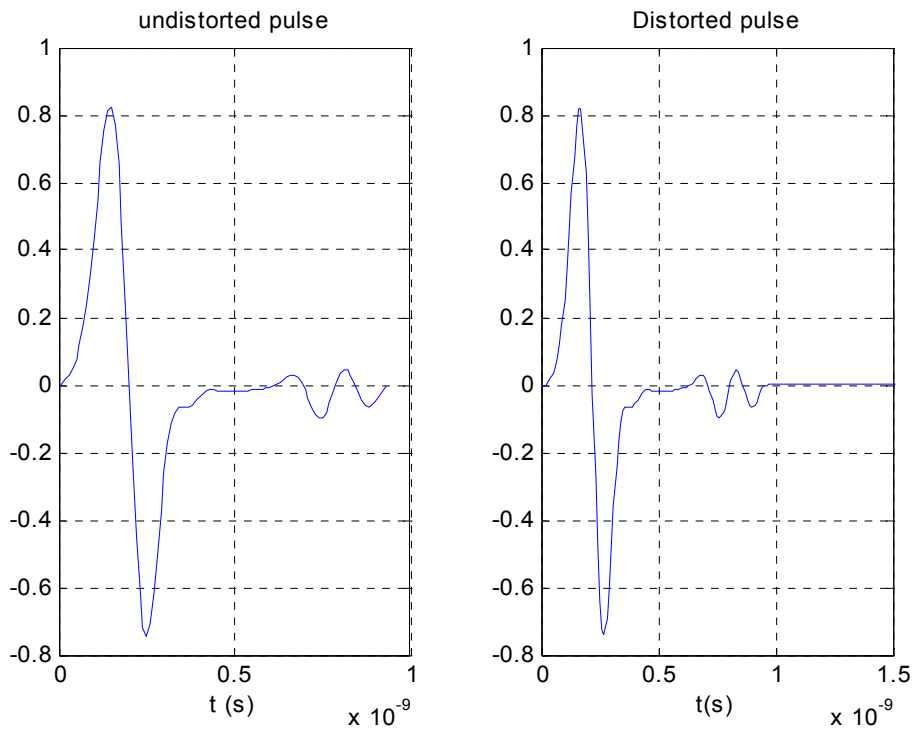


Figure A-16 Original and distorted UWB pulse after passing through foam

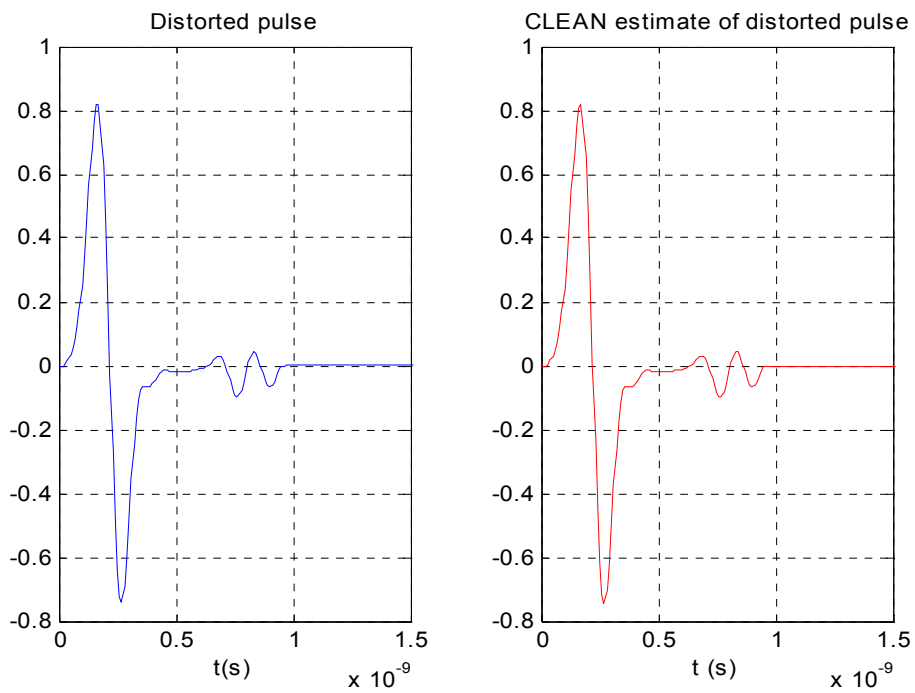


Figure A-17 Distorted UWB Pulse After Passing through foam and Pulse Produced from CLEAN

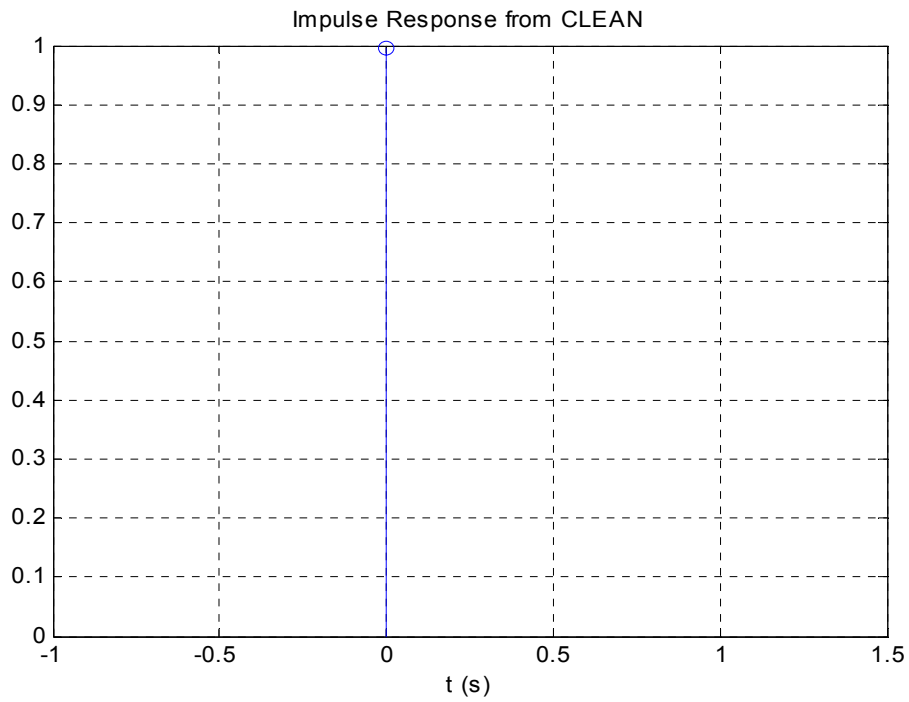


Figure A-18 Discrete Tap Channel Model Created by CLEAN Algorithm using the Distorted Pulse After Passing Through Foam (CLEAN threshold of 20 dB)

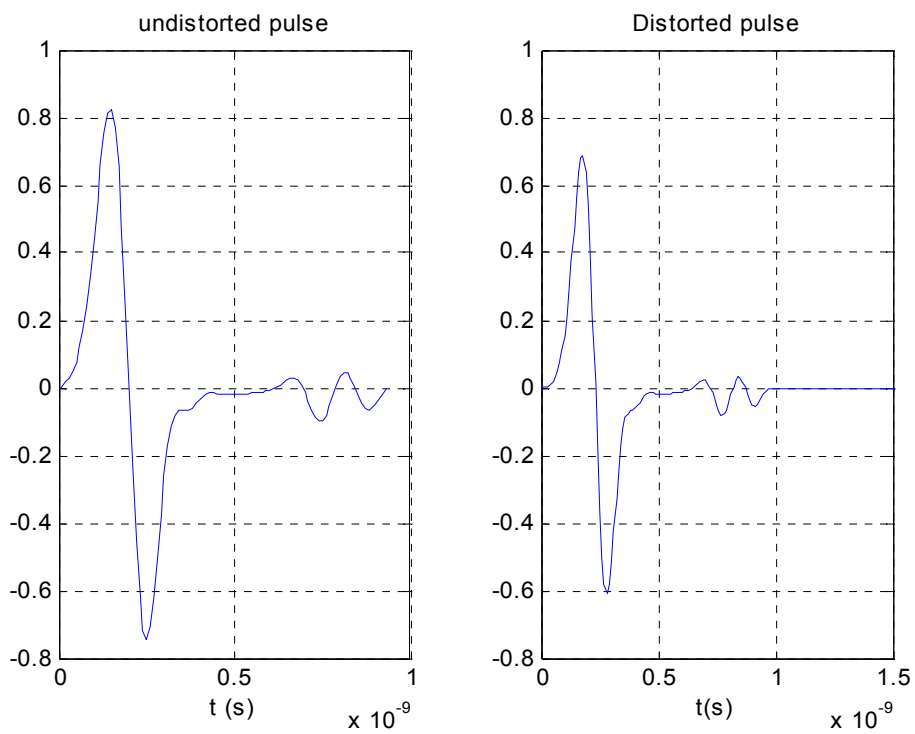


Figure A-19 Original and distorted UWB pulse after passing through plywood

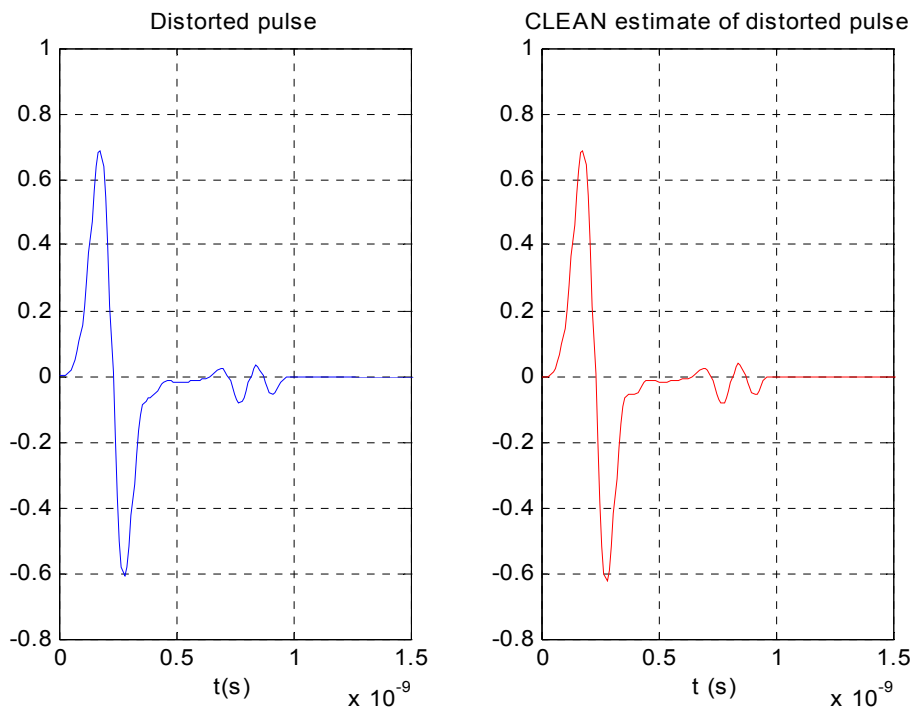


Figure A-20 Distorted UWB Pulse After Passing through plywood and Pulse Produced from CLEAN

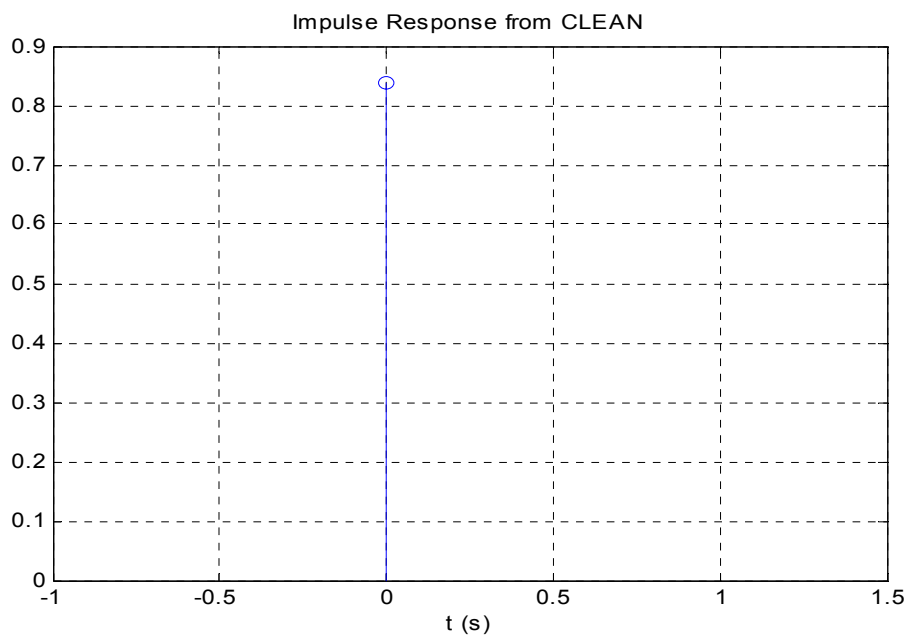


Figure A-21 Discrete Tap Channel Model Created by CLEAN Algorithm using the Distorted Pulse After Passing Through Plywood (CLEAN threshold of 20 dB)

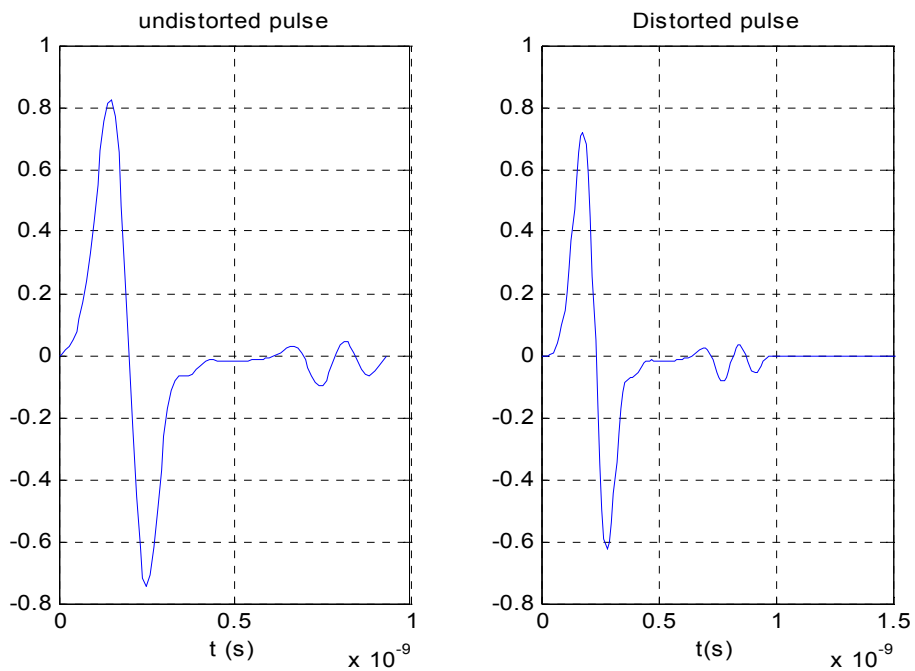


Figure A-22 Original and distorted UWB pulse after passing through structure wood

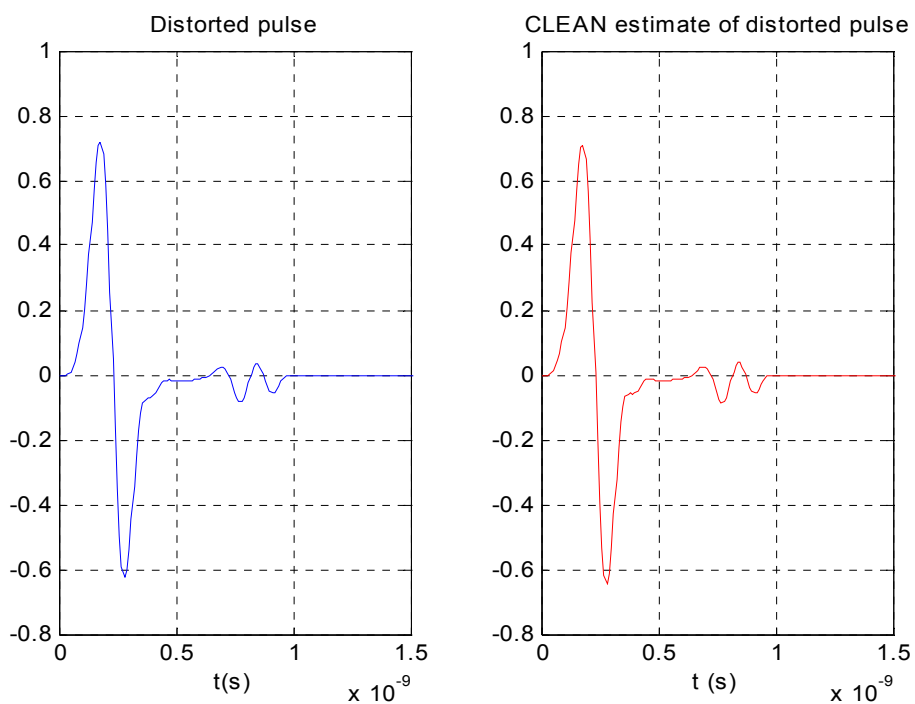


Figure A-23 Distorted UWB Pulse After Passing through structure wood and Pulse Produced from CLEAN

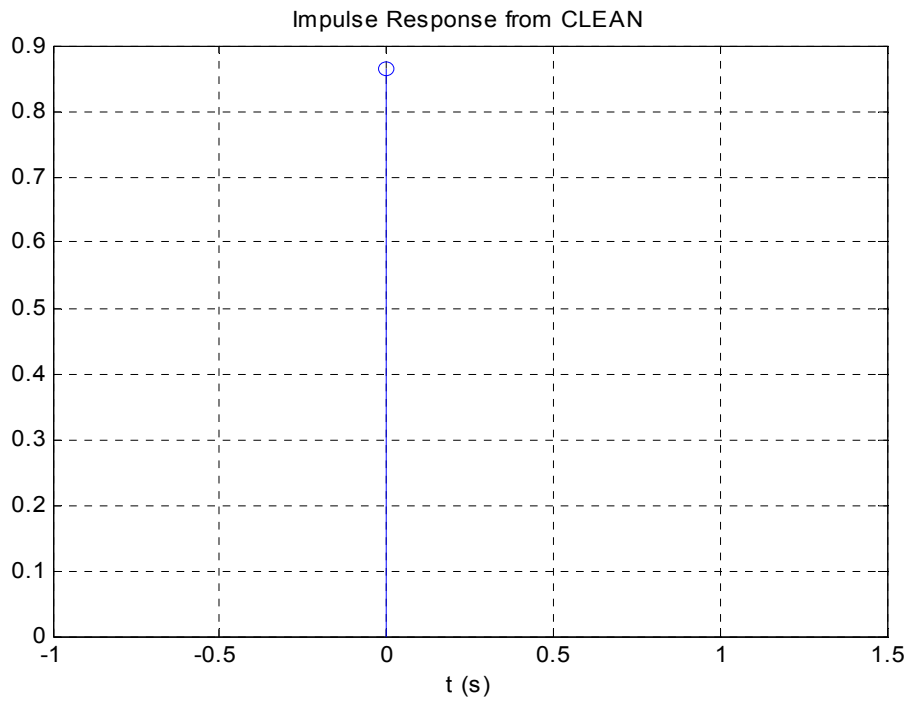


Figure A-24 Discrete Tap Channel Model Created by CLEAN Algorithm using the Distorted Pulse After Passing Through structure wood (CLEAN threshold of 20 dB)

Appendix B: Signal distortions due to reflections from some common shapes

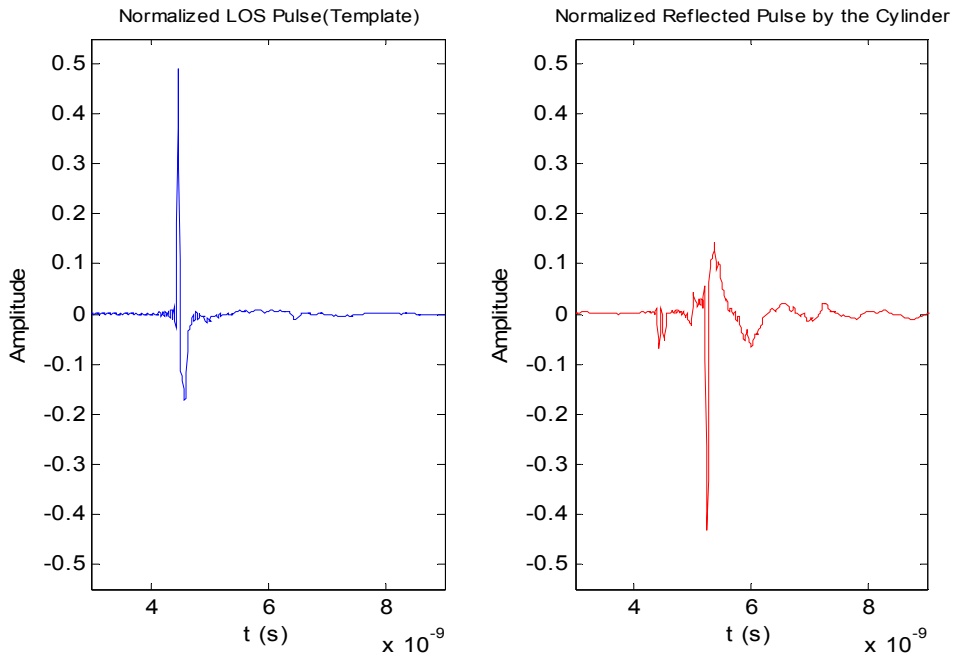


Figure B-1 Line-of-sight signal (left) and signal reflected from a cylinder

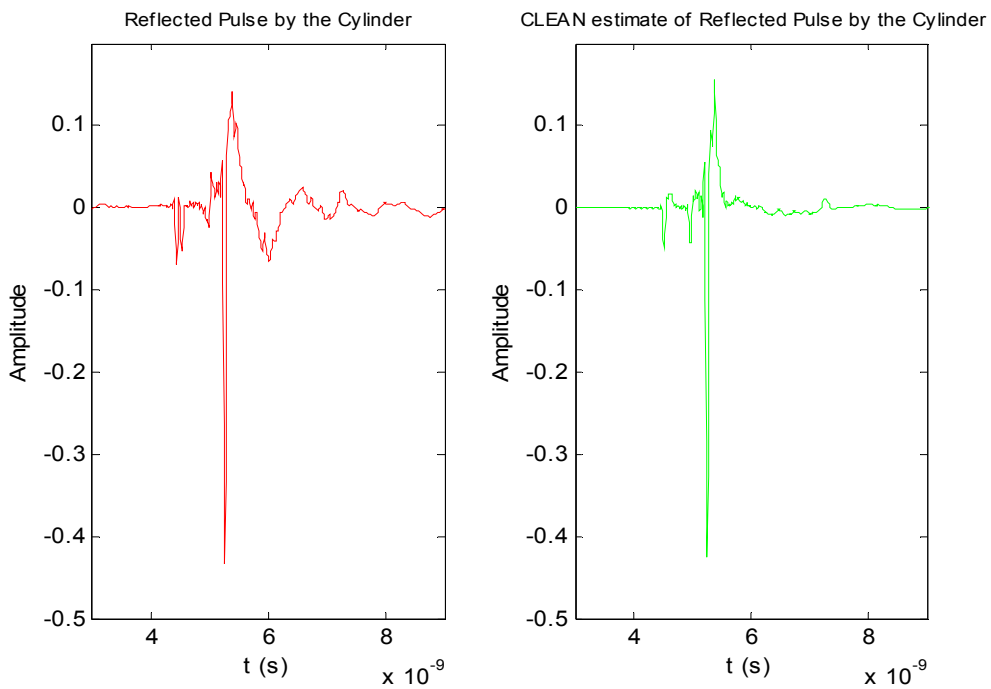


Figure B-2 Reflected pulse by a cylinder and CLEAN estimate of the reflected pulse

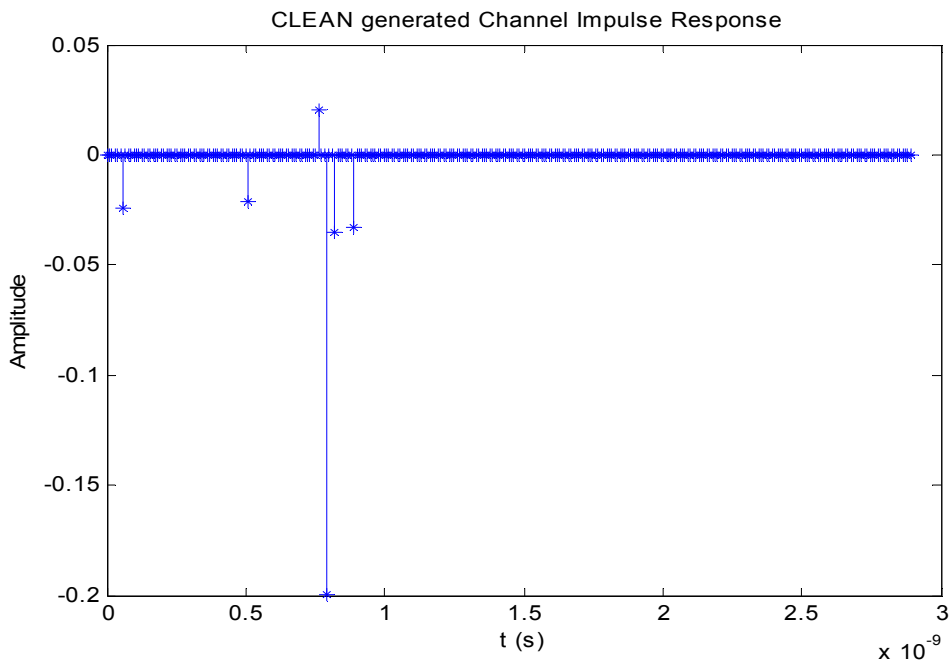


Figure B-3 CLEAN generated Impulse Response for signal reflected by a Cyliner with CLEAN threshold of 20 dB

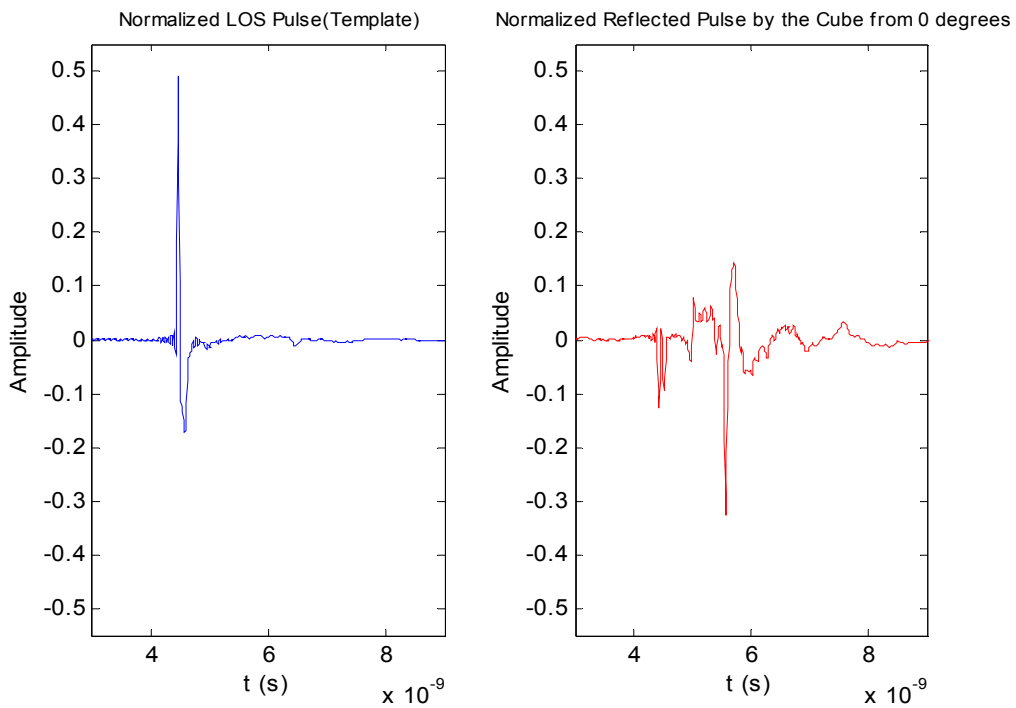


Figure B-4 Line-of-sight signal (left) and signal reflected by a cube from zero degrees

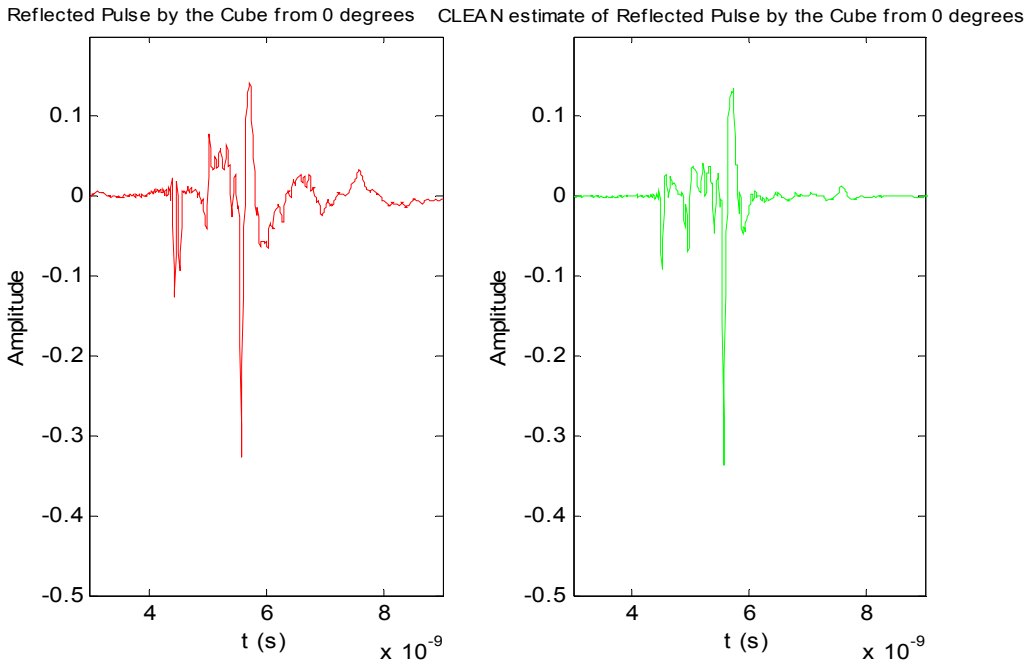


Figure B-5 Reflected pulse by a cube from zero degrees and CLEAN estimate of the reflected pulse

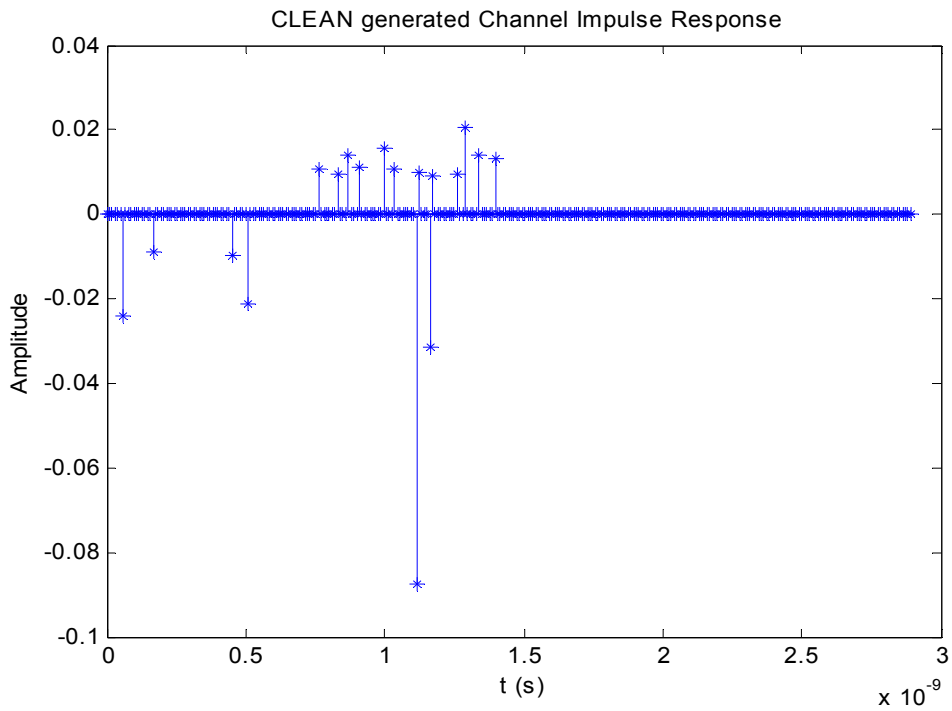


Figure B-6 CLEAN generated Impulse Response for signal reflected by a cube from zero degrees with CLEAN threshold of 20 dB

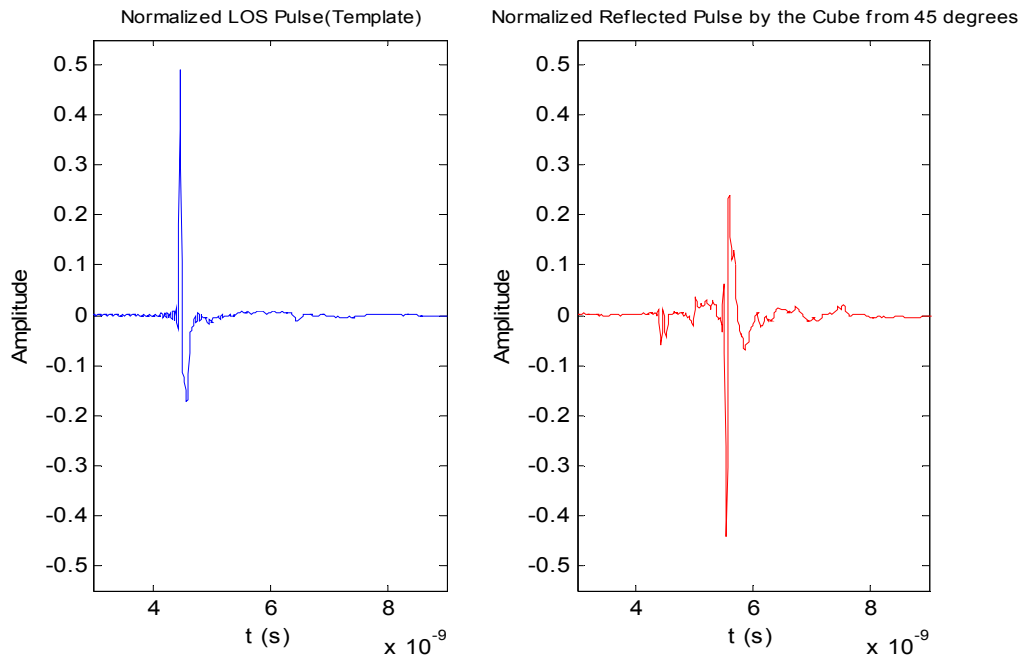


Figure B-7 Line-of-sight signal (left) and signal reflected by a cube from forty-five degrees

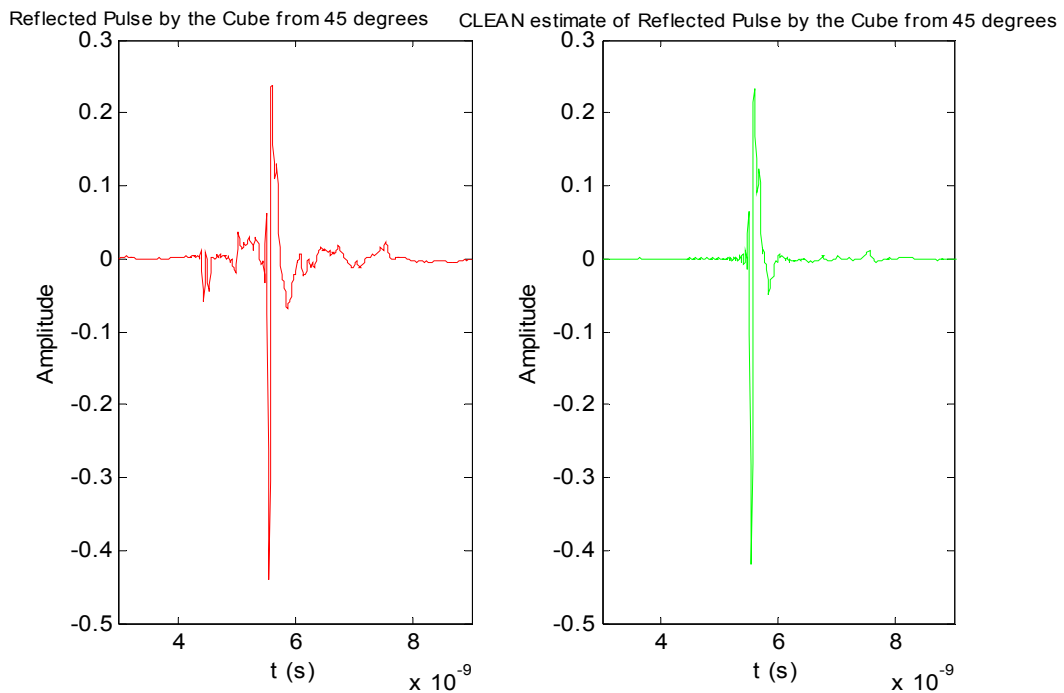


Figure B-8 Reflected pulse by a cube from forty-five degrees and CLEAN estimate of the reflected pulse

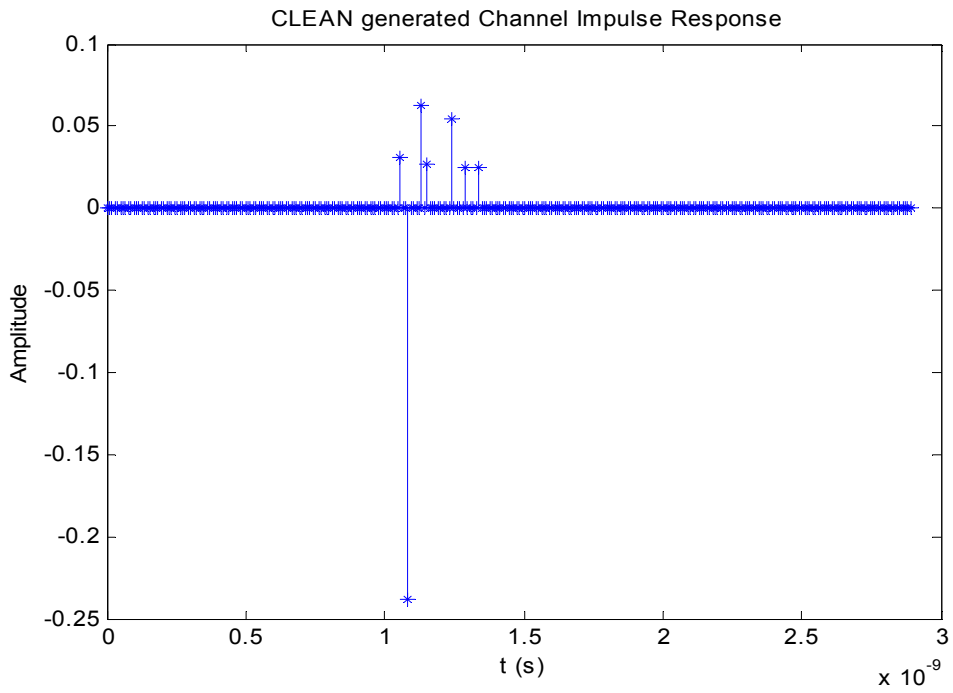


Figure B-9 CLEAN generated Impulse Response for signal reflected by a cube from forty-five degrees with CLEAN threshold of 20 dB

Bibliography

- [1] S. M. Yano, "Investigating the Ultra-Wideband Indoor Wireless Channel," *IEEE VTS 55th Vehicular Technology Conference*, vol. 3, pp. 1200-1204, May 2002.
- [2] FCC, "Revision of Part 15 of the Commission's Rules Regarding Ultra-Wideband Transmission Systems," *First Report and Order, ET Docket 98-153*, Feb. 2002.
- [3] Ross, G.F., "The transient analysis of multiple beam feed networks for array systems," *Ph.D. dissertation*, Polytechnic Institute of Brooklyn, Brooklyn, NY, 1963.
- [4] S. Verdu, "Wireless bandwidth in the making," *IEEE Communications Magazine*, vol. 38, no. 7, pp. 53–58, July 2000.
- [5] M. Z. Win, Xiaoxin Qiu, and R.A. Scholtz, V.O.K. Li, "ATM-based TH-SSMA network for multimedia PCS," *IEEE Journal on Selected Areas in Communications*, vol. 17, no. 5, pp. 824–836, May 1999.
- [6] Amara D. Angelica, "Powered by Pulse, More than an Pipe Dream," *TechWeek*, May.1999. Available:
<http://www.timedomain.com/Files/PDF/news/TechWeek.pdf>
- [7] T. S. Rappaport, *Wireless Communications: Principles and Practice*, Upper Saddle River, NJ: Prentice Hall, 1996.
- [8] K. Pahlavan and A. H. Levesque, *Wireless Information Networks*, John Wiley & Sons, Inc., 1995.
- [9] G. L. Turin, "Communication through Noisy, Random Multipath Channels," *IRE Conversion Record, part 4*, pp. 154-166, 1956.
- [10] H. Hashemi, "Impulse Response Modeling of the Indoor Radio Propagation Channels," *IEEE JSAC*, vol. 11, no.7, pp. 967-978, Sept, 1993
- [11] M. Win and R. A. Scholtz, "On the Energy Capture of Ultrawide Bandwidth Signals in Dense Multipath Environments," *IEEE Communications Letters*, vol.2, no.9, pp. 245-247, Sept 1998.
- [12] R. J-M. Cramer, *An Evaluation of Ultrawideband Propagation Channels*, PhD Dissertation, University of Southern California, Dec 2000.
- [13] R. M. Buehrer, W.A. Davis, A. Safaai-Jazi, and D. Sweeney, "Ultra-wideband Propagation Measurements and Modeling," *DARPA NETEX Program Final Report*, Jan. 31, 2004.

- [14] S. S. Ghassemzadeh, L. J. Greenstein, and V. Tarokh, "The Ultra-wideband Indoor Multipath Loss Model (doc: IEEE P802.15-02/282-SG3a and IEEE P802.15-02/283-SG3a)," submitted to IEEE P802.15 Working Group for Wireless Personal Area Networks (WPANs), Jun 2002. Available: <http://grouper.ieee.org/groups/802/15/pub/2002/Jul02/>
- [15] R. M. Buehrer, A. Safaai-Jazi, W. A. Davis, and D. Sweeney, "Characterization of the Ultra-wideband Channel," *IEEE Conference on Ultra Wideband Systems and Technologies*, pp. 26-31, Nov. 2003.
- [16] J. Foerester, "Channel Modeling Sub-committee Report Final (doc.: IEEE 802-15-02/490r1-SG3a)," submitted to IEEE P802.15 Working Group for Wireless Personal Area Networks (WPANs), Feb. 2002. Available: <http://grouper.ieee.org/groups/802/15/pub/2002/Nov02/>
- [17] C. Prettie, D. Cheung, L. Rusch, and M. Ho, "Spatial Correlation of UWB Signals in a Home Enviroment," *IEEE Conference on Ultra Wideband Systems and Technologies*, pp. 65-69, May 2002.
- [18] S. S. Ghassemzadeh, V. Tarokh, "UWB Path Loss Characterization in Residential Enviroments," *IEEE Radio Frequency Integrated Circuits Symposium*, pp. 501-504, June 2003.
- [19] S. S. Ghassemzadeh, R. Jana, C.W. Rice, W. Turin, and V. Tarokh, "A Statistical Path Loss Model for In-Home UWB Channels," *IEEE Conference on Ultra Wideband Systems and Technologies*, pp. 59-64, May 2002.
- [20] S. Haykin, *Adaptive Filter Theory*, Prentice-Hall, Englewood Cliffs, N.J.,1991
- [21] E. A. Robinson and S. Treitel, *Geophysical Signal Analysis*, Prentice-Hall, Englewood Cliffs, N.J.,1980
- [22] A. K. Jain, *Fundamentals of Digital Image Processing*, Prentice-Hall, Englewood Cliffs, N.J., 1989
- [23] S. M. Riad, "The Deconvolution Problem, an Overview," *Proceedings of the IEEE*, vol. 74, no. 1, pp. 82-85, Jan. 1986.
- [24] A. N. Tikhonov and V. Y. Arenin, *Solution of Ill-Posed Problems*, New York: Halsted, 1977
- [25] R. G. Vaughan and N. L. Scott, "Super-Resolution of Pulsed Multipath Channels for Delay Spread Characterization," *IEEE Transactions on Communications*, vol. 47, no. 3, pp. 343-347, Mar. 1999.

- [26] A. Bennis and S. M. Riad, "Filtering Capabilities and Convergence of the Van-Cittert Deconvolution Technique," *IEEE Transactions on Instrumentation and Measurement*, vol. 41, no. 2, pp. 246-250, April 1992.
- [27] J. A. Hogbom. "Aperture Synthesis with a Non-Regular Distribution of Interferometer Baselines," *Astron. and Astrophys. Suppl. Ser.*, vol. 15, pp. 417-426, 1974.
- [28] R. A. Scholtz, M. Z. Win, and J. M. Cramer, "Evaluation of the Characteristics of the Ultra-Wideband Propagation Channel," *Antennas and Propagation Society International Symposium*, vol.2. pp. 626-630, 1998.
- [29] P. Withington, R. Reinhardt, and R. Stanley, "Preliminary Results of an Ultra-wideband (Impulse) Scanning Receiver," *IEEE Military Communications Conference*, vol. 2, pp. 1186-1190, 1999.
- [30] R. J. Fontana, "Ultra Wideband Technology – The Wave of the Future?" Multispectral Solutions, Inc. Available: http://www.multispectral.com/pdf/ITCUSA_2000.pdf
- [31] H. Hashemi, "The Indoor Radio Propagation Channel," *Proceedings of the IEEE*, vol. 81, no. 7, pp. 943-968, July 1993.
- [32] J. M. Cramer, R. A. Scholtz, and M. Z. Win, "On the analysis of UWB communication channels," *Military Communications Conference Proceedings, IEEE*, vol. 2, pp. 1191-1195, Nov. 1999.
- [33] G. E. Athanasiadou, A. R. Nix, and J. P. McGeehan, "A ray tracing algorithm for microcellular and indoor propagation modeling," *IEE ICAP Conference on Antennas and Propagation*, vol. 2, pp. 231-235, April 1995.
- [34] L. Heikki, "Verification of a stochastic radio channel model using wideband measurement data," *Master Thesis*, Available: <http://www.vtt.fi/tte/tte35/pdfs/Mthesis.pdf>
- [35] B. Donlan and R. M. Bueherer, "Large and Small Scale Channel Modeling for Indoor UWB channels," *Submitted to IEEE Transactions on Wireless Communications*.
- [36] J. E. Ehrenberg, T. E. Ewart, and R. D. Morris, "Signal-processing Techniques for Resolving Individual Pulses in a Multipath Signal," *J. Acoustic Soc. Am.*, 63, pp. 1861-1865, 1978.
- [37] T. G. Manickam, R. J. Vaccaro, and D. W. Tufts, "A Least-Squares Algorithm for Multipath Time-Delay Estimation," *IEEE Transactions on Signal Processing*, vol. 42, no. 11, pp. 3229-3233, Nov, 1994.

- [38] T. G. Manickam and R. J. Vaccaro, "A Non-Iterative Deconvolution Method for Estimating Multipath Channel Responses," *Proc. of the IEEE Internat. Conf. On Acoustics Speech and Signal Processing*, vol.1, pp. 333-336, April 1993.
- [39] Z. Kostic, M. I. Sezan, and E. L. Titlebaum, "Estimation of the Parameters of a Multipath Channel Using Set-Theoretic Deconvolution," *IEEE Transactions On Communications*, vol. 40, no. 6, pp. 1006-1011, June 1992.
- [40] Z. Kostic and G. Pavlovic, "Resolving Subchip-Spaced Multipath Components in CDMA Communication Systems," *IEEE Transactions on Vehicular Technology*, vol. 48, no. 6, pp. 1803-1808, Nov 1999.
- [41] R. C. Qiu and I-T Lu, "A Novel High-Resolution Algorithm for Ray Path Resolving and Wireless Channel Modelling," *Sarnoff Symposium, IEEE Princeton Section*, pp. 0_59-0_63, April 28,1995.
- [42] R. C. Qiu and I-T Lu, "Wideband Wireless Multipath Channel Modeling with Path Frequency Dependence," *IEEE International Conference on Communications*, vol. 1, pp. 277-281, June 1996.
- [43] R. J-M. Cramer, M. Z. Win, and R. A. Scholtz, "Impulse Radio Multipath Characteristics and Diversity Reception," *IEEE International Conference on Communications*, vol. 3, pp. 1650-1654, June 1998.
- [44] A. A. Saleh and R. A. Valenzuela, " A Statistical Model for Indoor Multipath Propagation," *IEEE Journal on Selected Areas in Communications*, Vol. SAC-5, no. 2, pp. 128-137, Feb. 1987.

Vita

Liu Yang was born on March 17, 1979 in Chengdu, China. She received her Bachelor's degree in Electrical Engineering from the University of Electronic Science and Technology of China (UESTC) in 2001 with highest honors. In 2002, Liu began work towards a Master of Science degree in Electrical Engineering at Virginia Tech. Since summer of 2003 Liu has been working as a research associate in the Mobile and Portable Radio Research Group (MPRG) where she concentrated her research on the area of Ultra-Wideband Communications.